TÉCNICO LISBOA

A First Sample of Dust Attenuation Laws for DES Galaxies

João Ricardo Dias Duarte

Thesis to obtain the Master of Science Degree in

Engineering Physics

Supervisors: Prof. Ana Maria Vergueiro Monteiro Cidade Mourão
Prof. Santiago González Gaitán

Examination Committee

Chairperson: Prof. José Pizarro de Sande e Lemos
Supervisor: Prof. Santiago González Gaitán
Member of the Committee: Dr. Javier Peña Rubio

October 2021

Acknowledgments

This work could not (and would not) have been completed without the tireless help and support from many people. I cannot reasonably hope to fit all their names and contributions on this page, so allow me to offer some highlights.

I would like to begin by thanking my supervisors, Ana Mourão and Santiago González-Gaitán, for their invaluable assistance during every stage of this project. The importance of their openness and availability cannot be overstated. Most of all, I would like to thank them for the opportunity to participate in the CRISP Project (PTDC/FIS-AST-31546/2017) and FCT for all the financial support. I would also like thank all the group members who participated in our weekly meetings for their valuable comments and suggestions.

I would like to give a special thanks to my colleagues and friends, with whom I have shared both heartaches and successes over the course of the last five years (longer in some cases). Because of all of you, it is truly bittersweet to see this journey come to an end.

Finally, I would like to offer my deepest gratitude to my family for all the loving and caring support, not only during the completion of this thesis, but indeed throughout all my life.

Resumo

Supernovas tipo Ia (SNe Ia) são indicadores de distancia úteis em cosmologia, desde que a sua luminosidade seja calibrada aplicando algumas correções. Um dos fatores motivantes destas correções é a extinção por poeira, contabilizada na relação cor-luminosidade β da calibração.

Propomos uma abordagem alternativa para inferir leis de atenuação por poeira para galáxias hospedeiras de 162 SNe Ia, partindo de fotometria global e local (4kpc). Modelos de População Estelar Simples são ajustados à fotometria ótica obtida do Dark Energy Survey, complementada quando possível por fotometria GALEX UV e 2MASS NIR. Mostramos que 4 filtros são suficientes para recuperar propriedades de poeira para galáxias consistentemente com previsões da literatura baseadas em simulações e observações.

Mostramos que propriedades de poeira variam bastante entre galáxias. Isto significa que não podemos assumir uma calibração universal para SNe Ia. Obtemos uma relação entre a inclinação de atenuação e a profundidade ótica, global e localmente, melhor explicada pela variação da geometria estrelas/poeira com a orientação da galáxia. Esta relação revela-se muito diferente da extinção encontrada diretamente para SNe.

Analisando os resíduos de Hubble para as SNe, encontramos degraus relacionados com a profundidade ótica e a inclinação da atenuação, interpretados como reflecções menos significativas do ”degrau em massa”. Uma descrição deste fenómeno totalmente motivada por poeira mostra-se possível utilizando um ”degrau em poeira” bidimensional.

Estudamos uma nova calibração para SNe Ia, separando as contribuições intrínseca e de extinção na relação cor-luminosidade, sendo a última aproximada pela atenuação da hospedeira. Concluímos que é pior que a calibração usual.

Palavras-Chave: calibração de supernovas; extinção por poeira; atenuação por poeira; escala de distância

Abstract

Type Ia supernovae (SNe Ia) are useful distance indicators in cosmology, provided their luminosity has been calibrated by applying some corrections. One of the factors motivating these corrections is dust extinction, accounted for in the β color-luminosity relation of the calibration.

We propose an alternative approach to infer dust attenuation laws towards the host galaxies of 162 SNe Ia, from both global and local (4 kpc) photometry. Simple Stellar Population models are fitted to optical photometry obtained from the Dark Energy Survey, complemented when possible with GALEX UV and 2MASS NIR photometry. We show 4 filters bands are sufficient to recover dust properties for hosts consistently with literature predictions based on both simulations and observations.

We show dust properties vary greatly across different galaxies, meaning an universal SN Ia correction cannot be assumed. We find a relation between the attenuation slope and the optical depth, both locally and globally, best explained by varying star/dust geometry with galaxy orientation. This relation is shown to be very different from the extinction found directly for SNe.

Analyzing the Hubble residuals for the SNe, we find optical depth and attenuation slope related steps, interpreted as less significant reflections of the ”mass-step”. An entirely dust motivated description of this phenomenon is found to be possible when employing a two dimensional ”dust-step”.

We study a new SNe Ia calibration, separating the intrinsic and extinction contributions in the color-luminosity correction, the latter being approximated by host attenuation. We conclude it is worse than the standard calibration.

Keywords: supernovae calibration; dust extinction; dust attenuation; distance scale

Contents

List of Tables

List of Figures

List of Abbreviations

BBC BEAMS with Bias Corrections.

CDM Cold Dark Matter.

DECam Dark Energy Camera.

DES Dark Energy Survey.

FUV Far Ultraviolet.

FWHM Full Width Half-Maximum.

IMF Initial Mass Function.

ISM Interstellar Medium.

M-H MCMC Metropolis-Hastings Markov Chain Monte Carlo.

NIR Near Infrared.

NUV Near Ultraviolet.

PSF Point Spread Function.

RMS Root Mean Square.

SED Spectral Energy Density.

SFH Star Formation History.

SFR Star Formation Rate.

SN Supernova.

SN Ia Type Ia Supernova.

SNR Signal-to-Noise Ratio.

SSP Simple Stellar Population.

UV Ultraviolet.

Chapter 1

Introduction

1.1 Type Ia Supernovae and Distance Calibration

Type Ia supernovae (SNe Ia) are generally agreed to be the result of the explosion of a white dwarf in an interacting binary system. This occurs, for example, when either accretion of material from its companion or a merger with a different star causes the white dwarf mass to approach the Chandrasehkar limit[1].

They differ from the arguably more famous core-collapse supernovae, such as Type Ib, Ic and II supernovae. These types of supernova, which represent the final stage for young and highly massive stars, are only found in regions of star formation with younger stellar populations, while SNe Ia can be found in all galaxy types, both younger star-forming galaxies and older quiescent galaxies. In fact, SNe Ia can explode as early as ~ 40 Myr and as late as a Hubble time (~ 14 Gyr) after starburst[2].

SNe Ia are a set of important cosmological objects, making for excellent distance indicators, among other things. In particular, they famously contributed to the discovery of the accelerated expansion of the Universe[3][4]. In this capacity they are often referred to as candles, even though they are not considered "standard" candles, as they do not have a known absolute peak magnitude. Their peak luminosity can, however, be standardized by applying some empirical corrections based on color-luminosity and light curve shape-luminosity relations[5]. Additionally, a third correction is often introduced, as there is evidence for a luminosity dependence related to the stellar mass of the SN Ia host galaxy $M_\star$ [6], with SNe Ia originating in higher-mass galaxies being more luminous, even after the application of the other corrections.

These corrections are used to estimate the absolute magnitude of a SN Ia, from which the luminosity distance d_L to the SN can be obtained by comparison with the observed apparent magnitude. This distance is often indirectly parameterized by means of the distance modulus μ, defined as the difference between the apparent and absolute magnitudes of a given celestial object:

$$\mu = 5\text{Log}\left(\frac{d_L}{10\text{pc}}\right) \tag{1.1}$$

The standardization of a group of SNe Ia begins with an initial fit of the light-curve for each SN, returning values for the light-curve width x_1, colour c, and observed magnitude m_B. The colour parameter,

in particular, is defined as approximately the difference between the magnitude m in the B and V bands at the fitted epoch of peak brightness[7]:

$$c \simeq m(\lambda_B) - m(\lambda_V) = B - V \quad \text{at peak brightness,} \tag{1.2}$$

where $\lambda_V = 5510$Å and $\lambda_B = 4450$Å.

A "BEAMS with Bias Corrections" (BBC) fitting method[7] can then be used to convert the light curve fit parameters into corrected distance modulus values μ and to determine nuisance parameters α, β, γ and M, which are considered to be the same for the entire population. These parameters describe the shape-luminosity, color-luminosity and mass step corrections, as well as the absolute magnitude of a fiducial SN Ia with $x_1 = 0$ and $c = 0$. Additionally, the BBC method can also be used to determine a bias term $\delta\mu_{bias}$, which accounts for inherent biases due to selection effects and the light-curve analysis[8]. Taking all these corrections into account, the distance modulus μ of each SN Ia is given by[5]:

$$\mu = m_B - M + \alpha x_1 - \beta c + \delta_M + \delta\mu_{bias} \tag{1.3}$$

In the previous expression, δ_M is the "mass step" term, which is dependent on the host galaxy mass and γ[9]:

$$\delta_M = \begin{cases} \frac{\gamma}{2}, & \text{if } \mathrm{Log}(M_\star/M_\odot) > 10 \\ -\frac{\gamma}{2}, & \text{if } \mathrm{Log}(M_\star/M_\odot) < 10 \end{cases}. \tag{1.4}$$

For each SN, the deviation between the value obtained for μ from Eq. 1.3 and the expected distance modulus μ_{model} value at the corresponding redshift in a given cosmological model is known as an Hubble residual $\Delta\mu$:

$$\Delta\mu = \mu - \mu_{\text{model}} \tag{1.5}$$

By examining these residuals carefully, one can quantify the accuracy of the SNe Ia calibration. The easiest way to do this is by looking at the root mean square (RMS) of the fit, defined by:

$$RMS = \sqrt{\frac{1}{N}\sum_{i=1}^{N} \Delta\mu_i^2}, \tag{1.6}$$

where N is the total number of SNe Ia in the sample.

As expressed in Eq. 1.1, the previously mentioned μ_{model} is simply a function of the luminosity distance d_L which, for a Friedmann-Robertson-Walker cosmology, only depends on the cosmological parameters and the redshift[3]. In this work, we assume a spatially-flat ΛCDM model, which postulates a Universe composed of three major components: dark energy, which is assumed to behave like a cosmological constant Λ; cold dark matter (CDM); and ordinary baryonic matter[10]. We assume a matter density $\Omega_m = 0.3$, a dark energy density of $\Omega_\Lambda = 0.7$ and an Hubble constant $H_0 = 70\,\mathrm{km\,s^{-1}\,Mpc^{-1}}$. Under these assumptions, the luminosity distance is given by[9]:

$$d_L(z) = (1+z)c \int_0^z \frac{dz'}{H_0\sqrt{\Omega_m(1+z')^3+\Omega_\Lambda}} \tag{1.7}$$

1.2 Astrophysical Dust

There are two main factors contributing to the color-luminosity correction parametrized by β in Eq. 1.3: the intrinsic color variations among different SNe Ia and the effects of astrophysical dust, in particular reddening.

Astrophysical dust is one of the main components of the interstellar medium (ISM) of galaxies and it can be divided into two main components: a diffuse dust component and a birthcloud dust component. The first type of dust is formed during the course of stellar evolution, with grains forming in the atmospheres of stars or in the remnants of supernovae, and being subsequently released or ejected into the ISM[11]. The second type of dust refers to remnants of the birthcloud responsible for a given stellar population. As this birthcloud eventually disperses, this type of dust is most relevant for younger stellar populations.

For a given observation, the effects of dust on the observed light during its travel can be described by one of two distinct concepts: extinction or attenuation, depending on whether we are dealing with a point or extended source, respectively[11]. The different effects relevant in each case are schematically represented in Fig. 1.1.

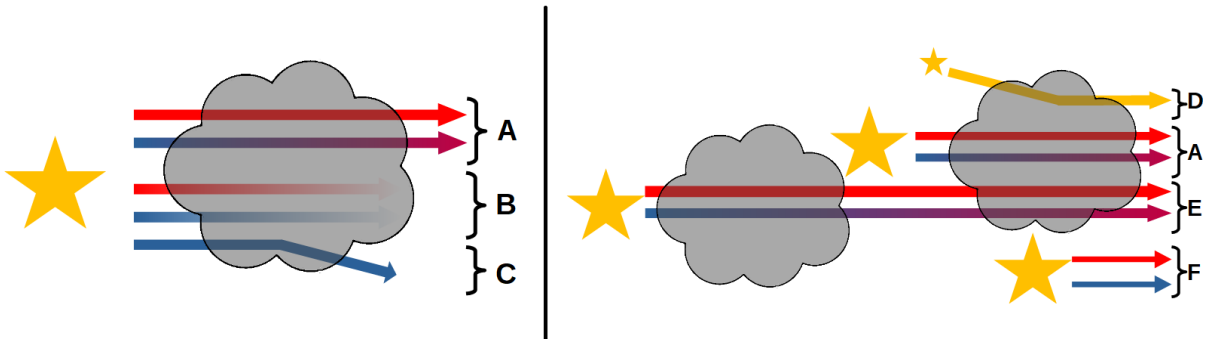

Figure 1.1: Schematic representation of dust extinction and dust attenuation[11]. For the dust extinction experienced by one individual light source (left panel), the following phenomena are pictured: A) Interstellar reddening, B) Absorption, C) Scattering of light out of that line of sight. Reddening results from a combination of the other two phenomena. For the dust attenuation in extended star/dust distributions (right panel), the following phenomena are pictured: A) Interstellar reddening, D) Scattering of light back into the line of sight, E) Varying dust column densities, F) Unobscured stars. Based on Salim (2020)[11]

.

The extinction for an individual point source at a given wavelength results from a combination of the overall composition, size and orientation of the dust grains. It refers to the absorption of light along a particular line of sight as well as scattering of that light out of the line of sight. Given that the wavelength of blue light is comparable to the typical size of dust grains (5 to 250 nm)[11], it tends to be absorbed and scattered more strongly than red light. This leads to a reddening of the observed spectrum. Extinction

is employed when referring to an object that can be considered a point source.

Attenuation includes not only the above mentioned effects of absorption and scattering described for extinction, but also effects arising from the spacial distribution of stars and dust in a galaxy or stellar population, such as scattering of light back into the line of sight, variable dust densities and light emitted by unobscured stars. Attenuation is most often discussed in the context of galaxies and other extended objects, as the previously described phenomena are negligible when considering only a single star. For the purposes of introducing the formalism used to describe both of these phenomena, we will use the terms extinction and attenuation interchangeably for the rest of this section.

Consider a source emitting with intensity $I_0(\lambda)$ for a given wavelength λ, whose light travels through a dust cloud. The intensity of the light as it leaves the cloud is given by:

$$I(\lambda) = I_0(\lambda)e^{-\tau(\lambda)}, \tag{1.8}$$

where $\tau(\lambda)$ is defined as the optical depth of the dust cloud [12].

It is more useful to look at this expression in terms of the magnitudes of the objects in question. Therefore, taking $m_0(\lambda)$ to be the unattenuated spectral energy density (SED) of some astronomical object for a given wavelength λ and $m(\lambda)$ the actual observed SED, the attenuation for that same λ is given by[11][12]:

$$A(\lambda) = m(\lambda) - m_0(\lambda) = -2.5\text{Log}\left(\frac{I(\lambda)}{I_0(\lambda)}\right) = -2.5\text{Log}(e^{-\tau_\lambda}) \simeq 1.086\tau(\lambda). \tag{1.9}$$

Three important quantities can be defined at this point: the optical depth for the V band τ_V, the color excess $E(B-V)$, and the ratio of total-to-selective attenuation R_V:

$$\tau_V = \tau(\lambda_V) \simeq \frac{A_V}{1.086} \tag{1.10}$$

$$E(B-V) = [m(\lambda_B) - m(\lambda_V)] - [m(\lambda_B)_0 - m(\lambda_V)_0] = A(\lambda_B) - A(\lambda_V) \tag{1.11}$$

$$R_V = \frac{A_V}{E(B-V)} \tag{1.12}$$

where once again we have $\lambda_V = 5510$Å and $\lambda_B = 4450$Å. It should be noted that, if the existence of the β color-luminosity relation in Eq. 1.3 was entirely due to dust, then we would have[13]:

$$\beta_{R_V} = R_V + 1 \tag{1.13}$$

Attenuation is usually described by means of an attenuation curve $k(\lambda)$, with $\frac{A_V}{R_V} = E(B-V)$ acting as a normalization factor. This choice of normalization is, however, mostly arbitrary[11]. $A(\lambda)$ can then be expressed as an attenuation law, in the form:

$$k(\lambda) = \frac{A(\lambda)}{A_V}R_V \qquad \Longrightarrow \qquad A(\lambda) = \frac{A_V}{R_V}k(\lambda) \iff \tau(\lambda) = \frac{\tau_V}{R_V}k(\lambda). \tag{1.14}$$

From this formalism, it is possible to define a set of typical curves that describe the overall behaviour

of attenuation properties across different wavelengths for a variety of conditions. Some examples of typical attenuation curves are displayed in Fig. 2.1. The comparison between different curves is made easy by the introduction of several parameters that help to describe each curve. In particular, and of major importance to the present work, the slope of the curve gives precious insight into the reddening effect. We will explore this notion further in later chapters.

1.3 Motivation and Objectives

As mentioned before, for the purposes of standardization, the value of β in Eq. (1.3) is assumed to be one and the same for the entire population of SNe Ia under study.

However, it has been shown that not only can dust properties vary from galaxy to galaxy, they can also vary significantly across different lines of sight within the same galaxy[11][14]. For this reason, assuming a common β for all SNe is an oversimplification that can introduce systematics into the calibration process, especially if the dust properties evolve with redshift or if they exhibit a dependence in some of the SN properties used in the standardization. It can thus prove advantageous to individually determine dust properties for each SN Ia, which could then be used to better constrain the color-luminosity relation in the calibration.

As it can be challenging to determine the extinction for SN Ia, especially at high redshifts, the study of SN Ia host galaxies offers an interesting opportunity, not only to tackle the problem of dust induced systematics in the SN calibration, but also to extend our knowledge about general dust properties affecting SN observations. In this work we present an alternative approach to infer dust attenuation laws towards the host galaxies for a cosmological sample of 162 SNe Ia collected as part of the Dark Enery Survey (DES)[15][16].

To achieve this goal, we use both global and local (4 kpc) broadband photometric data in the *griz* filter bands for the SNe hosts, complemented when possible with GALEX[17] UV and 2MASS[18] NIR photometry.

We fit Simple Stellar Population (SSP) models to this data, which are a subset of models that assume that all stars in the considered population were born at the same time from a cloud of homogeneous chemical composition[19]. From these fits, we seek to extract relevant information about the dust properties for each individual galaxy and to explore global tendencies in the data. In particular, we intend to confirm whether there is evidence for the large variation in dust properties previously observed[11].

Furthermore, we study the relation between a host galaxy's attenuation law and its respective SN extinction law, analysing the viability of using our fit results to approximate the latter. In particular, we are interested in the impact of using the values of R_V, inferred for the host galaxies, in a new SNe Ia calibration.

Finally, we explore possible origins of the "mass-step" relation introduced above, analysing whether it can be linked to or described by the attenuation law of the SNe host galaxies.

1.4 Thesis Outline

The present work in organized according to the following structure:

Chapter 1 presents a brief introduction to the topics of SNe Ia in Section 1.1 and astrophysical dust in Section 1.2. It then details the motivation and main objectives of the work, in Section 1.3.

Chapter 2 begins with a brief introduction to Bayesian Inference in Sections 2.1.1 and 2.1.2 and Markov Chain Monte Carlo algorithms in Section 2.1.3. These tools are then applied in the construction of our fitting methodology, which is detailed in Section 2.2. The chapter concludes with Section 2.3, in which the results from fits performed on simulated data are presented. In particular, we examine the impact of using data from different photometric filter bands in the final fit results. This serves as a benchmark performance test of the overall fitting procedure. Full data sets relating to these simulations are presented in Appendix A.

Chapter 3 focuses on obtaining attenuation laws for SNe Ia host galaxies, based on broadband photometric fits. In Section 3.1, we present some background information about the Dark Energy Survey, from which our data was obtained. An overview of this data, which consists of both global and local host galaxy optical photometry is presented in Section 3.2. The fit results for the host galaxies are displayed and discussed in Section 3.3. Finally, in Section 3.4, we once again examine the impact of using from different photometric filter bands in the fitting process, this time on a real data set. Full fit results for this chapter are presented in Appendix B.

In Chapter 4 we discuss the relation between a SN Ia extinction law and its host galaxy attenuation law. We start with Section 4.1 by taking a look at the relation between the extinction law parameters as documented in the literature, comparing it to our own results obtained for the host galaxies. We then move on to Section 4.2, where a more in-depth analysis is performed by looking at the possible correlations between SN Ia light curve parameters and the respective host galaxy attenuation parameters. We conclude the chapter with Section 4.3, in which we analyse both whether a “dust-step” similar to the “mass-step” can be identified in the data and whether performing a new SNe Ia calibration with the values of R_V computed for the hosts has a positive impact on the respective Hubble residuals.

Finally, in Chapter 5, we highlight the conclusions of this work.

Additionally, we include some appendices in which some important concepts are introduced, namely Appendix C, which contains an explanation of Kron aperture photometry, and Appendix D, which details the process of Guassian Processes Regression.

Chapter 2

Fitting Methodology

As highlighted in Section 1.3, we are interested in fitting Simple Stellar Population (SSP) models to the photometric data for the host galaxies of a set of DES SNe Ia. To do this, we compute the Spectral Energy Distributions (SED) for each SSP and compare with the observed data. Given both the complexity of the models used and the limited amount of photometric data, we rely on Bayesian inference methods for this fitting process, which is accomplished using the **Prospector**[1] [20] Python package.

2.1 Bayesian Inference

2.1.1 Bayes' Theorem

Before delving deeper into statistical inference methods, we must first familiarize ourselves with Bayes' Theorem. Given two statistical events A and B that occur with probability $P(A) > 0$ and $P(B) > 0$, we can define the conditional probability of A given that B has occurred as:

$$P(A|B) = \frac{P(A \cap B)}{P(B)} \tag{2.1}$$

Taking into account that $P(A \cap B) = P(B \cap A)$, we can then write:

$$P(A \cap B) = P(A|B)P(B) = P(B|A)P(A) \tag{2.2}$$

This expression then leads to Bayes' Theorem in its usual form:

$$P(B|A) = \frac{P(A|B)P(B)}{P(A)} \tag{2.3}$$

It should be noted that Bayes' Theorem can be equally applied to continuous random variables.

[1] https://github.com/bd-j/prospector

2.1.2 Inference

Statistical inference is a method by which one can learn about the underlying processes behind a given observed data set from that same data. Bayesian inference is one of these methods and it is based on Bayes' Theorem.

For the purposes of this work, we will focus on inference with parametric models. To do this, we start by assuming that we have a data set D comprised of N total data points, which can be modeled using a probability distribution function (pdf) $p(D|\boldsymbol{\theta})$, which depends on a given parameter vector $\boldsymbol{\theta}$. From here, once we have actually observed the data, we can define the likelihood function for $\boldsymbol{\theta}$:

$$\mathcal{L}(\boldsymbol{\theta}) = p(D_{obs}|\boldsymbol{\theta}) \tag{2.4}$$

This quantity is often misinterpreted, so it is important to clearly define it. Although it is a function of $\boldsymbol{\theta}$, it does not represent a pdf for these parameters. Rather, we can think of it as the conditional probability for the observed data for any given values of $\boldsymbol{\theta}$. One common definition for $\mathcal{L}(\boldsymbol{\theta})$ is given by Eq. 2.5, where $\Delta(\boldsymbol{\theta})$ is defined as the difference between the observations and the fitted model and σ^2 accounts for observation errors in D_{obs}.

$$\mathrm{Ln}(\mathcal{L}(\boldsymbol{\theta})) = -\frac{1}{2}\sum_{i=0}^{N}\left(\frac{\Delta(\boldsymbol{\theta})_i^2}{\sigma_i^2} + \ln(2\pi\sigma_i^2)\right) \tag{2.5}$$

The next step in the process is to describe the parameters $\boldsymbol{\theta}$ that control the model. We do this by defining a set of pdf's $p(\boldsymbol{\theta})$ known as priors. These functions essentially describe the information we have about $\boldsymbol{\theta}$ before looking at the data. We can either have vague priors, such as an uniform distribution, which only prescribes a range for $\boldsymbol{\theta}$, or more informative ones, which can be tailored to reflect more nuanced distributions or even relations between different parameters.

Inference can therefore be thought of as a process of updating the prior based on observed data. We call this updated pdf $p(\boldsymbol{\theta}|D_{obs})$ the posterior and it can be obtained from the application of Bayes' Theorem:

$$p(\boldsymbol{\theta}|D_{obs}) = \frac{p(D_{obs}|\boldsymbol{\theta})p(\boldsymbol{\theta})}{p(D_{obs})} \tag{2.6}$$

The previous expression contains a quantity $p(D_{obs})$ which we have not yet described. This quantity is known as the predictive prior and acts simply as a normalization constant.

It should be noted that, although pdfs are much more informative, there are some occasions where it can be helpful to refer to a single *best-fit* value for a given parameter. In these cases, we will take this value to be the median of the distribution, with the uncertainty range given by the 16th and 84th percentiles, defining a 68% credible region.

Despite being a powerful method for gaining insight into the underlying mechanisms behind a data set, there are some drawbacks to Bayesian inference. On one hand, the predictive prior is, in general, difficult to calculate and, on the other hand, the calculation of the posterior requires the computation of the likelihood over the entire parameter space, which can be both taxing and time consuming, especially

as the number of model parameters increases. In the following section, we will explore a solution that allows us to get around both of these problems - sampling.

2.1.3 Sampling Algorithms

Sampling is a process which essentially allows one to reconstruct a distribution based only on a set of discrete values for $\boldsymbol{\theta}$. This solves one of the problems we encountered, as the computation of the likelihood over the entire parameter space is no longer necessary. There are several different ways to achieve this, but we will focus on the Metropolis–Hastings Markov Chain Monte Carlo (M-H MCMC) algorithm[21].

This algorithm works by producing a biased random walk through parameter space, which will tend to converge towards values of $\boldsymbol{\theta}$ that maximize the posterior pdf. This means that we will end up with a discrete set of K values of $\boldsymbol{\theta}$, known as a chain or a walker[2]. From this walker one can then obtain a fairly close reconstruction of the posterior distribution.

Three ingredients are needed to build the algorithm: The first is the function to be sampled, in this case $p(\boldsymbol{\theta}|D_{obs})$. The second is a proposal pdf function, $q(\boldsymbol{\theta}'|\boldsymbol{\theta})$, which is used to generate a new position $\boldsymbol{\theta}'$ in the parameter space given an "old" position $\boldsymbol{\theta}$. The third is an initial set of parameters $\boldsymbol{\theta}_0$.

For a given set of samples, the most recent iteration of which is $\boldsymbol{\theta}_k$, the algorithm to generate $\boldsymbol{\theta}_{k+1}$ is thus:

1. Draw a proposal $\boldsymbol{\theta}'$ from $q(\boldsymbol{\theta}'|\boldsymbol{\theta})$;
2. Draw a random number $0 < r < 1$ from a uniform distribution;
3. Compute $R = \frac{p(\boldsymbol{\theta}'|D_{obs})}{p(\boldsymbol{\theta}_k|D_{obs})}$.
4. - If $R > r$, then the new value is accepted and $\boldsymbol{\theta}_{k+1} = \boldsymbol{\theta}'$.
   - If $R < r$, then the new value is rejected and $\boldsymbol{\theta}_{k+1} = \boldsymbol{\theta}_k$.

Notice that by calculating the ratio $\frac{p(\boldsymbol{\theta}'|D)}{p(\boldsymbol{\theta}_k|D)}$ we completely eliminate the need to compute the predictive prior, which takes care of our second problem.

There are a number of steps that can be taken to improve on the M-H MCMC algorithm. First of all, it is possible to increase the number of walkers used. This essentially means we will end up with several (mostly) independent chains of K values of $\boldsymbol{\theta}$ from which to reconstruct the posterior. This can be used to mitigate the pitfall of local maxima in the posterior, in which some of the walkers might get stuck.

Second of all, the initial iterations of each walker are highly dependent on the initial values of the algorithm and hence are not representative of the posterior distribution. For this reason, it is common to perform an initial sampling with $n_{\text{burn-in}}$ interactions, whose values are discarded to eliminate any possible bias. This is known as the burn-in. The proper walkers can then be re-initialized based on the results from this burn-in round. In the case of **Prospector**, several burn-in rounds can be performed, with the

[2]The terms chain and walker are sometimes used interchangeably, but there is a small difference between the two. Essentially, a walker is a regular chain for which the proposal distribution depends on the positions of all the other walkers[22].

walker distribution being re-initialized after each round according to a multivariate Gaussian derived from the best 50% of the walkers from the previous round.

Additionally, one can improve on the choice of initial values $\boldsymbol{\theta}_0$ by performing a set of initial minimizations on the data. Although not as accurate as Bayesian inference, these minimizations can provide useful insights about the general region where the walkers should be initialized. Performing multiple minimizations and taking the result with the highest posterior value once again helps to avoid local maxima. It should also be noted that in order to assure a correct sampling of the parameter space, not all walkers should be initiated on the exact result of the initial minimization. Rather, each walker should be initiated within a certain radius around the minimization results. For each parameter, this radius is known as the initial dispersion D_θ.

It should be noted that, although Bayesian fitting does not itself impose a limit on the number of free parameters $\boldsymbol{\theta}$ present in the fitting model, the minimization step enforces a maximum number of free parameters equal to the number of data points in the fit.

The Bayesian inference methods detailed in this work were implemented using the **emcee**[3] Python package[23]. After extensive testing, we settled on the following configuration for the algorithm:

- 20 initial minimizations;
- 128 walkers;
- 3 initial rounds of burn-in, with 16, 32 and 64 iterations, respectively;
- 1024 iterations for each walker (after burn-in).

2.2 Simple Stellar Population Models

Now that we have a grasp on Bayesian inference, we can start to build the models with which to calculate $\Delta(\boldsymbol{\theta})$ in the likelihood function, as defined in Eq. 2.5. For this work, we will use SSP models, which assume that all stars in the considered population were born at the same time from a cloud of homogeneous chemical composition[19]. In particular, we will loosely follow the PROSPECTOR-α model[20], with some variations, referring to the Padova isochrones[24] to build the model. In the following sections we present a detailed overview of the model used, which was generated using both the **FSPS**[4][25][26] FORTRAN code and the **python-FSPS**[5] Python package.

2.2.1 Stellar Mass

In our model, radiation sources are powered by their total mass. For practical purposes, we do not concentrate on the masses of individual sources, but rather on the total stellar mass $M_\star$ of the galaxy or galactic region in which they are located. The main contribution of this stellar mass to the SED is to set the overall normalization.

[3] https://github.com/dfm/emcee
[4] https://github.com/cconroy20/fsps
[5] https://github.com/dfm/python-fsps

The distribution of the stellar mass in a galaxy can be described by an empirical initial mass function (IMF), from which the present day mass distribution can be obtained by simulating the evolution of the population. For the purposes of this model, we use a Kroupa (2001) IMF[27].

The stellar mass is a parameter which is fairly easy to constrain based on observed data, even while other parameters might exhibit some degeneracy among themselves. For this reason, in some of the subsequent analysis where the available photometric data might prove insufficient for a more complete fit, we will treat the stellar mass as a fixed parameter. In these cases, we will use previously obtained values for these masses, which should not impact the quality of our results.

For the cases in which the mass is left as a free model parameter, we assume a flat top-hat prior on the logarithm of the mass over the range $8 < \mathrm{Log}(M_\star/M_\odot) < 12$, which covers typical mass values for galaxies. Additionally, we chose an initial dispersion $D_{\mathrm{Log}(M_\star/M_\odot)} = 11$. This value, despite being relatively large, proved the best at sampling the full parameter space. The burn-in iterations allow the walkers to converge to a much smaller range of values by the time the actual sampling begins, which means the large initial dispersion does not impact the recovered posterior distribution.

2.2.2 Star Formation History

The star formation history (SFH) describes how stars form over time and space in a given galaxy. This is relevant to the SED, as young stellar populations tend to exhibit a bluer spectrum, as massive and short-lived stars dominate the emission, while older populations tend to exhibit a redder spectrum, since the more massive stars have died out and the low mass stars are reaching the end stages of their evolution [28]. In this work, we will adopt a delayed τ-model, such that the SFH is described by an exponentially decreasing star formation rate (SFR), with e-folding time τ:

$$SFR(t) = te^{-t/\tau} \tag{2.7}$$

The previous expression is normalized such that a total of one solar mass of stars is formed over the full SFH. Additionally, t is the time measured forward from the beginning of the Universe up to the actual age of the stellar population t_{age}.

Although there are some disadvantages associated with using a parametric SFH[29], they are not entirely relevant for this analysis, as we always treat the SFH parameter as a fixed value, with $\tau = 1$Gyr.

Contrastingly, the age parameter t_{age} is always left free. For this parameter, we choose a flat top-hat prior over the range $0.001 < t_{\mathrm{age}} < 13.8$ Gyr, so as to only consider solutions younger than the age of the Universe. Additionally, we choose $D_{t_{\mathrm{age}}} = 5$ Gyr for the initial age dispersion.

2.2.3 Stellar Metallicity

Stellar metallicity Z is defined as the abundance of elements heavier than helium in a star. It mainly affects the optical to near-infrared (NIR) flux ratio, which is of great importance when determining dust attenuation. For this reason, metallicity is always introduced as a free parameter in our model.

When performing a fit, it is typically assumed that all the stars in the model galaxy have a single stellar metallicity $Z_\star$. However, since we recover a metallicity distribution rather than a discrete value, this assumption ends up being somewhat relaxed, allowing for a more general description.

We choose a flat top-hat prior on the logarithm of the metallicity over the range $-2 < \mathrm{Log}(Z_\star/Z_\odot) < 2.5$. This range is mostly determined by the coverage of the Padova isochrones[24], which covers $-2 < \mathrm{Log}(Z_\star/Z_\odot) < 0.2$. Nevertheless, we extend the upper limit in our prior to assure a more complete sampling of the parameter space. Additionally, we choose $D_{\mathrm{Log}(Z_\star/Z_\odot)} = 2$.

2.2.4 Dust Attenuation

The impacts of dust attenuation on a SED and its parametrization have already been discussed in the previous chapter. In our model we will be referring to a modified version of the attenuation curve derived by Calzetti for nearby starburst galaxies[30]. The original curve takes the form:

$$k(\lambda) = \begin{cases} 2.659(-2.156 + 1.509/\lambda - 0.198/\lambda^2 + 0.011/\lambda^3) + R_{V,0}, & \text{if} \quad 0.12\mu\mathrm{m} \leq \lambda \leq 0.63\mu\mathrm{m} \\ 2.659(-1.857 + 1.040/\lambda) + R_{V,0}, & \text{if} \quad 0.63\mu\mathrm{m} \leq \lambda \leq 2.20\mu\mathrm{m} \end{cases} \tag{2.8}$$

where $k(\lambda)$ follows Eq. 1.14 and $R_{V,0} = 4,05$ is the total-to-selective attenuation for the Calzetti law. There are however a few shortcomings of this attenuation law, which we will now address.

Firstly, observations show that this curve can be insufficient to describe attenuation processes for star-forming galaxies, in particular at higher redshifts. In these cases there is evidence of a so-called UV bump at around 2175Å[31]. For this reason, the original Calzetti curve is modified by the addition of this same bump, modelled by a Lorentzianlike "Drude" profile:

$$D(\lambda) = \frac{E_{bump}\lambda^2\gamma^2}{(\lambda^2 - \lambda_0^2)^2 + \lambda^2\gamma^2}, \tag{2.9}$$

where $\lambda_0 = 2175$Å is the central wavelength, $\gamma = 350$Å is the FWHM of the bump and E_{bump} is the amplitude[31]. We will further discuss this amplitude shortly.

Secondly, the modified attenuation law is also multiplied by a power law $\left(\frac{\lambda}{\lambda_V}\right)^n$ in order to produce different slopes without the need to alter τ_V. The slope, therefore, ends up being effectively controlled by the diffuse dust attenuation index n[31].

There is strong evidence of a relation between the steepness of the attenuation curves and the strength of the UV bump[32]. This effectively means that E_{bump} exhibits a dependency in n, which, for our purposes, can be described by:

$$E_{bump} = 0.85 - 1.9n. \tag{2.10}$$

Taking these corrections into account, the moddified Calzetii attenuation law becomes[31]:

$$\tau(\lambda) = \frac{\tau_V}{R_{V,0}}[k(\lambda) + D(\lambda, n)]\left(\frac{\lambda}{\lambda_V}\right)^n. \tag{2.11}$$

The shape of this attenuation curve is plotted in Fig. 2.1 for different values of n. As previously men-

tioned, this parameter control the general slope of the curve. The more negative n is, the larger the attenuation for the bluer wavelengths, which translates to a larger level of reddening.

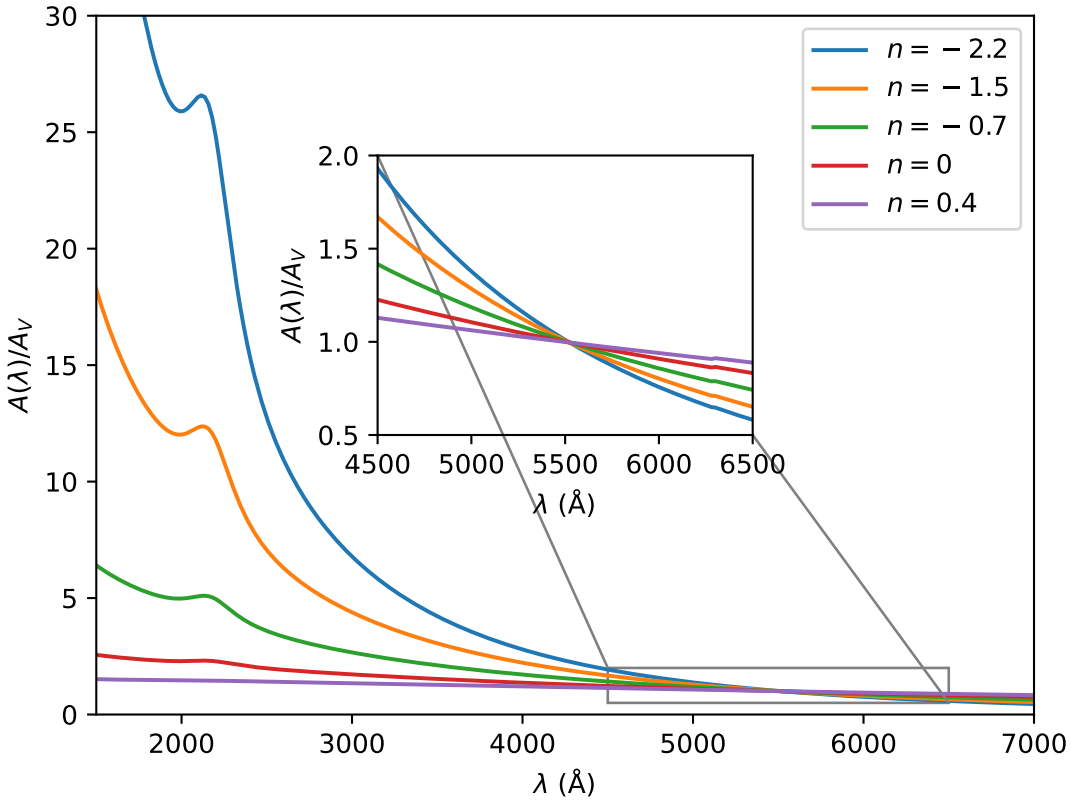

Figure 2.1: Normalized modified Calzetti attenuation curve as a function of the wavelength λ, plotted for different values of the dust index n: the curve for $n = -2.2$ is shown in blue; the curve for $n = -1.5$ is shown in orange; the curve for $n = -0.7$ is shown in green; the curve for $n = 0$ is shown in red; and the curve for $n = 0.4$ is shown in purple. A smaller section of the curve, focused on the region $\lambda \sim \lambda_V$ is also plotted.

The diffuse dust attenuation law for this model will then be parametrized by Eq. (2.11), with τ_V and n acting as free parameters. For the purposes of this work, we will disregard the birthcloud component.

In the case of τ_V, we adopt a flat top-hat prior over the range $0 < \tau_V < 6$ to account for a fairly large range of optical depths. Additionally, we choose $D_{\tau_V} = 1$.

In the case of n, we also adopt a flat top-hat prior, this time over the range $-2.2 < n < 0.4$ to account for the typical slopes in attenuation curves. As is apparent from Fig. 2.1, the upper limit is chosen so that we do not end up with a flat attenuation curve, which would cause $\tau(\lambda)$ to be nearly fully degenerate with the normalization of the SED[20]. For the initial dispersion in n, we choose $D_n = 1$.

2.2.5 Redshift

Redshift z must be accounted for in our model, in order to make sure the effects of the expansion of the Universe are represented in the SED. For each SN host, the redshift is treated as a fixed parameter, as

the DES galaxies have spectroscopically confirmed redshifts[16][33].

2.2.6 Parameter Correlations and Degeneracies

We close our discussion of SSP models by addressing two different concerns related to the model parameters.

Firstly, as previously mentioned, all the prior distributions for the model parameters are flat, either for the parameter itself or its logarithm. This, in a sense, constitutes the most agnostic form for a prior, as only the parameter range is constrained. There is, however, an argument to be made for making full use of the priors by making them more informative, mainly by taking advantage of some well know relations between different parameters.

For instance, due to the build-up of heavy elements with the passing of cosmic time, an age-metallicity relationship is expected to be present for the studied galaxies. On the same note, relations between the optical depth and the dust index have also been reported[34]. These relations could be easily translated into more informative priors, at the cost of imparting a level of bias into our fit results. For this reason, rather than implementing these relations a priori, we choose flat priors so as to be sure that any relations found in the fitting process have not been forced.

Secondly, galaxy SEDs are, as we have seen, the result of many complex physical variables. For this reason, it can be difficult to uniquely determine the fit parameters in individual galaxies with only broadband optical photometry, which can lead to degeneracies between some of the parameters. Of furthermost relevance to this work is the well known age-dust-metallicity degeneracy. The inclusion of additional UV or NIR photometric information in the fits might be one way to possible mitigate this effect. We will explore this possibility further on, should these degeneracies prove too severe.

As a final note, it is important to highlight that, although they might appear similar, parameter correlation and parameter degeneracy are two distinct concepts. On one hand, parameter correlations cribe global relations that become apparent when looking at a full data set. In this way, they are reflections of the underlying physical mechanisms behind the data. On the other hand, parameter degeneracies are artefacts implicit in the fitting process for individual galaxies, apparent when examining the recovered posterior distributions.

2.3 Test Simulations

With the fitting methodology laid down, we would like to perform some tests to see how accurately it can recover the model parameters from broadband photometric data. We do this by performing fits on a simulated galaxy population.

The first step of the test is therefore to simulate galaxy SEDs from which to extract the relevant photometric data. We do this by once again using **FSPS**, employing the same SSP model as described in the previous section, with the values for $M_\star$, $Z_\star$, t_{age}, τ_V, n, and z being drawn from a series of statistical distributions. For the first 5 quantities, these distributions were taken to be the same as the

respective priors, simply because they accurately covered the parameter space without a bias toward any specific region. In the case of the redshift, we choose a flat top-hat distribution over the range $0 < z < 0.6$, which closely resembles the real range we will be working with.

According to this process, a population of 75 mock galaxies was generated. A full list of the parameters used in these simulations is displayed in Table A.1. It should be noted that this simulated population does not necessarily resemble an actual SNe Ia host population, as we are merely interested in testing the performance of the fitting method across the full parameter space.

From the resulting SSP models, SEDs for each galaxy were generated. These were then used to extract broadband photometry in the DECam *griz* filter bands[6][33][35], with the magnitude in each filter band ν given by f_ν. Additionally, a degree of statistical noise σ_ν was applied to the photometric data in accordance with a prescribed signal-to-noise ratio (SNR) of 10. This value was chosen to roughly reflect the minimum SNR of the DES data set[16]. By applying this degree of noise we can thus better match the observational conditions, where such noise is inherent and unavoidable. We therefore have:

$$\sigma_\nu \sim \mathcal{N}(0,1) \times \frac{f_\nu}{\text{SNR}}, \tag{2.12}$$

where $\mathcal{N}(0,1)$ is a Gaussian distribution with mean 0 and standard deviation 1.

For each galaxy we now have 4 slightly noisy photometric data points to which we want to fit a SSP model and are therefore limited to 4 free fit parameters. For this reason, both the redshift and the stellar mass for the galaxies will be treated as fixed parameters, as previously discussed. Both of these values will therefore be set to their "true" values, that is, the values used to generated the simulated photometry.

In this sense, this represents the ideal scenario for our fitting methodology, as not only does the fitted model perfectly describe the data generation process, but also some parameters are already fixed at their true values. This is one of the reasons why the introduction of statistical noise is so important, to make sure the fits can handle some variations.

Some examples for the fitted posterior distributions, as well as the respective *best-fit* values, are shown in Figs. 2.2 and 2.3. The "true" simulation parameters are also shown for easy comparison. The first figure represents a best case scenario in which all the posterior distributions converged to a well defined shape with a clear maximum which roughly matches the original simulation value. The second figure displays a less ideal scenario in which the convergence was not as good, which results in somewhat muddled shapes for the posterior distributions. In addition, some of the original parameters are out of the credible interval prescribed by the *best-fit* values.

It is worth pausing at this moment to once again consider the inherent degeneracies present in the fitting process, which Bayesian inference is particularly apt at making explicit. Looking at Fig. 2.2, for example, we can see that the age-dust degeneracy is clearly evident in the corresponding two-dimensional posterior distributions. A degeneracy between both dust parameters is also observed. These degeneracies are also somewhat apparent in Fig. 2.3, although not as clearly.

Looking now once again at the full fitted results, which is displayed in Table A.2, we can say that the majority of the 75 test galaxy fits converged adequately. Given that each fit was performed using only

[6] http://www.ctio.noao.edu/noao/node/13140

data from 4 filter bands, this is a result much better than initially expected and points to the fact that the fitting methodology is indeed adequate to solve the problem at hand.

The fit residuals, which are given by the difference between the *best-fit* and the simulation value are plotted in Fig. 2.4. The values of *RMS* obtained when comparing the fitted and simulation values are also shown. Looking at the residuals, we can see that, in general, they are very close to 0. The values of *RMS* obtained are also relatively low, especially for the two dust parameters. There appear to be some problems in the fit when dealing with larger absolute values of $\mathrm{Log}(Z_\star/Z_\odot)$, but this does not appear to greatly impact the corresponding fitted dust parameters.

Despite the relatively high quality of the fit, however, there is still room for improvement. The logical solution is the inclusion of more photometric data, which would allow for both a better convergence of the walkers and also the promotion of the stellar mass to a free parameter. This would be ideal when dealing with real data.

We will thus investigate the effect of including extra photometry in both the Ultraviolet (UV) and Near-Infrared (NIR) ranges, namely in the GALEX *NUV*/*FUV*[7][17] and 2MASS *JHKs*[8][18] filter bands. This photometric information can be easily obtained from the simulated SEDs, following the procedure

[7] https://asd.gsfc.nasa.gov/archive/galex/Documents/instrument_summary.html
[8] http://svo2.cab.inta-csic.es/theory/fps/index.php?id=2MASS

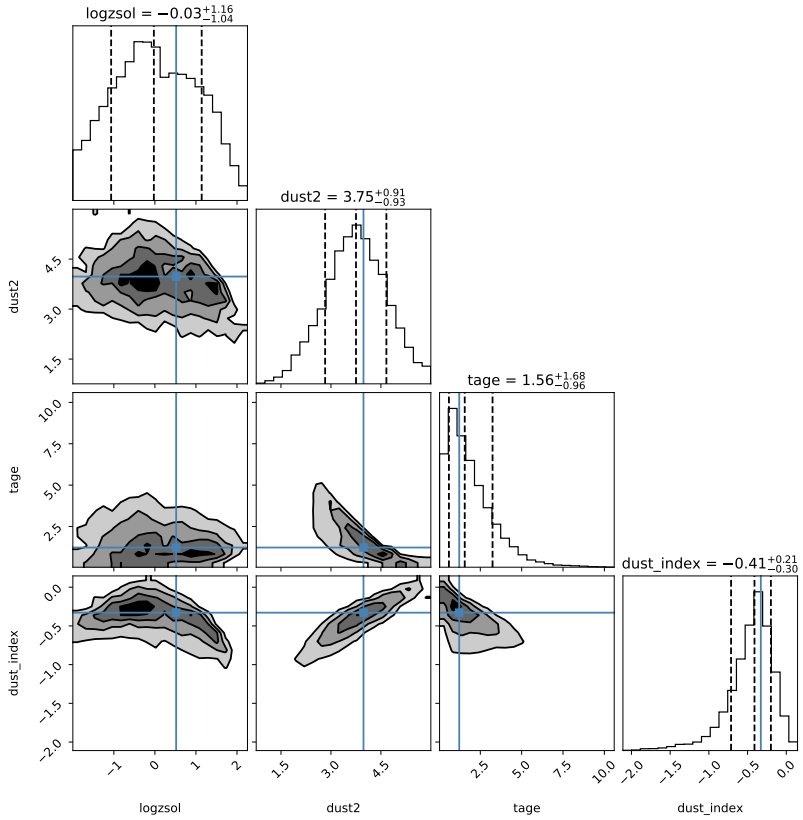

Figure 2.2: One and two-dimensional posterior distributions for the 5th simulated galaxies with an accurate fit. The dashed black lines show the median as well as the 16th and 84th percentiles for each of the one-dimensional distributions. The “true” value of each parameter is shown in blue. The *best-fit* values for each parameter are also indicated on the top of each distribution.

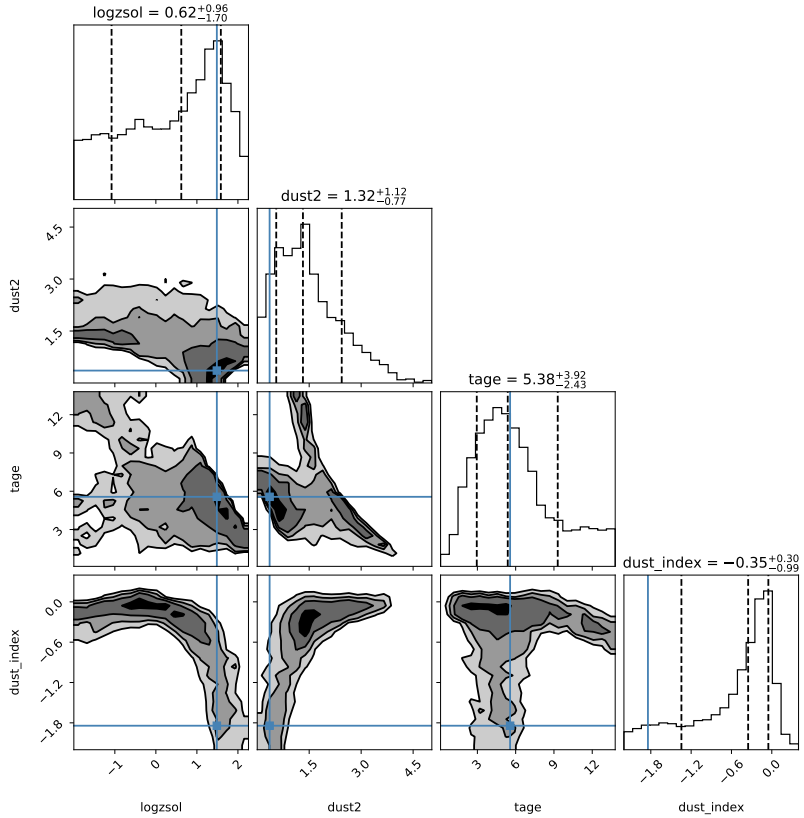

Figure 2.3: One and two-dimensional posterior distributions for the 3rd simulated galaxies with an inaccurate fit. The dashed black lines show the median as well as the 16th and 84th percentiles for each of the one-dimensional distributions. The "true" value of each parameter is shown in blue. The *best-fit* values for each parameter are also indicated on the top of each distribution.

detailed above.

Fits were performed using the following filter combinations:

1. DECam *griz* and GALEX *NUV*/*FUV*;
2. DECam *griz* and 2MASS *JHKs*;
3. DECam *griz*, GALEX *NUV*/*FUV* and 2MASS *JHKs*;

The residuals for these fits are displayed in Figs. 2.5, 2.6 and 2.7, respectively. Once again, the respective values of RMS are also plotted.

As expected, there is a noticeable improvement in the fits when GALEX photometry is introduced, with the case with both GALEX and 2MASS data leading to the best overall fit. However, it is curious to notice that the introduction of 2MASS photometry on its own makes for slightly worse fits, as evidenced by the values of RMS. This might seem counter-intuitive, but it is most likely a consequence of including an excess of NIR data without corresponding UV data to balance the spectrum and help break any degeneracies, which can result in a skewed fitted SED.

Overall, it is reasonably to conclude that, by and large, broadband optical photometry is sufficient to accurately determine dust properties for SN host galaxies. In cases where it is available, UV photometry

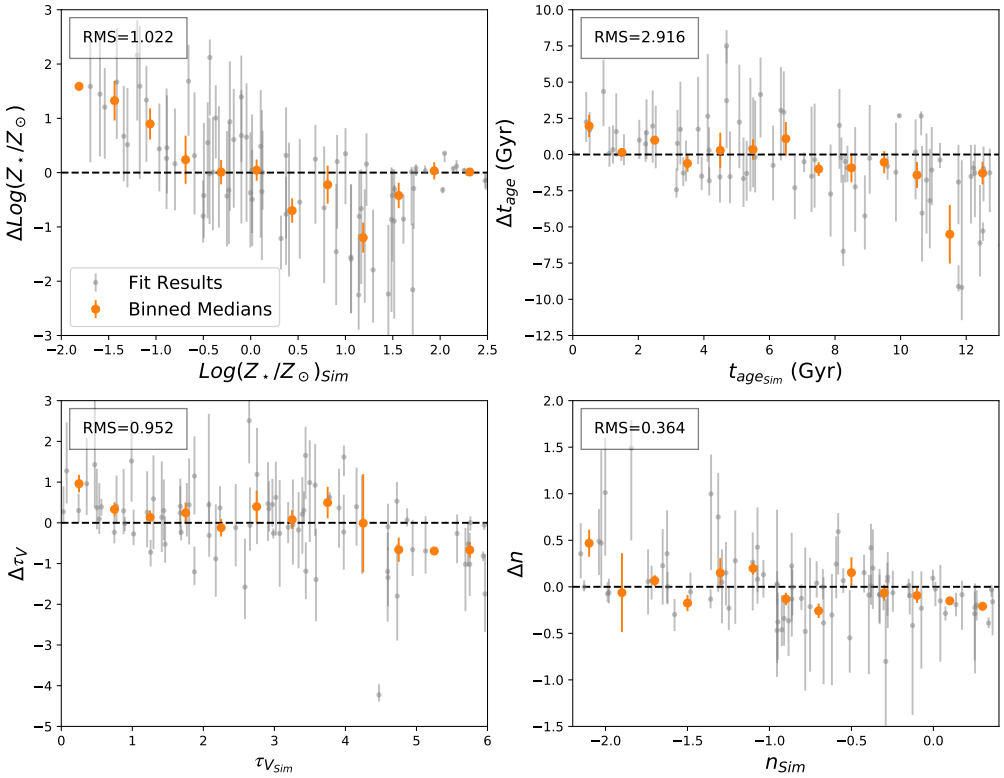

Figure 2.4: Residuals for the *best-fit* values for the test galaxies DECam *griz* fits as a function of the original parameters. From top to bottom and left to right we have: Log($Z_\star/Z_\odot$), $t_{\rm age}$, τ_V and n. Results for the different galaxies are shown in grey. Binned medians for each parameter are shown in orange. The corresponding values of RMS for each parameter are also plotted in the top left corner.

has been shown to marginally improve the fitting results. The same is true for NIR photometry, provided it is balanced out by UV data. With the tests concluded, we will now move on to a real data set.

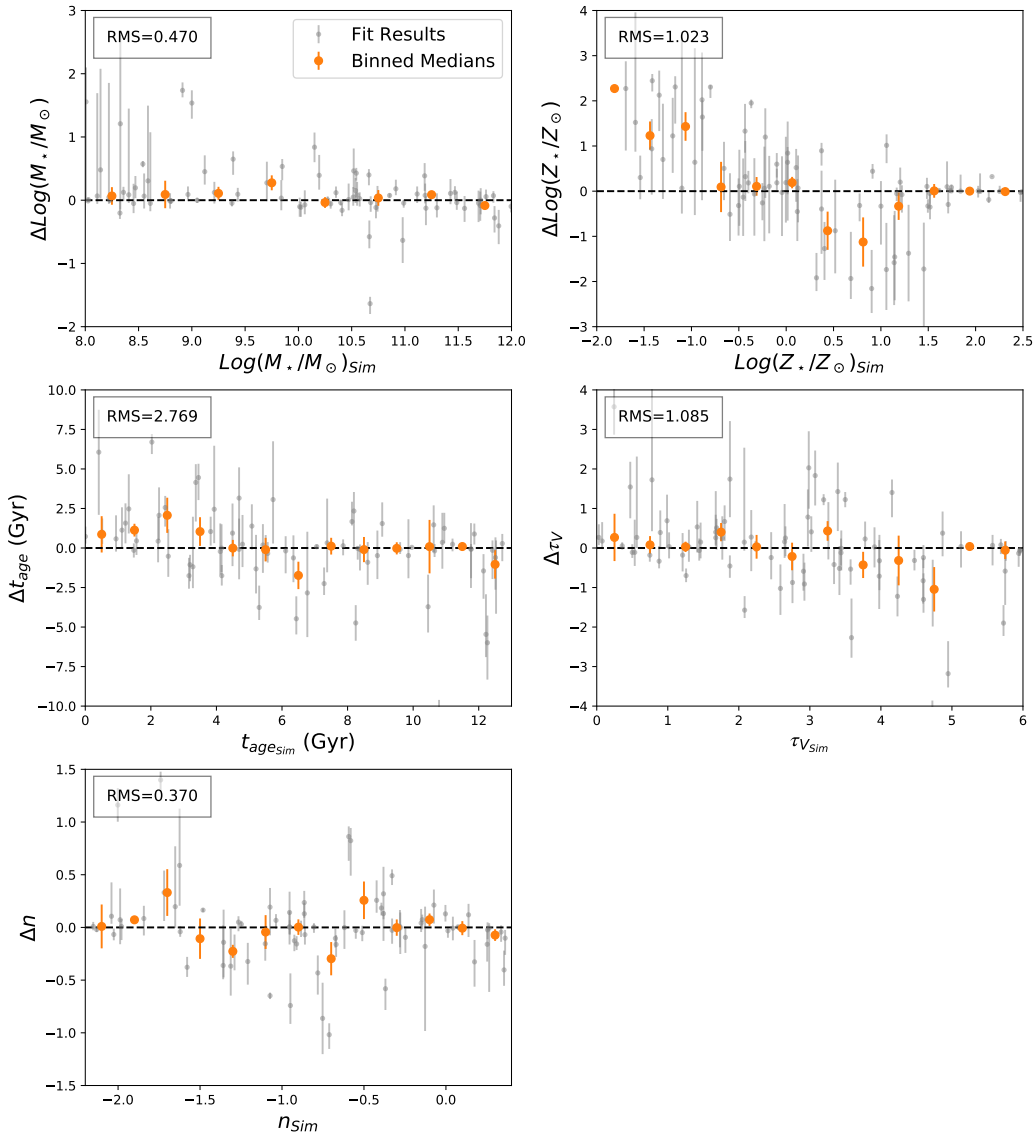

Figure 2.5: Residuals for the *best-fit* values for the test galaxies GALEX *NUV*/*FUV* and DECam *griz* fits as a function of the original parameters. From top to bottom and left to right we have: Log($M_\star/M_\odot$), Log($Z_\star/Z_\odot$), $t_{\rm age}$, τ_V and n. Results for the different galaxies are shown in grey. Binned medians for each parameter are shown in orange. The corresponding values of RMS for each parameter are also plotted in the top left corner.

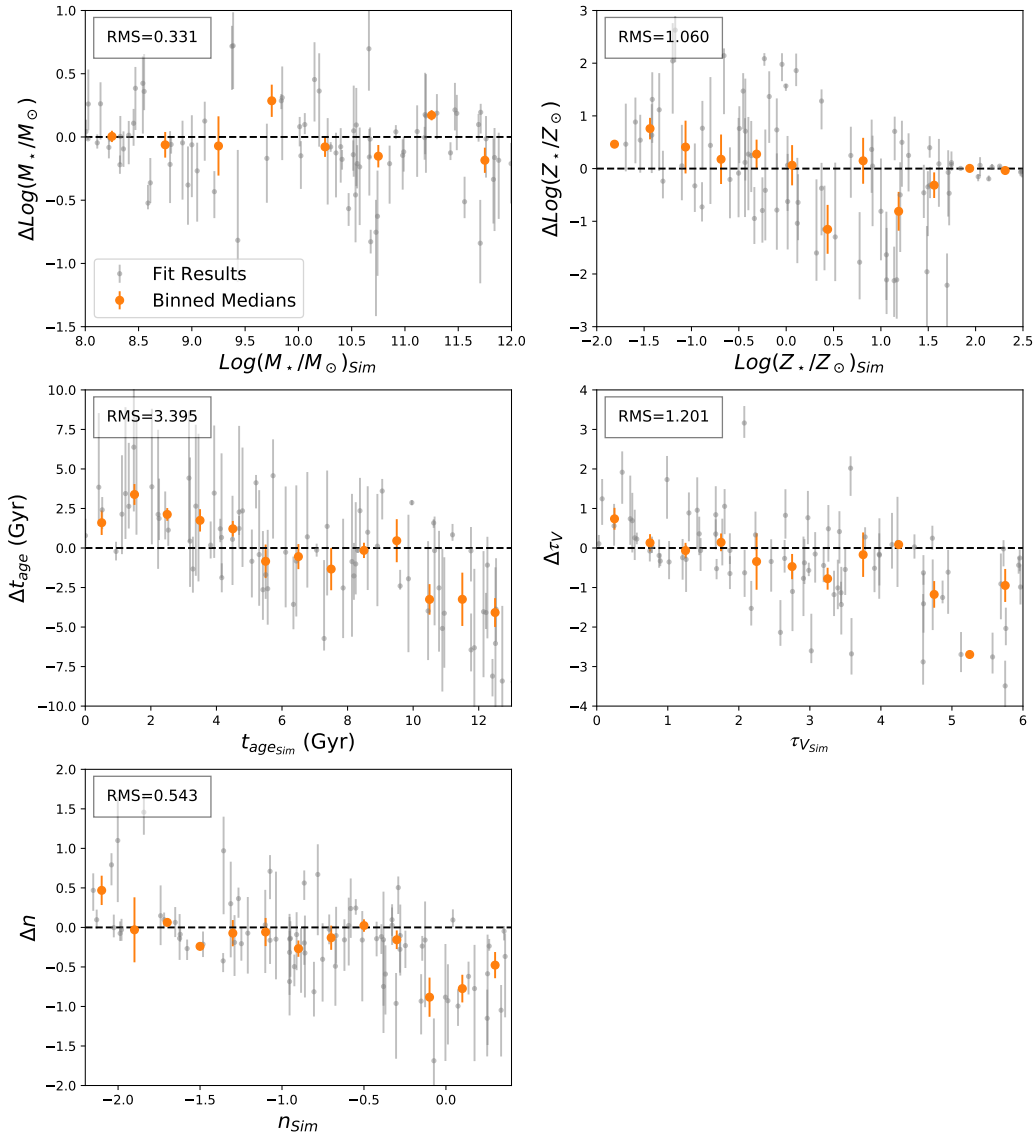

Figure 2.6: Residuals for the *best-fit* values for the test galaxies 2MASS *JHKs* and DECam *griz* fits as a function of the original parameters. From top to bottom and left to right we have: Log($M_\star/M_\odot$), Log($Z_\star/Z_\odot$), $t_{\rm age}$, τ_V and n. Results for the different galaxies are shown in grey. Binned medians for each parameter are shown in orange. The corresponding values of RMS for each parameter are also plotted in the top left corner.

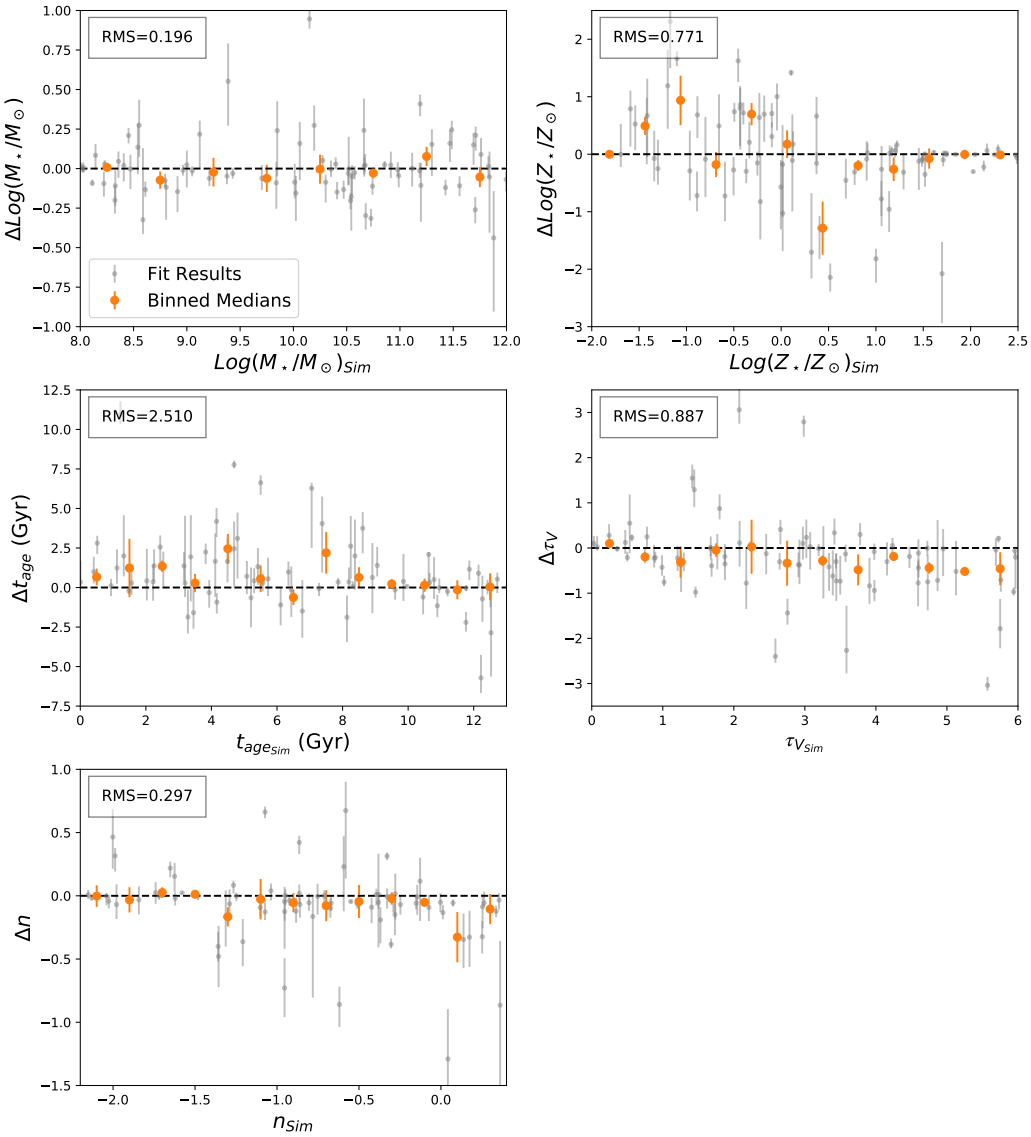

Figure 2.7: Residuals for the *best-fit* values for the test galaxies GALEX *NUV*/*FUV*, 2MASS *JHKs* and DECam *griz* fits as a function of the original parameters. From top to bottom and left to right we have: Log($M_\star/M_\odot$), Log($Z_\star/Z_\odot$), $t_{\rm age}$, τ_V and n. Results for the different galaxies are shown in grey. Binned medians for each parameter are shown in orange. The corresponding values of RMS for each parameter are also plotted in the top left corner.

Chapter 3

Dust Attenuation for DES Galaxies

The present chapter will focus on obtaining dust attenuation laws for a set of SNe Ia host galaxies, based on the fitting framework discussed in Chapter 2.

3.1 The Dark Energy Survey

The Dark Energy Survey (DES) is a collaborative imaging survey covering $\sim$ 5100 square degrees of the southern hemisphere using the 4-m Blanco telescope at the Cerro Tololo Inter-American Observatory (CTIO), equipped with the 520 megapixel wide-field Dark Energy Camera [36] with a 0.263 arcsecond per pixel resolution. Among its objectives are the mapping of galaxies and the detection of supernovae. In particular, the program includes a five-year transient survey (DES-SN), optimised for the detection and measurement of SNe Ia for cosmology.

In this section we will look at data collected as a part of the first three-year cosmological sample of the survey (DES3YR). Particularly, we will focus on a set of 162 spectroscopically-confirmed SNe Ia, as well as their respective host galaxies. This particular data set, which is only a small part of the full data release[1][9], covers a redshift range of $0.077 < z < 0.58$ and includes broadband photometry for the host galaxies in the DECam *griz* filter bands[16][33][35].

3.2 DES Photometric Data

When studying SNe Ia and their respective hosts, it is common to focus on a galaxy's global photometry. However, there is evidence for a connection between the intrinsic properties of SNe Ia and the characteristics of their local environment[33]. For this reason, in this work we will look at both global and local photometric data, originally computed by Kelsey (2020)[16].

[1] https://www.darkenergysurvey.org/des-year-3-supernova-cosmology-results/

3.2.1 Global Photometry

The global photometry for each host galaxy was measured from stacked images using **SOURCE EXTRACTOR**[37], employing Kron FLUX_AUTO measurements, that is, integrating pixel values within an adaptively scaled aperture, derived from Kron's "first moment" algorithm[38]. A detailed explanation of this method is provided in Appendix C.

A detection image was used to set the aperture, which ensures the aperture is the same for the measurements in each filter. The measurements were also corrected for Milky Way dust extinction using Schlegel dust maps[39] and a Fitzpatrick extinction law[40] with coefficients $R_g = 3.186$, $R_r = 2.140$, $R_i = 1.569$ and $R_z = 1.196$[16].

3.2.2 Local Photometry

In the case of local photometry, the aperture photometry tool from the **PHOTUTILS** Python module [41] was used. The resulting fluxes were corrected for Milky Way extinction in the same way as described above[16].

Since we are interested in capturing a snapshot of the local stellar environment near the SN Ia we would, in theory, look for an aperture as small as possible. There are, however, some limitations to keep in mind.

In particular, we must keep in mind the effects of atmospheric seeing, which refers to the distortion of astronomical light due to turbulence in the atmosphere. Seeing is usually parameterized by the full-width half-maximum (FWHM) of the point spread function (PSF) of the observed stars. This PSF essentially describes the response of the telescope to a point source by defining a two-dimensional distribution of light in the telescope's focal plane. For the purposes of this data set, a maximum threshold FWHM of $1.3''$ was assumed for the seeing[16]. This value essentially puts a limit on how small our aperture can be. In particular, if we assume a Gaussian form for the PSF, then we have:

$$\text{FWHM} = 2\sqrt{2\ln(2)}\sigma, \tag{3.1}$$

where σ can be thought of as the smallest useful aperture radius. This value defines the smallest aperture within which objects can be correctly resolved. For FWHM$= 1.3''$, we find a smallest useful aperture radius of $\sigma = 0.55''$. To translate this into a common physical aperture size, we look at our redshift range. For a given value of z, the relation between an object's physical size R and its observed angular size σ_R is given by:

$$d_A \simeq \frac{R}{\sigma_R} \tag{3.2}$$

In the previous equation, d_A is simply the angular diameter distance which, using the same cosmological model defined in Section 1.1, is a function of the redshift z, given by:

$$d_A(z) = \frac{c}{1+z}\int_0^z \frac{dz'}{H_0\sqrt{\Omega_m(1+z')^3+\Omega_\Lambda}} \tag{3.3}$$

As shown in Fig. 3.1, a 4 kpc aperture only becomes smaller than a $0.55''$ radius near $z \simeq 0.7$[16], and so we can safely choose a consistent 4 kpc radius aperture for our analysis.

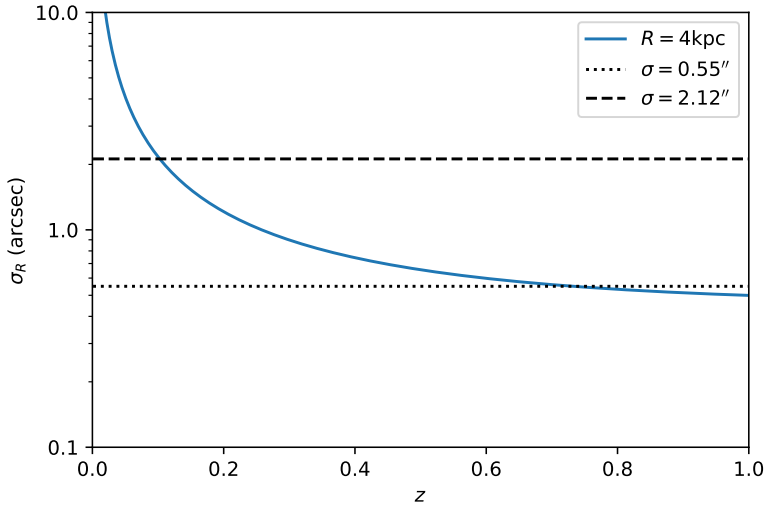

Figure 3.1: Apparent angular size as a function of redshift for a 4kpc aperture, plotted in solid blue. Lines of constant angular radius $\sigma = 0.55''$, characteristic of DES, and $\sigma = 2.12''$ are shown in dotted and dashed black, respectively.

3.3 DES Photometric Fits

Following the methodology detailed in Chapter 2, Bayesian fits were performed for both the global and local photometric data. Since we will only be fitting data from 4 filter bands, we will treat the stellar mass as a fixed parameter, referring to the values previously obtained for these galaxies by Kelsey (2020)[16]. The complete fit results for both the global and local cases are presented in Tables B.1 and B.2, respectively.

3.3.1 Global Photometry Fits

As we are mainly interested in the dust content of these galaxies, the first question we will tackle is whether or not there is evidence for a correlation between the two fitted dust attenuation law parameters, τ_V and n. Existing models for this relation in the literature tend to be mostly empirical[34]. In this work, we elect to perform a non-parametric regression, namely a Gaussian Process Regression. To do this, we resort to the **GauPro**[2][42] R package.

The details of the Gaussian Process Regression are discussed in Appendix D. In summary, it is a regression method built on Gaussian processes, which are stochastic processes that assume that a given data set follows a multivariate normal distribution[43]. Given the tests performed in Section 2.3, we consider this a reasonable assumption to make. Moreover, this method is particularly useful because it also allows for an estimate of the standard error.

[2] https://github.com/CollinErickson/GauPro

Fig. 3.2 shows the *best-fit* values for τ_V and n, as well as the result of the Gaussian Process Regression, including a 68% credible interval. For comparison, the mean relation obtained by Chevallard (2013)[34] for the overall correlation between these two quantities for a set of simulated galaxies observed at different angles is also plotted in Fig. 3.2. This relation takes the form[34]:

$$n \simeq \frac{2.8}{1 + 3\sqrt{\tau_V}} \qquad (\pm 25\%) \tag{3.4}$$

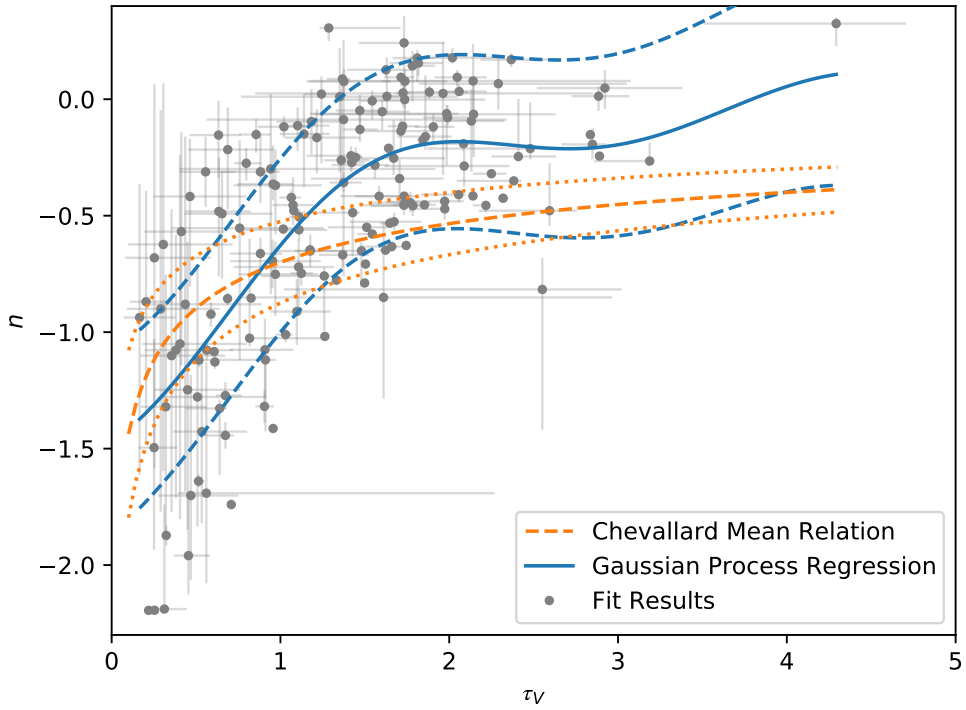

Figure 3.2: *Best-fit* values of n as a function of τ_V for the fitted DES galaxies with DECam global *griz* photometry. Results for the different galaxies are shown in grey. A Gaussian Process Regression is shown in solid blue, with dashed blue lines defining a 68% credible interval. The mean relation found for similar galaxies by Chevallard (2013)[34] is shown in dashed orange, with $\pm 25\%$ error margins shown in dotted orange.

Despite some scatter, there is a clear correlation between the two quantities, with a larger optical depth corresponding to a larger value of n, and thus a shallower attenuation curve. It should be noted, however, that the fitted curve is not representative of the data for $\tau_V > 3$, as there are few data points in this region.

Although the Chevallard model simulation relation given by Eq. 3.4 differs slightly from our data we can see that it expresses the same overall tendency. We are thus fairly confident that the overall correlation between the two fitted dust parameters can be explained by different galaxy orientations, such as schematically represented in Fig. 3.3[34]. The cases with small τ_V, mostly correspond to galaxies that are being observed face-on. To understand the important phenomena governing observations in

this case, we must consider both the photons emitted parallel and perpendicularly to the galaxy plane.

Photons emitted perpendicularly to the galaxy plane, that is, along the line of sight for a face-on galaxy, suffer minimal attenuation, independently of their wavelength. Looking only at this component one would therefore expect low values of reddening. However, we must also take into account photons emitted along the equatorial plane of a galaxy, which might be scattered away from the plane and into the line of sight. On one hand, for blue photons, which interact strongly with the dust particles, the probability of escaping the plane in this manner is low, as they are likely to continue interacting with the dust particles even after being scattered, eventually being fully absorbed[34]. On the other hand, red photons, which do not interact as strongly with dust particles, have a higher change of not meaningfully interacting with dust after this scatter event, which allows them to more consistently escape the galaxy plane in this fashion. This leads to higher values of reddening and, consequently, a higher attenuation curve slope, reflected in more negative values for n.

The cases with a larger τ_V correspond roughly to a edge-on view of the galaxies. In these cases, radiation emitted from the deepest layers of the galaxy starts to be fully absorbed, independently of wavelength. For this reason, the radiation reaching an observer is dominated by stars located in the outermost layers of the galaxy, unobscured stars and light scattered into the line of sight[44]. This leads to an overall lower level of reddening and values of n closer to 0.

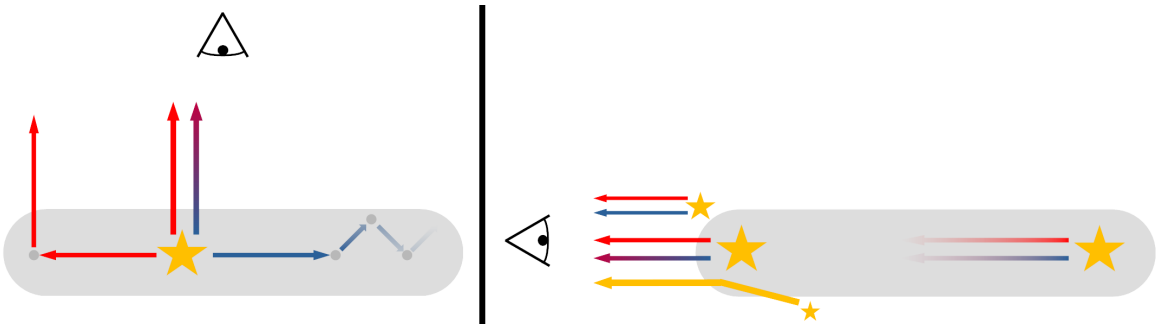

Figure 3.3: Schematic representation of dust attenuation for different galaxy orientations, namely head-on (Left panel) and edge-on (Right panel) observations.

It should be noted that galaxy orientation is not the only mechanism behind the correlation observed in Fig. 3.2, being mostly relevant for spiral galaxies. For elliptical galaxies, for example, galaxy orientation is not an important factor. However, due to the overall low dust content for these particular galaxies, they end up exhibiting a behaviour similar to the one observed for head-on spiral galaxies, leading to an overall large level of reddening.

Additionally, different galaxies can have different intrinsic optical depths, which is one of the possible reasons for the scatter observed in the figure.

The discrepancy observed between the Chevallard model simulations and our fit results can be possibly explained by the fact the former as been derived for dust attenuation in the galactic disc. Simulations for the attenuation in the central galactic bulge result in values of n that grow much more rapidly with τ_V[34], which is precisely what we see in our results. As our global data comes from a Kron aperture photometry, it is likely that the measurements do include light from the central bulge. However, it

has been shown that bulge stars typically account for only a small portion of the total optical emission, with the overall dust attenuation being controlled by the disk component[34], which suggests a different cause for the discrepancy observed in Fig. 3.2.

Regarding the contribution of unobscured stars in the cases with higher τ_V, it should be said that if the unobscured population is composed of older stars, then an increase in τ_V might produce the opposite effect, steepening the attenuation curve. We must then take a closer look at the relation between t_{age} and τ_V, plotted in Fig. 3.4. The results from this plot help validate the previous hypothesis, as it is clear that galaxies with larger τ_V values also tend to be younger. We can then be fairly confident that the flatness of the attenuation curves in the region of $\tau_V \sim 2$ is a product of young unobscured stars.

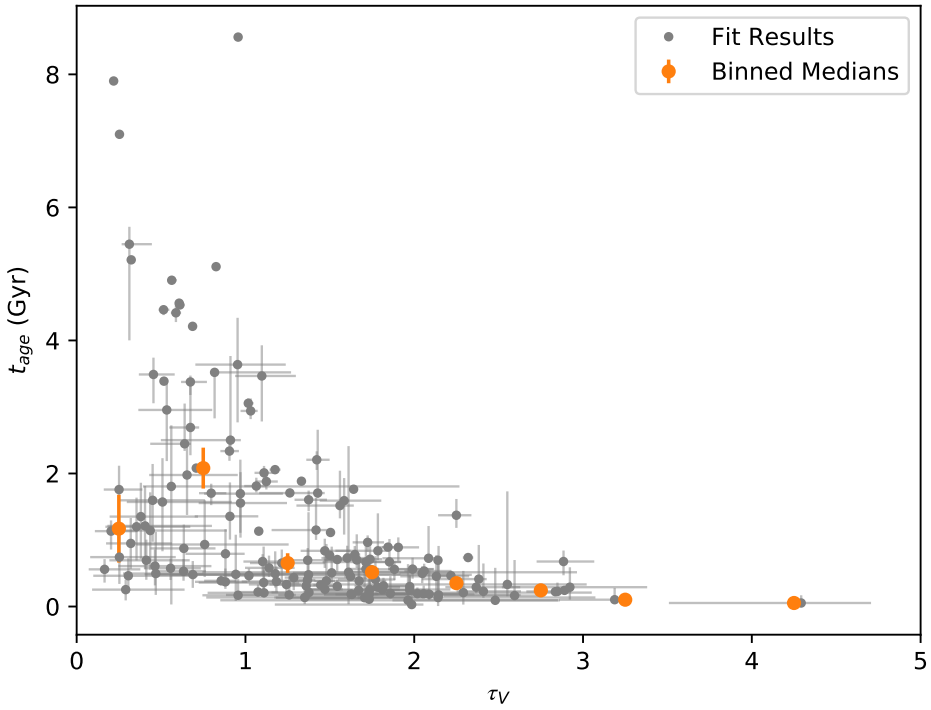

Figure 3.4: *Best-fit* results of t_{age} as a function of τ_V for the fitted DES galaxies with DECam global *griz* photometry. Results for the different galaxies are shown in grey. Binned medians for each parameter are shown in orange.

Another relevant question is the way the fit parameters relate to the stellar mass, particularly the dust parameters. In this case, we are not only interested in τ_V and n, but also in the quantity $E(B-V)$, which is a function of these last two parameters and can be obtained from Eqs. 1.11 and 2.11. The *best-fit* dust parameters for each galaxy as a function of stellar mass are plotted in Fig. 3.5. The stellar age t_{age} is also plotted, as it can also provide some insights into dust behaviour, as we shall see.

Starting with τ_V, we can see that, despite some scatter, this quantity increases steadily with $\text{Log}(M_\star/M_\odot)$, up to $\text{Log}(M_\star/M_\odot) \simeq 10$. This tendency is in agreement with results obtained for star-forming galaxies by Salim (2018)[14]. This data, however, describe a continuous increase in τ_V even after the $\text{Log}(M_\star/M_\odot) \simeq 10$ limit, which does not match our results. The large scatter observed for higher stellar

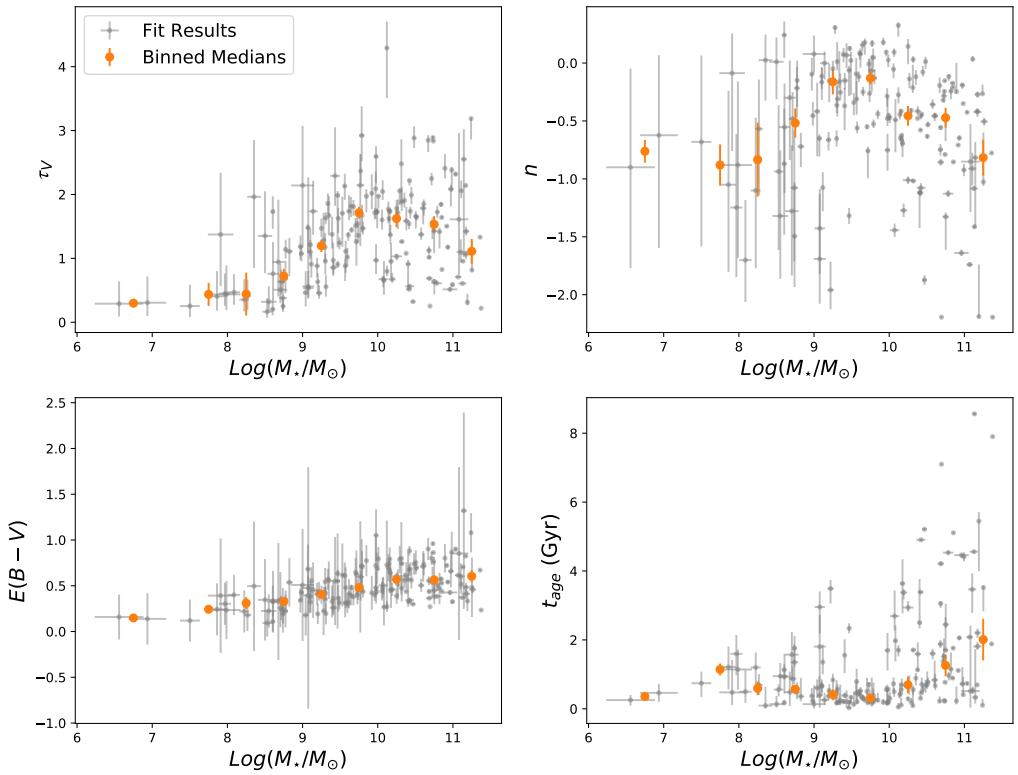

Figure 3.5: *Best-fit* results for different quantities as a function of $\mathrm{Log}(M_\star/M_\odot)$ for the fitted DES galaxies with DECam global *griz* photometry. From top to bottom and left to right we have: τ_V, n, $E(B-V)$ and t_{age}. Results for the different galaxies are shown in grey. Binned medians for each parameter are shown in orange.

masses points to the fact that our data set includes not only star-forming galaxies, but also quiescent galaxies, which typically have lower optical depths and, consequently, attenuation curves with steeper slopes[14].

One way of determining which of the galaxies are quiescent is to look at their respective ages, as quiescent galaxies tend to be older. From the lower right corner of Fig. 3.5, we can see than indeed galaxies with $\mathrm{Log}(M_\star/M_\odot) > 10$ tend to be older, which supports the theory that the more negative values of n in this region are related to quiescent galaxies. Unfortunately, due to the limited photometric data, this hypothesis cannot be fully validated.

Looking now at n, it is clear that this quantity exhibits a behaviour very similar to that of the optical depth which, given the strong correlation shown between the two quantities, is not very surprising. As mentioned before, quiescent galaxies tend to have steeper attenuation curves slopes, which is probably the reason for the comparatively more negative values of n found for higher masses.

Looking at the results for $E(B-V)$, we can see that it exhibits a tenuous but noticeable increase with $\mathrm{Log}(M_\star/M_\odot)$, which contrasts the behaviour observed for both τ_V and n. However, it should be noted that it is difficult to make concrete assertions about the behaviour of this quantity, as it shows only a

slight variation coupled with relatively high error margins.

Finally, it should be noted that, as previously discussed, observation orientation is one of the main mechanisms governing a galaxy's attenuation law. This is one possible explanation for the large scatter observed in Fig. 3.5. This is one of the reasons why it is important to look at the median values in each mass bin, namely to get a fair representation of the real physical tendencies as seen across different galaxy orientations.

3.3.2 Local Photometry Fits

As in the case of global photometry, we start by looking at the correlation between the two dust parameters, τ_V and n. Once more, a Gaussian Process Regression was performed, the results of which are displayed in Fig. 3.2 as well as the corresponding 68% credible interval. The *best-fit* values for τ_V and n for the individual galaxies, as well as the mean relation obtained by Chevallard (2013)[34], are also shown.

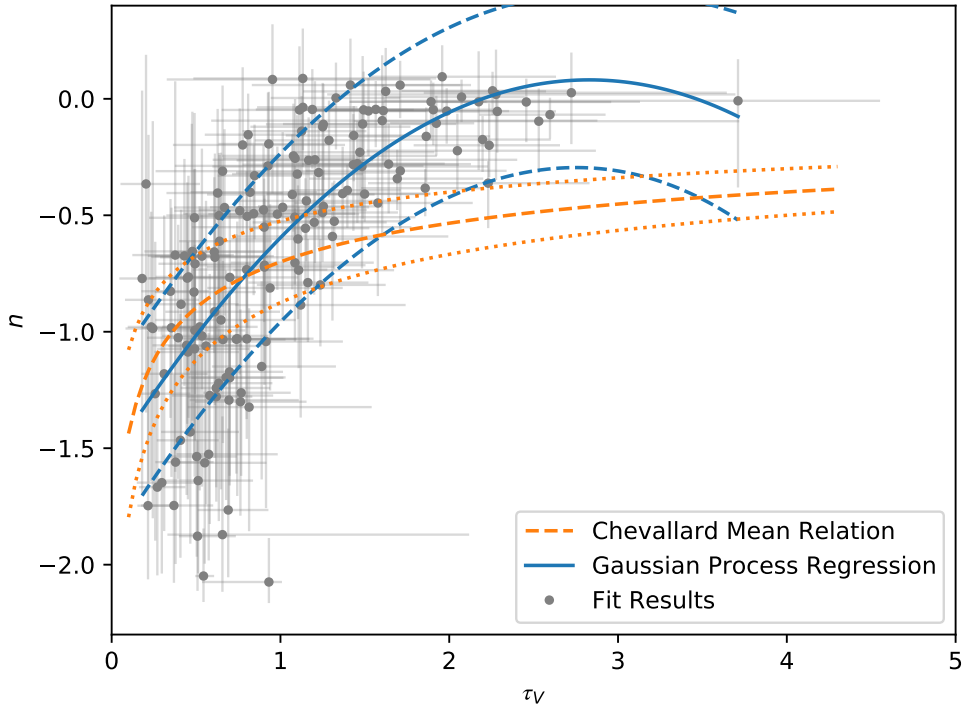

Figure 3.6: *Best-fit* values of n as a function of τ_V for the fitted DES galaxies with DECam local *griz* photometry. Results for the different galaxies are shown in grey. A Gaussian Process Regression is shown in solid blue, with dashed blue lines defining a 68% credible interval. The mean relation found for similar galaxies by Chevallard (2013)[34] is shown in dashed orange, with $\pm 25\%$ error margins shown in dotted orange.

Once again the correlation between the two quantities is clearly apparent, with the local results echoing the relation found for global photometry. It must also be noted that the fitted curve is not representative of the data for $\tau_V < 2.5$.

One difference between both fits is the agreement with the Chevallard mean relation. In the case of local photometry, this agreement is visibly poorer, as the fitted attenuation curves end up being shallower than predicted. The argument that this is due to contributions from the galactic bulge does not seem appropriate in this case, as we are considering only a 4kpc aperture around each SN Ia location, which might not include the bulge region.

Apart from this, an hypothesis for the underlying mechanisms governing this relation has already been discussed. For the sake of consistency, we will once again plot the relation between τ_V and t_{age}, so as to decide on the plausibility of young unobscured stars producing flattened attenuation curves for higher optical depths. These results are plotted in Fig. 3.7 and are consistent with those recovered for the global case.

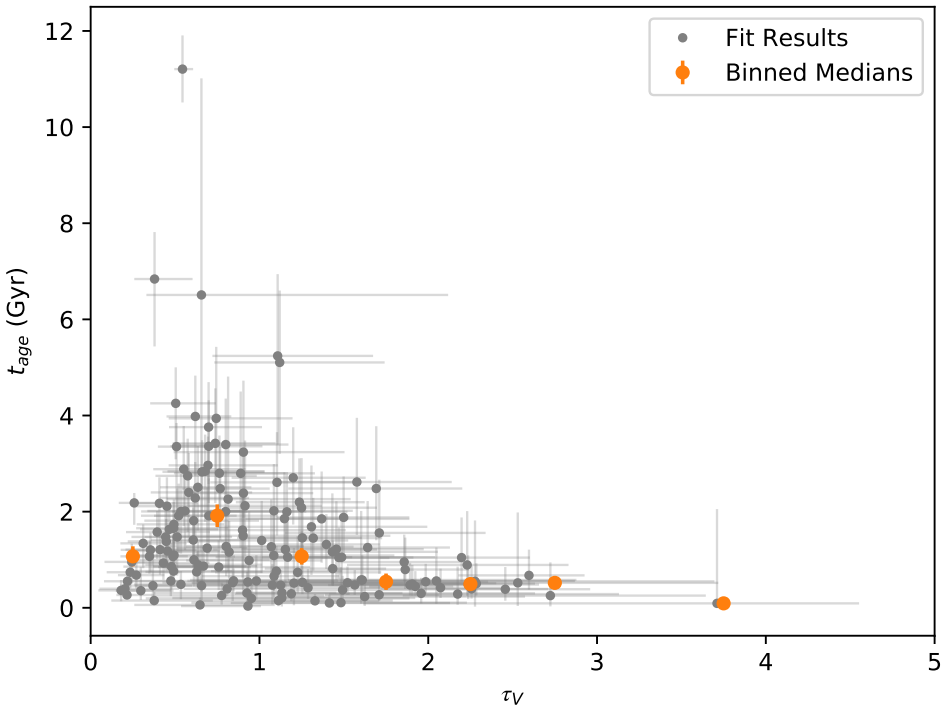

Figure 3.7: *Best-fit* results of t_{age} as a function of τ_V for the fitted DES galaxies with DECam local *griz* photometry. Results for the different galaxies are shown in grey. Binned medians for each parameter are shown in orange.

Next, we will tackle the relation between the fit parameters and the stellar mass. For each galaxy, the *best-fit* parameters for τ_V, n and t_{age} as well as $E(B-V)$ are plotted in Fig. 3.8 as a function of stellar mass.

All the quantities reflect the same general tendencies observed in Fig. 3.5 for the global photometry case, although with a larger degree of scatter. In particular, it is hard to make a concrete assertion about the behaviour of n, as the scatter and error margins are simply too large. Even so, the binned medians seem to confirm the previous result.

We can thus conclude that the two sets of photometry give rise to similar results, which are also

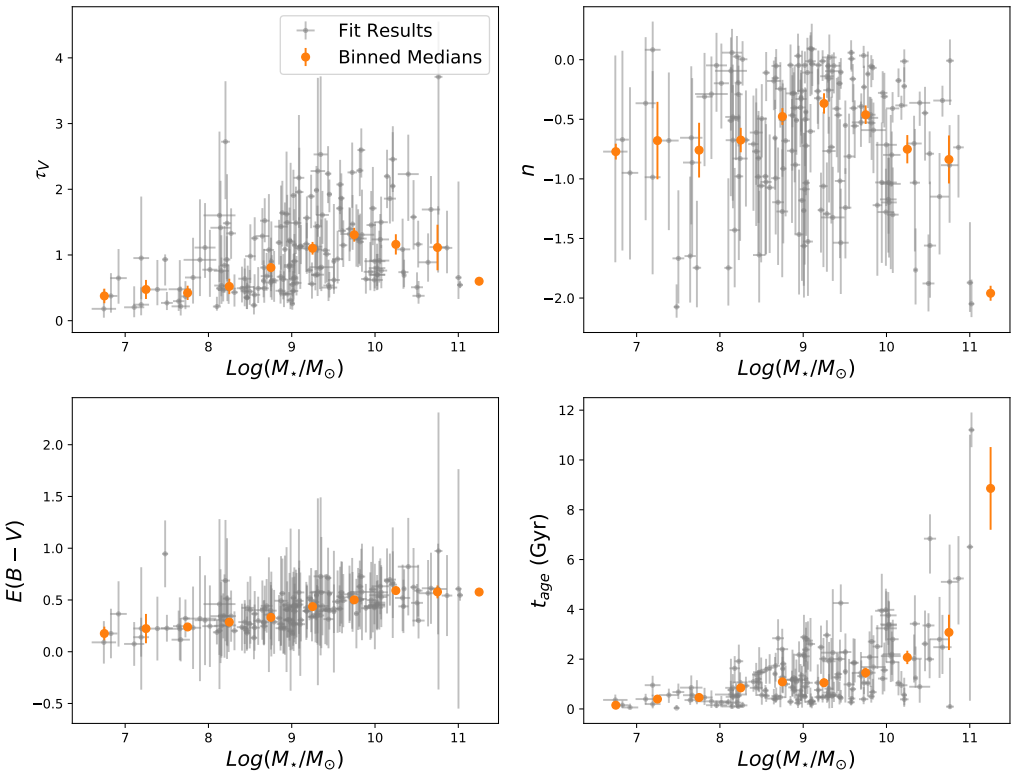

Figure 3.8: *Best-fit* results for different quantities as a function of $\mathrm{Log}(M_\star/M_\odot)$ for the fitted DES galaxies with DECam local *griz* photometry. From top to bottom and left to right we have: τ_V, n, $E(B-V)$ and t_{age}. Results for the different galaxies are shown in grey. Binned medians for each parameter are shown in orange.

in agreement with literature predictions and observations, at least on a general level. We offer a more detailed comparison between the global and local measurments in the next section.

3.3.3 Comparison Between Global and Local Results

We will now look at a deeper comparison between the fit results for both global and local photometry. Particularly, we will look at whether the distance to an observed galaxy, that is, the redshift, has any impact on the dust parameters τ_V and n obtained from global and local photometric fits. To this effect, in Fig. 3.9 are plotted the deviations $\Delta\tau_V = \tau_{V_{\mathrm{Global}}} - \tau_{V_{\mathrm{Local}}}$ and $\Delta n = n_{\mathrm{Global}} - n_{\mathrm{Local}}$, as a function of the redshift z.

Despite some level of scattering, the results for both fits are fairly consistent, with median deviations $\Delta\tau_V = 0.26$ and $\Delta n = 0.026$. Even so, there seems to be a level of bias present in the fits, as the results obtained for τ_V tend to be larger for the global photometry fit.

There are a few galaxies for which the consistency is not as good, but, for most of them, the *best-fit* values are still within each other's error bars. Additionally, we can see that the results remain constant as the redshift increases, which is ideal.

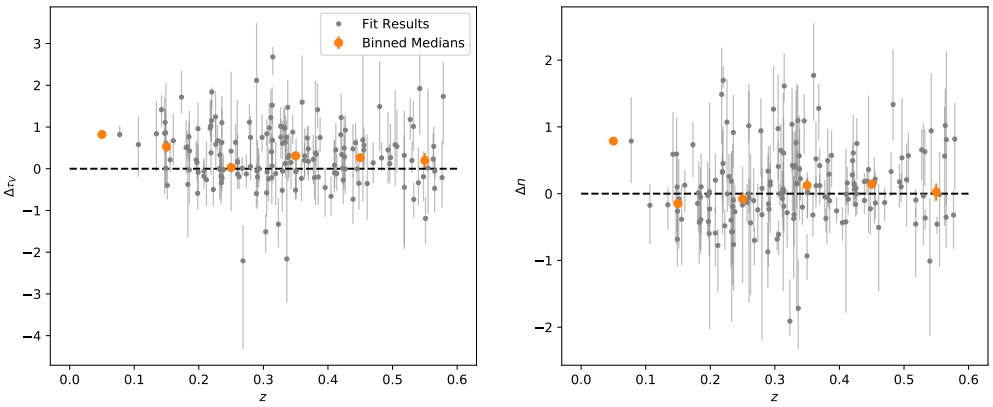

Figure 3.9: Differences between *best-fit* results for the parameters obtained with global and local DECam *griz* photometry for the DES galaxies, as a function of z. The left hand side shows the results for τ_V and the right hand side the ones for n. Results for the different galaxies are shown in grey. Binned medians for each parameter are shown in orange.

3.4 Additional GALEX and 2MASS Photometry

In Section 2.3 we discussed the benefits of including extra photometry in the SSP fits. We concluded that, although broadband optical photometry is mostly sufficient to accurately recover dust attenuation laws, the inclusion of UV photometry, whether by itself or in conjunction with NIR data, marginally improves the fit results. In this section we will look at the impacts of this additional photometry in the previously discussed DES data set. The full fit results for the global case are presented in Table B.3.

3.4.1 Additional Global Photometry

In the case of additional global photometry, we will look for complementary Kron FLUX_AUTO UV and NIR measurements in the GALEX and 2MASS catalogs. This approach is not perfect, as the lack of a consistent detecting image between different surveys does not guarantee a constant aperture across different filter bands. However, and due to the way the Kron algorithm is constructed, it is acceptable to first approximation.

We were able to secure complementary data for 33 of the SNe Ia host galaxies. Additionally, there were some galaxies for which only 2MASS data was available, but this data was not considered, as we have shown in Section 2.3 that the inclusion of NIR photometry tends to produce worse fits when not properly balanced with the corresponding UV data. The detailed list of photometric data obtained is as follows:

- 4 galaxies with GALEX *NUV*/*FUV* and 2MASS *JHKs*;
- 1 galaxy with GALEX *NUV*/*FUV* and 2MASS *JH*;
- 1 galaxy with GALEX *NUV* and 2MASS *JH*;
- 9 galaxies with GALEX *NUV*/*FUV*;

- 18 galaxies with GALEX *NUV*

This number of galaxies is not sufficient to make any meaningful observations about the correlation between the dust parameters. For this reason, we will focus on comparing the new dust fit parameters with those previously obtained in Section 3.3.1. In Fig. 3.10 we plot the differences between the *best-fit*$_{griz}$ and the *best-fit*$_{griz+GALEX+2MASS}$ values for the dust parameters. The corresponding values of RMS for these differences is also plotted.

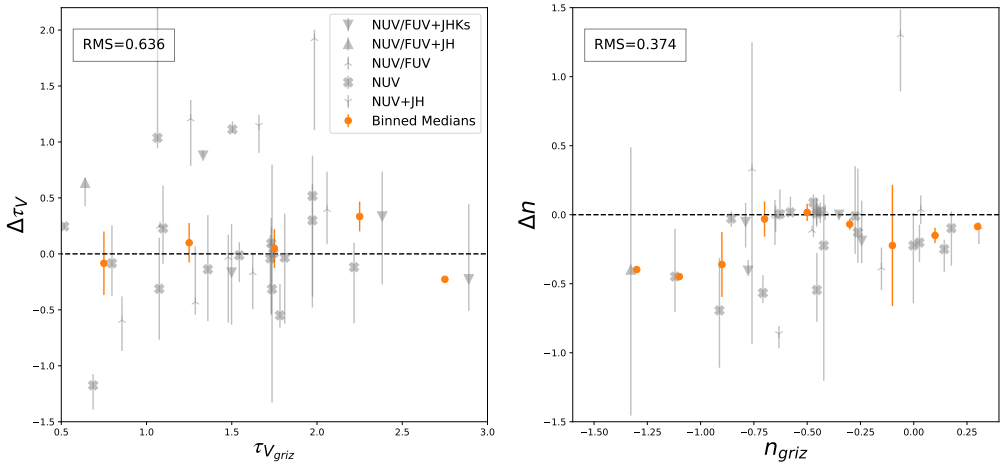

Figure 3.10: Differences between *best-fit* values for DECam *griz* photometry fits and GALEX *NUV*/*FUV*, 2MASS *JHKs*, and DECam *griz* photometry fits for the DES galaxies as a function of the *best-fit*$_{griz}$ parameters. The left panel shows the results for τ_V, while the right panel shows the values for n. Results for the different galaxies are shown in grey. Binned medians for each parameter are shown in orange. The corresponding values of RMS for each parameter are also plotted in the top left corner.

The results are very similar to those obtained from simulations in Section 2.3, with both sets of photometry yielding comparable results. There is some scatter present, but on the whole the results are fairly close, with overall median deviations of $\Delta\tau_v = 0.0065$ and $\Delta n = -0.086$. Additionally, we obtain $RMS_{\tau_v} = 0.636$ and $RMS_n = 0.374$. We again conclude that, at least for the global case, additional photometry has a mostly negligible impact on the fit results, which do not differ significantly from those obtained using only DECam *griz* photometry.

3.4.2 Additional Local Photometry

In the case of local Photometry, we used a pipeline Python code[3] to query and reduce GALEX data, returning 4kpc local aperture photometry. There are, however, a few considerations to take into account.

In particular, the GALEX survey has a PSF FWHM$\sim 5''$[4][17], which, according to Eq. 3.1, leads to a smallest useful aperture radius of $\sigma = 2.12''$. Therefore, from Eq. 3.2, we find that for a physical aperture of 4kpc, we can only resolve objects with $z < 0.1$, as shown in Fig. 3.1. Additionally, to assure

[3] https://github.com/perseu/pipeline
[4] https://asd.gsfc.nasa.gov/archive/galex/Documents/instrument_summary.html

the objects are indeed observable, we only consider galaxies for which Kron aperture photometry was also available.

Following this procedure, we were only able to recover UV data for 1 galaxy. Given that this is not sufficient for any type of analysis and that NIR data always needs to be balanced by corresponding UV data, we will move on.

Chapter 4

SNe Ia Cosmology

As we have seen from the overall results discussed in Chapter 3, the fitting methodology discussed in this work is quite successful at obtaining dust attenuation laws for SNe Ia host galaxies. We will now tackle the question of whether these recovered attenuation laws can offer an accurate description of the respective SNe Ia extinction laws.

4.1 Dust Extinction for DES SNe Ia

As we discussed in Section 1.2, the phenomena governing dust extinction differ slightly from those governing attenuation. In particular, the geometrical effects related to the spacial distribution of dust and light sources cease to be relevant, and only the amount and type of dust located on the line of sight is important.

To examine the way dust effects differ between point sources (SNe Ia) and extended objects (host galaxies), we plot in Fig. 4.1 the *best-fit* values for R_V and τ_V for the DES host galaxies. The values of R_V can be easily obtained from Eqs. 1.12 and 2.11. As a term of comparison, we look at the correlation found by Mandel (2011)[45] between R_V and A_V for a set of SNe Ia extinction, which can be expressed as:

$$R_V \simeq \frac{1}{a + bA_V} \tag{4.1}$$

with $a = 0.35 \pm 0.05$ and $b = 0.15 \pm 0.03$[45]. This relation is also plotted in Fig. 4.1, with Eq. 1.9 being used to relate A_V and τ_V.

Despite the large error margins for each of the individual fit points, it is clear that the extinction laws for SN Ia and the dust attenuation laws for host galaxies exhibit two opposite tendencies. This is to be expected based on the processes involved in both cases.

The rationale for the correlation found for the parameters in the galaxy attenuation laws has already been discussed in detail in Section 3.3. In summary, it is a combination of both star to dust geometry and galaxy observation orientation.

In the case of galaxies, the high levels of reddening, and consequently low R_V, observed for low

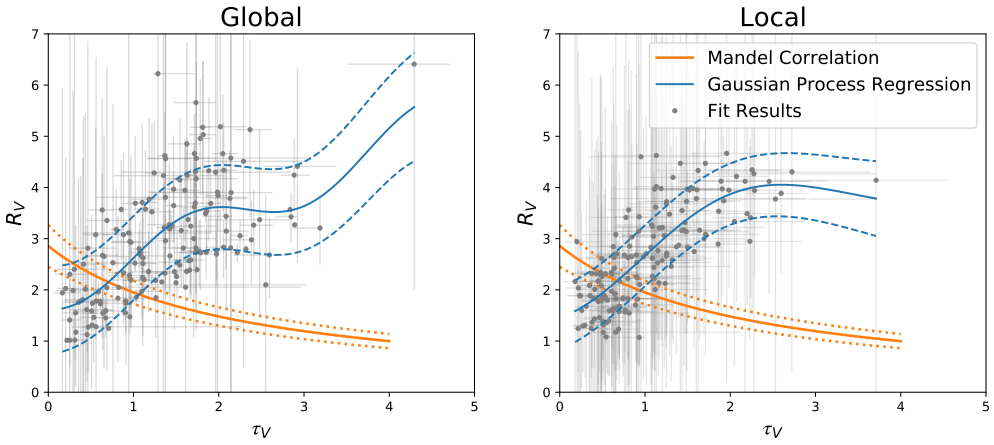

Figure 4.1: *Best-fit* values of R_V as a function of τ_V for the fitted DES galaxies with DECam Global (Left panel) and Local (Right panel) *griz* photometry. Results for the different galaxies are shown in grey. A Gaussian Process Regression is shown in solid blue, with dashed blue lines defining a 68% credible interval. The correlation found by Mandel (2011)[45] between these two quantities for the extinction laws of a set of SN Ia is shown in orange.

optical depths can be understood as primarily an effect of the scattering into the line of sight of (mostly red) radiation originally emitted along the equatorial plane of the galaxy. When dealing with a point source, however, this effect is not relevant, and thus we end up with lower values of reddening, an thus higher R_V, for lower optical depths. This happens because photons don't have that many opportunities to interact with dust grains, meaning we end up with fairly uniform extinction for different wavelengths.

As the optical depth increases these interaction opportunities increase, and thus we see a decrease of R_V with τ_V, as the level of reddening grows. Once again, the factors governing galaxy dust attenuation in this regime are no longer relevant. To start off, we can be sure that the SN Ia has not been totally obscured by a dust cloud, as this would make its observation impossible, at least in the optical filter bands. For this reason, there are no other possible unobscured sources for the radiation we are seeing, and thus the reddening is indeed a true reflection of the amount and composition of dust between the SN and the observer.

It is also worth noting that the results obtained are consistent between global and local observations, which indicates that an aperture of 4kpc is not sufficiently small to negate the geometrical effects associated with attenuation, meaning one needs even smaller physical apertures to correctly account for dust extinction.

The discrepancy between SN Ia and galaxies can also be observed, although not as clearly, from a plot of R_V as a function of $E(B-V)$, as shown if Fig. 4.2. In addition to the data and the Mandel correlation, the binned priors obtained by Burns (2014)[46] are also displayed.

In this case, the standard deviations for the binned medians are quite large, which complicates a definite analysis. However, the data points for galaxy attenuation seem to indeed follow a different tendency from the one expected for point source attenuation.

These results point to the fact that there is not an exact one-to-one relation between a SN Ia dust extinction and its host galaxy's attenuation, which might introduce problems should the latter be used to

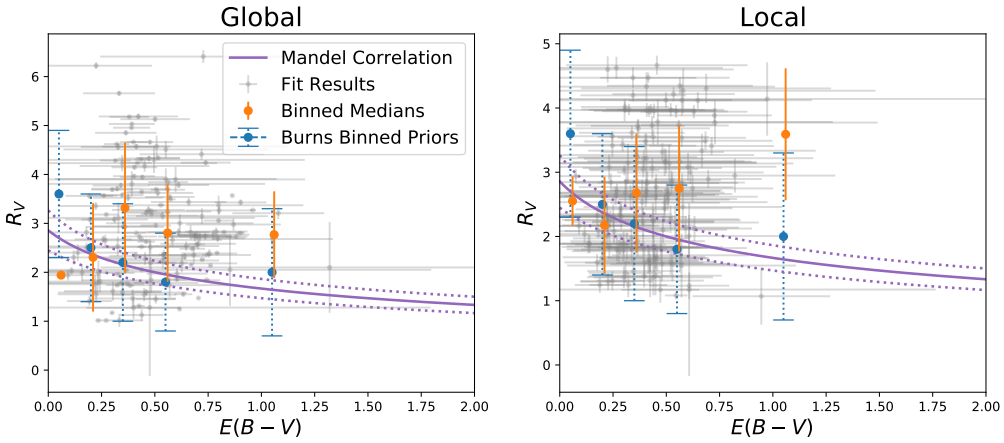

Figure 4.2: *Best-fit* values of R_V as a function of $E(B-V)$ for the fitted DES galaxies with DECam Global (Left panel) and Local (Right panel) *griz* photometry. Results for the different galaxies are shown in grey. Binned medians for R_V are shown in orange. The binned priors obtained by Burns (2014)[46] from an analysis of SN Ia extinction laws are shown in orange. The correlation found by Mandel (2011)[45] between these two quantities for the extinction laws of a set of SN Ia is shown in purple.

extrapolate new β values for SNe Ia calibration. We will explore this further in a later section.

It should be noted, however, that in many occasions, host galaxy data is indeed the best way available to probe the dust content for SNe Ia. In the next section, we will thus explore the relations found between the DES host galaxies' attenuation laws and their respective SN light-curve parameters.

4.2 Light Curve Fits and Dust Attenuation

In this section we will focus on examining the possible relations between a host galaxy's dust attenuation parameters and its respective SN Ia light-curve fit parameters x_1, c and m_B, originally obtained by the DES collaboration[9]. The relations between these parameters with the values of τ_V, n and $E(B-V)$ for both the global and local cases are plotted in Figs. 4.3, 4.4 and 4.5, respectively.

Focusing first of the $x_1 - \tau_V$ and $x_1 - n$ plots, we see that they mostly resemble statistical scatter, with results consistent for both the global and local cases. There are a few variations, but these are mostly confined to regions with only a small number of data points available.

In the case of the $x_1 - E(B-V)$ plot we see that, although the level of scatter is still large, a correlation between the two quantities seems indeed to be present when looking at the binned median values. Indeed, larger values of $E(B-V)$ correspond, on average, to lower values of x_1. One possible explanation for this is that we are indirectly recovering a well documented relation between the SNe Ia light-curve stretch x_1 and its host galaxy stellar mass $M_\star$, which predicts that more massive hosts tend to produce SNe Ia with smaller values of x_1[47]. This fact, coupled with the correlation observed between $\mathrm{Log}(M_\star/M_\odot)$ and $E(B-V)$ in both Figs. 3.5 and 3.8, makes this indirect recovery the most likely option. To confirm the hypothesis, we plot the relation between x_1 and $\mathrm{Log}(M_\star/M_\odot)$ in Fig. 4.6.

In the case of the color parameter, which is more closely related to the effects of dust, we can see that

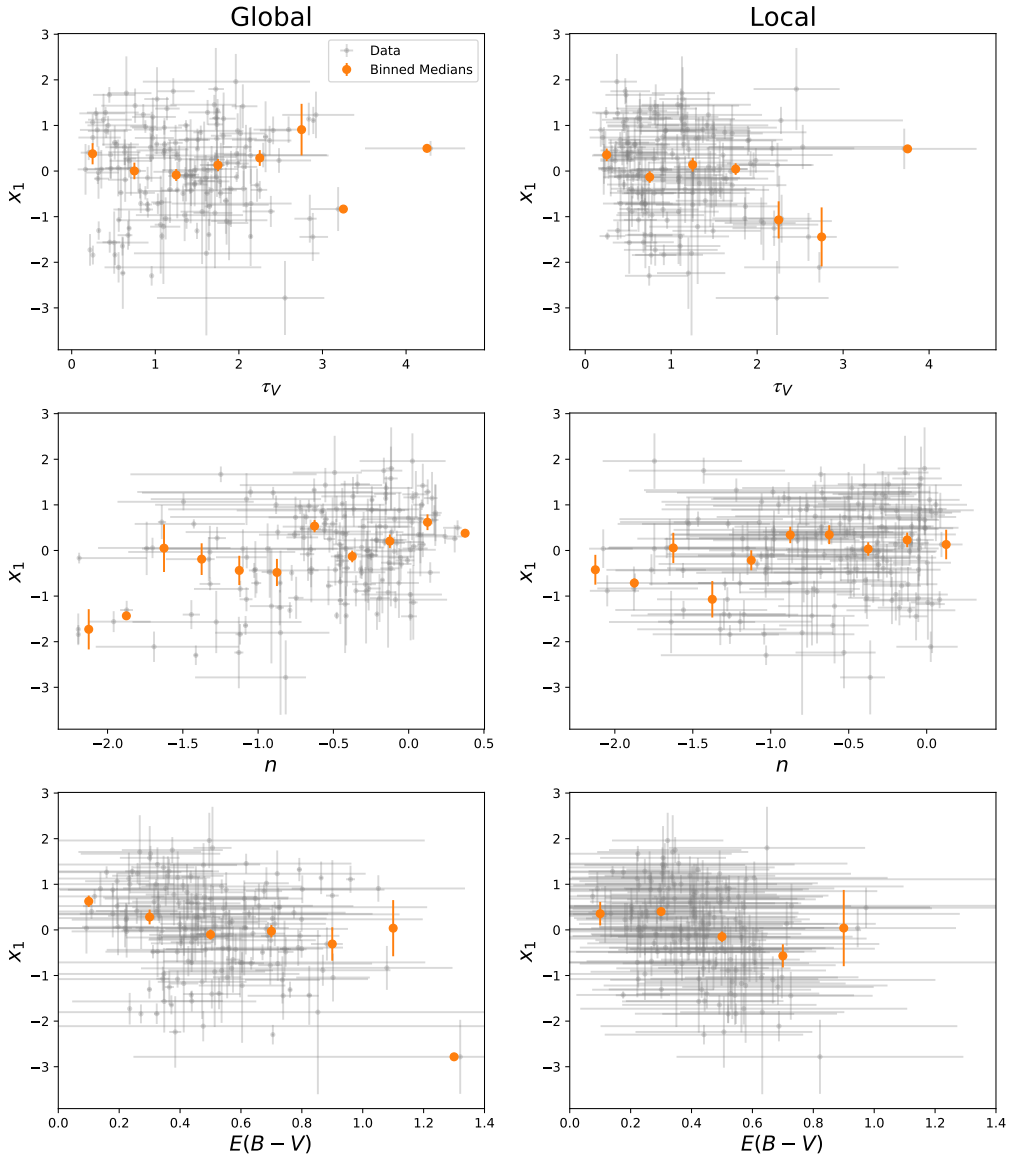

Figure 4.3: Light curve fit results for x_1 as a function of different *best-fit* parameters for the fitted DES galaxies with DECam both Global (Left panels) and Local (Right panels) *griz* photometry. From top to bottom, we have: $x1$ as a function of τ_V, n and $E(B-V)$. Results for the different galaxies are shown in grey. Binned medians for each parameter are shown in orange.

all the plots resemble a statistical scatter, with no noticeable relation between c and the dust parameters. This can be explained by two possible scenarios.

On one hand, it could be possible that intrinsic variations of color among different SNe Ia are simply a more prominent factor than dust reddening when considering the observed color of the SNe light-curves. On the other hand, as we have previously discussed, host galaxy attenuation is not completely adequate

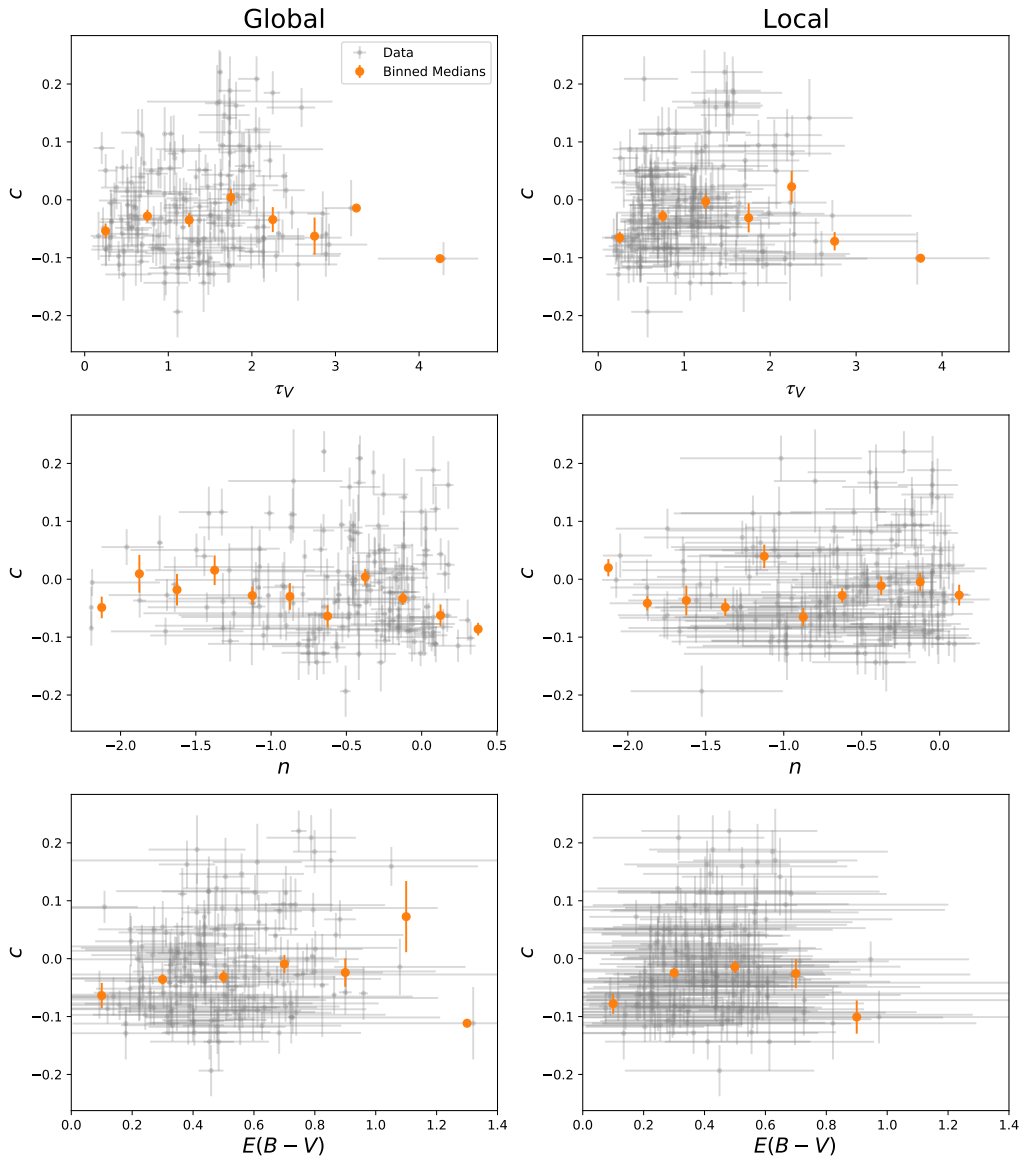

Figure 4.4: Light curve fit results for c as a function of different *best-fit* parameters for the fitted DES galaxies with DECam both Global (Left panels) and Local (Right panels) *griz* photometry. From top to bottom, we have: c as a function of τ_V, n and $E(B-V)$. Results for the different galaxies are shown in grey. Binned medians for each parameter are shown in orange.

at describing the local reddening of SNe Ia. In other words, a relation between a SNe Ia light-curve color and its host galaxy attenuation cannot be assumed, as evidenced by Fig. 4.4. Although we do not have enough data to conclude that intrinsic color variations do not play a significant role in the present results, the latter explanation is the most probable one, considering the circumstances.

Finally, looking at the $m_B - n$ and $m_B - E(B-V)$ plots, we once again find only statistical scatter with

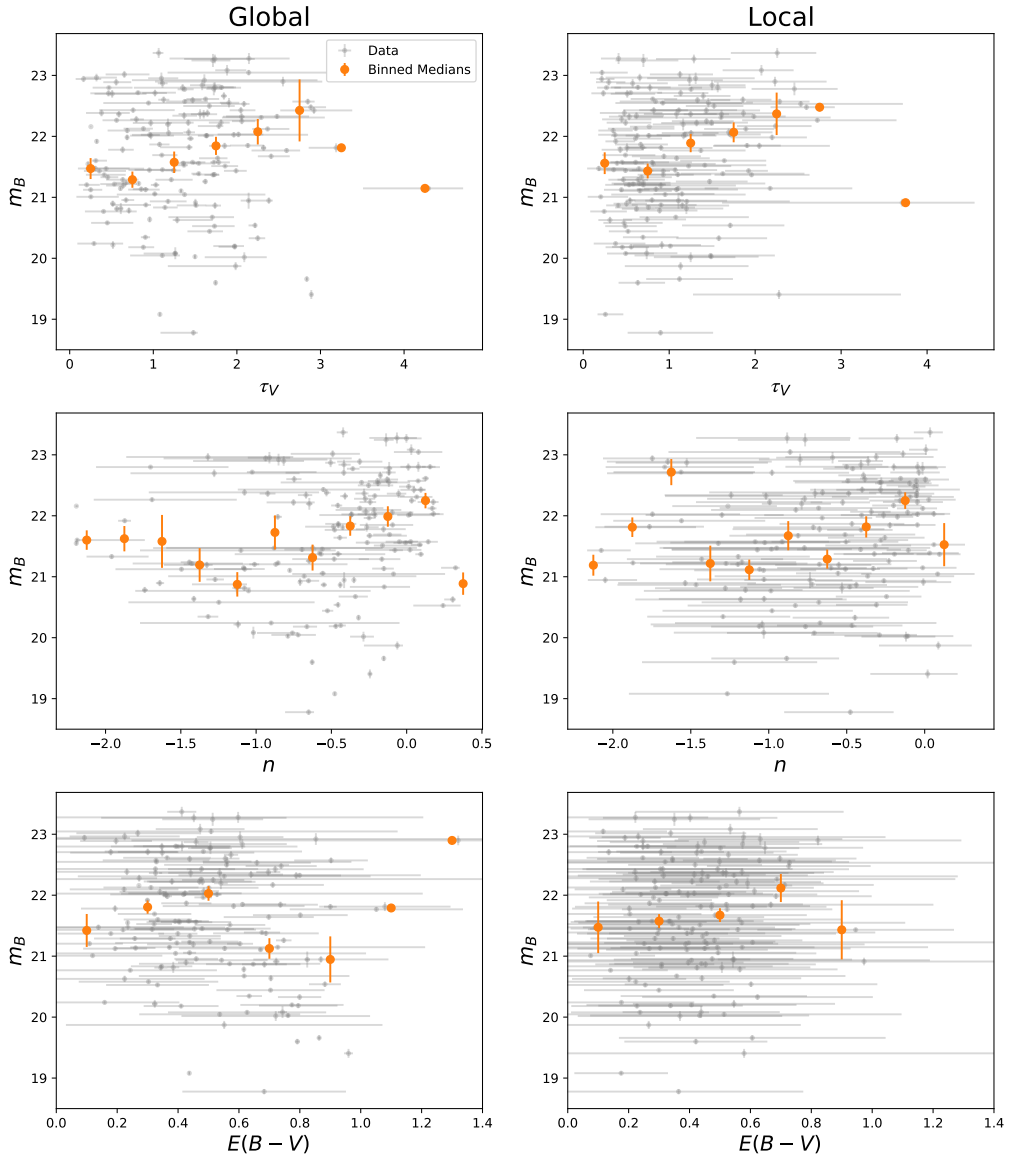

Figure 4.5: Light curve fit results for m_B as a function of different *best-fit* parameters for the fitted DES galaxies with DECam both Global (Left panels) and Local (Right panels) *griz* photometry. From top to bottom, we have: m_B as a function of τ_V, n and $E(B-V)$. Results for the different galaxies are shown in grey. Binned medians for each parameter are shown in orange.

no noticeable tendencies in the data. In the case of the $m_B - \tau_V$ plot, however, a correlation is readily apparent, with higher optical depths corresponding to higher magnitudes and thus fainter SNe.

Thinking back to the differences between SNe Ia extinction and host galaxy attenuation, it is clear that the main difference between the two is the level of reddening expected at each τ_V, which is controlled by the parameter n. As detailed in Section 3.3, the main mechanism behind a galaxy's optical depth is

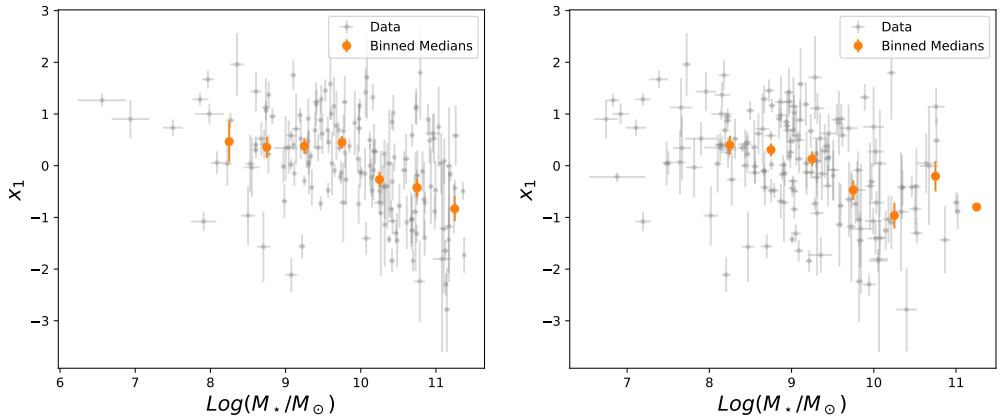

Figure 4.6: Light curve fit results for x_1 as a function of Log($M_\star/M_\odot$) for both the Global and Local cases. Results for the different galaxies are shown in grey. Binned medians for each parameter are shown in orange.

its orientation, with face-on observations leading to lower optical depths and vice-versa. Therefore, one should expect that the values for τ_V for both SNe Ia and their hosts should not differ significantly.

With this in mind, one possible origin for the correlation between m_B and τ_V displayed in Fig. 4.5 comes from the fact dust extinction causes not only a reddening of the observed spectrum, but also leads to a fainter observed image. Therefore, light traveling across higher optical depths results in higher apparent magnitudes. It is, however, difficult to conclude that this is indeed the main cause behind the observations, as one would first need to correct the values of m_B according to the respective redshift to make a more in depth analysis.

Overall, the use of a host galaxy's attenuation law to predict dust effects for the corresponding SNe Ia has some mixed results. On one hand, it appears to be an accurate tool at probing the overall extinction, that is, the dust optical depth, for the SNe Ia. On the other hand, it does not seem an optimal approach to determine reddening levels for the hosted SNe Ia, although the possibility that some of the discrepancies observed are the result of intrinsic color variations cannot be fully discarded. ´

4.3 Hubble Residuals "Steps"

In this section, we will focus on the SNe Ia calibration effects on the Hubble residuals, considering two main questions. First of all, we will examine whether there is evidence for a dust related "step" in the data and how it compares to the more commonly used "mass-step". Second of all, we will explore the effects of using both the global and local individual R_V values obtained for the host galaxies' in a new SNe Ia calibration. We are particularly interested in whether the "mass-step" observed for the Hubble residuals might in fact prove to be an artifact of the universal β calibration.

4.3.1 SNe Ia Calibrations

We will be working with two different sets of calibrations. The first calibration follows the standard Eq. 1.3, with an universal fitted β. In this particular case, we set $\delta_M = 0$ and $\delta_{\mu_{bias}} = 0$, so as to make the calibration specific contributions to the "mass-step" more apparent. For the second calibration, we take advantage of the values of R_V for the SNe host galaxies previously obtained in Section 3.3 to model SNe Ia extinction. Using Eq. 1.13, we can separate the extinction β_{R_V} and intrinsic β_{int} components in the β color-luminosity relation in Eq. 1.3. Thus, for this new calibration, we have[48]:

$$\beta c = \beta_{R_V} E(B-V) + \beta_{\text{int}}(c - E(B-V)) = A_B + \beta_{\text{int}}(c - E(B-V)), \tag{4.2}$$

where A_B is the attenuation for the B filter band, as evidenced by Eq. 1.12, and R_V and $E(B-V)$ are, in this case, the attenuation parameters obtained in Section 3.3, for both the global and local cases.

For both calibration fits, we once again use a Bayesian fitting procedure, with overall flat priors for the fit parameters and a likelihood function defined as:

$$\text{Ln}(\mathcal{L}) = -\frac{1}{2}\sum_{i=0}^{N}\frac{\Delta\mu_i^2}{s_i^2} \tag{4.3}$$

For the standard calibration, where we take α, β and M as free parameters, the value of s^2 is given by Eq. 4.4. For the R_V calibration, where the free parameters are α, β_{int} and M, s^2 is given by Eq. 4.5.

$$s^2 = \sigma_{m_B}^2 + (\alpha\sigma_{x1})^2 + (\beta\sigma_c)^2 + \sigma_{\text{int}}^2 \tag{4.4}$$

$$s^2 = \sigma_{m_B}^2 + (\alpha\sigma_{x1})^2 + \sigma_{A_B}^2 + \beta_{int}^2(\sigma_c^2 + \sigma_{E(B-V)}^2) + \sigma_{\text{int}}^2 \tag{4.5}$$

In the previous expressions, σ_{m_B}, σ_{x1} and σ_c are the uncertainties associated with each of the light-curve fit parameters, σ_{A_B} and $\sigma_{E(B-V)}$ are the uncertainties associated with the attenuation law parameters for the host galaxies and σ_{int} is a parameter which accounts for possible intrinsic variations in a SN Ia's luminosity. For the purposes of this analysis, we fix $\sigma_{\text{int}} = 0.107$, following the value obtained by González-Gaitán (2021)[13].

Finally, it should be noted that the analysis here detailed was repeated for some different likelihood functions. In particular, for some of these, σ_{int} was promoted to a free fit parameter. The results obtained for these alternative likelihoods were unchanged from those obtained using the likelihood defined by Eq. 4.3.

4.3.2 Hubble Residuals for the Standard Calibration

With both calibrations having been established, we will begin by examining the standard calibration. Following the procedure detailed in Section 4.3.1, the *best-fit* values found for the this calibration were $\alpha = 0.150^{+0.012}_{-0.010}$, $\beta = 3.157^{+0.011}_{-0.009}$ and $M = -19.372^{+0.010}_{-0.007}$. These values result in a fit $RMS = 0.137$.

The Mass Step

As mentioned in Section 1.1, the "mass-step" arises from a difference in luminosity between two SNe Ia populations, namely those originating in lower mass galaxies and those originating in higher mass galaxies. This essentially results in a difference between the mean values for the Hubble residuals for the two SNe Ia populations.

To look for a "mass-step", we begin by dividing the Hubble residuals into two populations, N_{low} and N_{high}, according to the stellar mass of the respective host galaxy. By varying the value at which the division is made, we can determine the optimal mass value for the step. This can be done by looking at several different quantities.

To begin with, we can look at the step magnitude found at each location, which is defined as the difference between the mean values of the Hubble residuals on each side of the step. This quantity is not very informative by itself, as we must take its error margin into account, which is done by looking at the step significance in σ. Finally, we can look at how much the introduction of the step benefits the overall description of the behaviour of the Hubble residuals. We do this by analysing the difference between the RMS_{mean} for a single population mean description and the RMS_{step} for a dual population mean description with a "mass-step". Thus, the larger the value of ΔRMS, the better a particular step locations is at reducing the Hubble residuals.

$$\Delta RMS = RMS_{\text{mean}} - RMS_{\text{step}} \tag{4.6}$$

$$RMS_{\text{mean}} = \sqrt{\frac{1}{N}\sum_{i=1}^{N}(\Delta\mu - \overline{\Delta\mu})^2} \tag{4.7}$$

$$RMS_{\text{step}} = \sqrt{\frac{1}{N}\left(\sum_{i=1}^{N_{\text{low}}}(\Delta\mu_{\text{low}} - \overline{\Delta\mu_{\text{low}}})^2 + \sum_{i=1}^{N_{\text{high}}}(\Delta\mu_{\text{high}} - \overline{\Delta\mu_{\text{high}}})^2\right)} \tag{4.8}$$

The results for the step magnitude, significance and ΔRMS found for the respective Hubble residuals are plotted in Fig. 4.7. In the case of global measurements, the optimal step location is found to be at $\text{Log}(M_\star/M_\odot) = 9.77$, with a maximum significance of 4.02σ, a step magnitude of 0.080 ± 0.020 mag and $\Delta RMS = 0.0060$. In the local case, the optimal step location is found to be at $\text{Log}(M_\star/M_\odot) = 9.405$, with a maximum significance of 5.35σ, a step magnitude of 0.115 ± 0.022 mag and $\Delta RMS = 0.0115$. We can see that, not only are both optimal steps significant at $> 4\sigma$, but they also correspond to the best improvement in RMS. Additionally, both step locations and their respective significance levels roughly match the results obtained by Kelsey (2020)[16] for this data set. This is very solid evidence for the existence of the "mass-step". To better illustrate it, the Hubble residuals are plotted in Fig. 4.8 as a function of $\text{Log}(M_\star/M_\odot)$. The optimal steps are also identified.

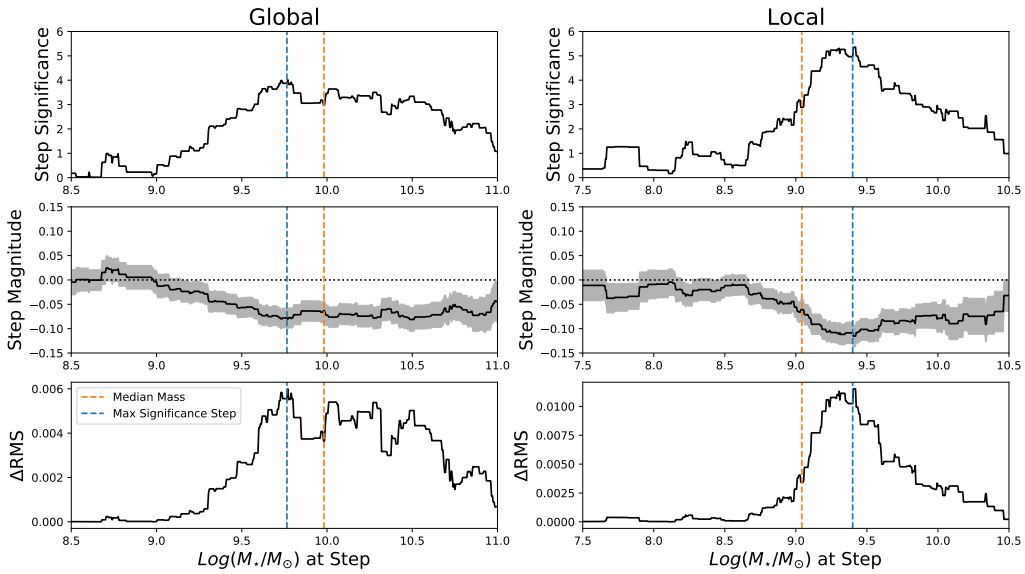

Figure 4.7: Evolution of the "mass-step" significance, magnitude and ΔRMS using SNe Ia standard β calibration for the global (Left panels) and local (Right panels) cases. In each case, and for each step location, the top panel shows the significance of the step in σ, the middle panel shows the magnitude of the step in solid black, with the grey region showing the uncertainty, and the lower panel shows the difference between RMS_{mean} and RMS_{step}. In these three panels, the location of the step of maximum significance is shown in blue and the median mass of the sample is shown in orange. Based on Kelsey (2020)[16].

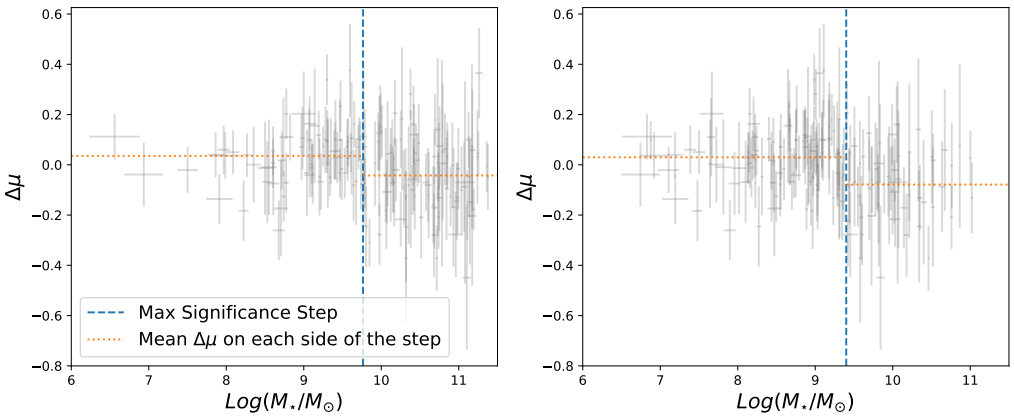

Figure 4.8: Hubble residuals for the DES SNe Ia as a function of the Global (Left panel) and Local (Right panel) Stellar Masses of the respective host galaxies for the universal β calibration. Results for the different SN are shown in gray. The location of the step of maximum significance is shown in blue, the mean values of $\Delta\mu$ on each side of the step are shown in purple and the median mass of the sample is shown in orange.

The Dust Steps

Now that the presence of the "mass-step" has been established, we will next look at whether evidence for a step related to the dust content of a SN host can be found in the data. In particular, we will examine

a possible "τ_V-step", related to τ_V, and an "n-step", related to n. We follow the same procedure as detailed above for the "mass-step", with the relevant plots for the two possible steps plotted in Figs. 4.9 and 4.10, respectively.

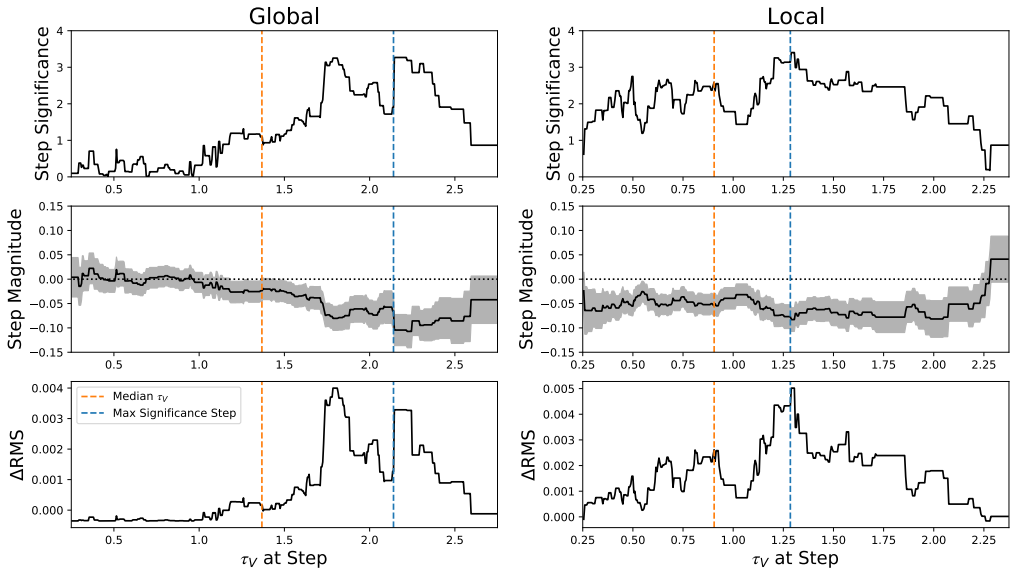

Figure 4.9: Evolution of the "τ_V-step" significance, magnitude and ΔRMS using SNe Ia standard β calibration for the global (Left panels) and local (Right panels) cases. In each case, and for each step location, the top panel shows the significance of the step in σ, the middle panel shows the magnitude of the step in solid black, with the grey region showing the uncertainty, and the lower panel shows the difference between RMS_{mean} and RMS_{step}. In these three panels, the location of the step of maximum significance is shown in blue and the median τ_V of the sample is shown in orange.

Focusing first on the "τ_V-step", we find the global optimal step location to be $\tau_V = 2.145$, with a maximum significance of 3.27σ, a magnitude of 0.104 ± 0.032 mag and $\Delta RMS = 0.0033$. In the local case, we find the optimal step location to be $\tau_V = 1.29$, with a maximum significance of 3.40σ, a step magnitude of 0.083 ± 0.024 mag and $\Delta RMS = 0.0050$. These significance levels are lower than those of the "mass-step", but the measured steps are still significant at $> 3\sigma$.

It should be mentioned that, in the global case, there is another slightly less significant candidate for the optimal step location, namely at $\tau_V = 1.78$. For this step location we have $\Delta RMS = 0.0040$, making it more meaningful than the location indicated by the maximum significance, as it results in an larger improvement to the Hubble residuals description. The reason for high significance of the $\tau_V = 2.145$ is simply a consequence of the small number of data points with $\tau_V > 2.145$, which ends up skewing the results.

Looking at Figs. 3.5 and 3.8, it becomes clear that the values obtained for the optimal step locations coincide fairly closely with the median values of τ_V close to the optimal "mass-step" locations. For this reason, it is safe to conclude that the "τ_V-step" simply recovers the original "mass-step" relation. The fact that the relation between the stellar mass and τ_V is not monotonic leads naturally to a larger level of

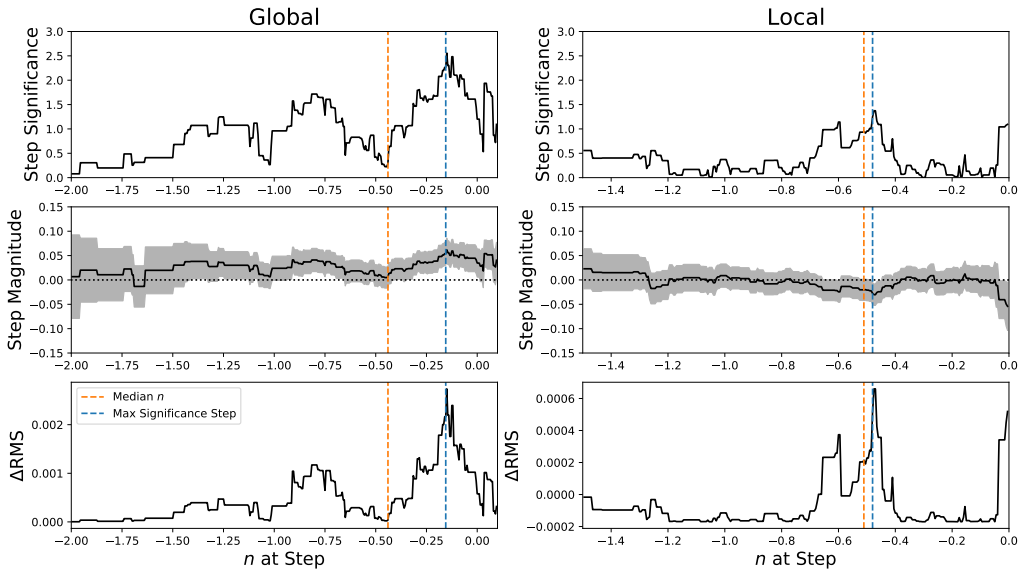

Figure 4.10: Evolution of the "n-step" significance, magnitude and ΔRMS using SNe Ia standard β calibration for the global (Left panels) and local (Right panels) cases. In each case, and for each step location, the top panel shows the significance of the step in σ, the middle panel shows the magnitude of the step in solid black, with the grey region showing the uncertainty, and the lower panel shows the difference between RMS_{mean} and RMS_{step}. In these three panels, the location of the step of maximum significance is shown in blue and the median n of the sample is shown in orange.

scatter in Hubble residuals, as there is not a one-to-one correspondence between the two stellar mass populations and the two τ_V populations. This is probably one of the causes behind the lower significance values observed.

In the case of the "n-step", we find the global optimal step location to be $n = -0.15$, with a maximum significance of 2.56σ, a magnitude of 0.062 ± 0.024 mag and $\Delta RMS = 0.0027$. In the local case, we find the optimal step location to be $n = -0.475$, with a maximum significance of 1.37σ, a step magnitude of 0.030 ± 0.022 mag and $\Delta RMS = 0.0006$. These are simultaneously the lowest step significance levels, magnitudes and ΔRMS observed for the standard calibration. Once again, these step values appear to match Figs. 3.5 and 3.8, although the higher level of scatter makes a direct comparison more difficult. Once again, the non-monotonic relation between n and the stellar mass further complicates the analysis.

Overall, evidence for both a "τ_V-step" and a "n-step" is present, but these appear to be reflections of the same tendency described by the "mass-step". However, judging from both the significance levels and values of ΔRMS observed for each step, the "mass step" appear to be the preferable way to describe and correct for this effect.

It might be the case, however, that looking for a "τ_V-step" or a "n-step" individually cannot account for the correct division of dust properties between the two SNe Ia populations. Thus, rather than considering only one of these parameters when dividing the two step populations, we will examine what happens when both parameters are simultaneous taken into account. Essentially, we adopt the same formalism

used above, with the difference that a two dimensional step location is now considered. We will examine 3 different population divisions:

1. One population consisting of SNe Ia with $\tau_V < \tau_{V_{\text{step}}}$ and $n < n_{\text{step}}$ and another consisting of the rest;
2. One population consisting of SNe Ia with $\tau_V < \tau_{V_{\text{step}}}$ and $n > n_{\text{step}}$ and another consisting of the rest;
3. One population consisting of SNe Ia with $\tau_V > \tau_{V_{\text{step}}}$ and $n > n_{\text{step}}$ and another consisting of the rest;

Note that the case where the population with $\tau_V > \tau_{V_{\text{step}}}$ and $n < n_{\text{step}}$ is isolated is not considered, as there are basically no SNe in this region, which is apparent from both Figs. 3.2 and 3.6,

For the first population division, the step significance, magnitude and ΔRMS are plotted in Fig. 4.11 as a function of the step locations. Additionally, the optimal steps recovered are plotted in Fig. 4.12 to better illustrate the two differentiated populations. For the global case, we find the optimal step location to be $\tau_V = 1.26$ and $n = -0.905$, with a maximum significance of 1.57σ, a magnitude of 0.041 ± 0.026 mag and $\Delta RMS = 0.0010$. In the local case, we find the optimal step location to be $\tau_V = 0.675$ and $n = -0.37$, with a maximum significance of 2.66σ, a step magnitude of 0.055 ± 0.020 mag and $\Delta RMS = 0.0024$.

For the second population division, the step significance, magnitude and ΔRMS are plotted in Fig. 4.13 as a function of the step locations, with the optimal steps recovered shown in Fig. 4.14. For the global case, we find the optimal step location to be $\tau_V = 1.81$ and $n = -0.85$, with a maximum significance of 4.11σ, a magnitude of 0.085 ± 0.020 mag and $\Delta RMS = 0.0068$. In the local case, we find the optimal step location to be $\tau_V = 0.82$ and $n = -0.975$, with a maximum significance of 4.37σ, a step magnitude of 0.091 ± 0.021 mag and $\Delta RMS = 0.0046$.

For the third population division, the step significance, magnitude and ΔRMS are plotted in Fig. 4.15 as a function of the step locations, with the optimal steps recovered shown in Fig. 4.16. For the global case, we find the optimal step location to be $\tau_V = 1.785$ and $n = -0.82$, with a maximum significance of 3.27σ, a magnitude of 0.081 ± 0.024 mag and $\Delta RMS = 0.0044$. In the local case, we find the optimal step location to be $\tau_V = 1.29$ and $n = -0.595$, with a maximum significance of 3.44σ, a step magnitude of 0.084 ± 0.024 mag and $\Delta RMS = 0.0053$.

Examining all three cases, we can see that the second division, that is, the one with one population consisting of SNe Ia with $\tau_V < \tau_{V_{\text{step}}}$ and $n > n_{\text{step}}$ and another consisting of the rest, produces the overall best step results.

4.3.3 Hubble Residuals for the R_V Calibration

With the previous results serving as a baseline, we can now examine the Hubble residuals under the second SNe Ia calibration. Following once again the procedure detailed in Section 4.3.1, the *best-fit* values found for the Global R_V calibration were $\alpha = 0.438^{+0.009}_{-0.011}$, $\beta_{\text{int}} = 4.317^{+0.013}_{-0.010}$ and $M = -19.096^{+0.010}_{-0.012}$. Additionally, we obtain $RMS = 0.442$, which represents an increase of 0.305 in relation to the standard

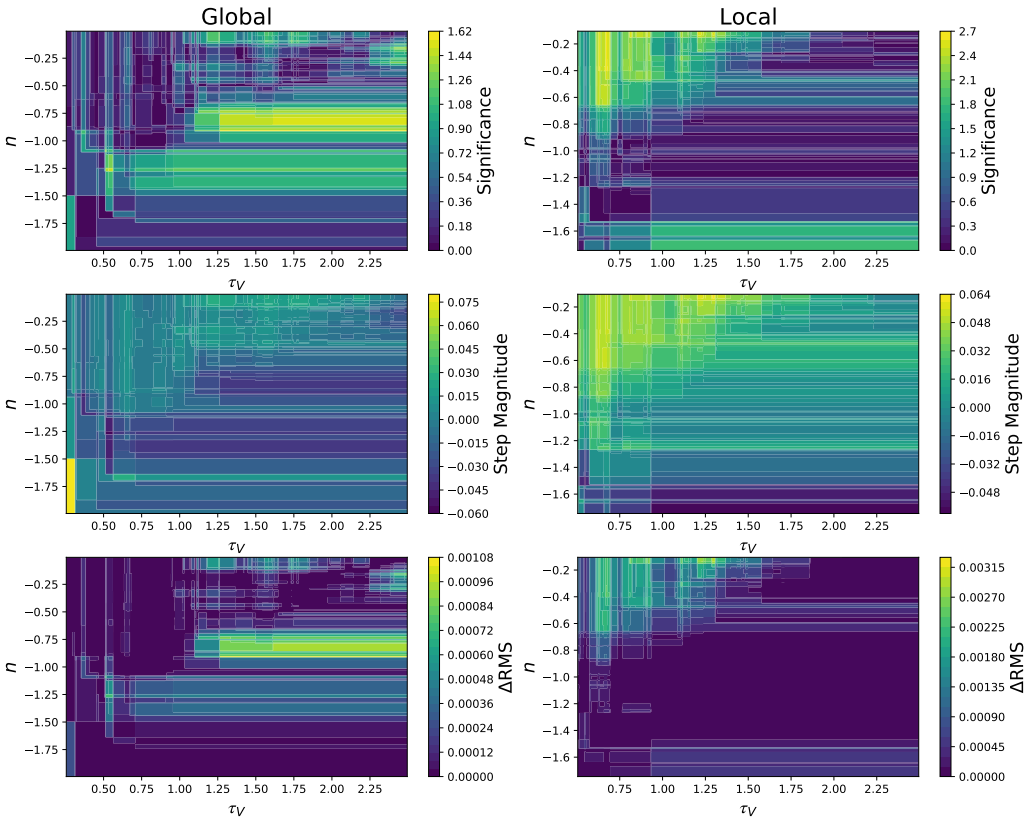

Figure 4.11: Evolution of the two dimensional "dust-step" significance, magnitude and ΔRMS using SNe Ia standard β calibration for the first population division for the global (Left panels) and local (Right panels) cases. In each case, and for each step locations, the top panel shows the significance of the step in σ, the middle panel shows the magnitude of the step in solid black, with the grey region showing the uncertainty, and the lower panel shows the difference between RMS_{mean} and RMS_{step}.

calibration. For the local R_V calibration, the *best-fit* values found were $\alpha = 0.152^{+0.010}_{-0.011}$, $\beta_{\text{int}} = 3.099^{+0.009}_{-0.011}$ and $M = -18.775^{+0.010}_{-0.009}$. In addition, we obtain $RMS = 0.622$, which represents an increase of 0.485 in relation to the standard calibration.

Overall, judging from the values of RMS, these calibrations appear to be worst fits of the data than the standard calibration, which once again indicates that host attenuation laws do not accurately describe SN extinction. It is particularly surprising that the global measurements result in a smilingly better fit than the local ones.

The Mass Step

We will now examine both calibrations' accuracy by examining the Hubble residuals and the possible "mass-step". The relevant results are plotted in Fig. 4.17. The results differ greatly from those obtained for the standard calibration. For the global case, the optimal step location is found to be $\text{Log}(M_\star/M_\odot) =$

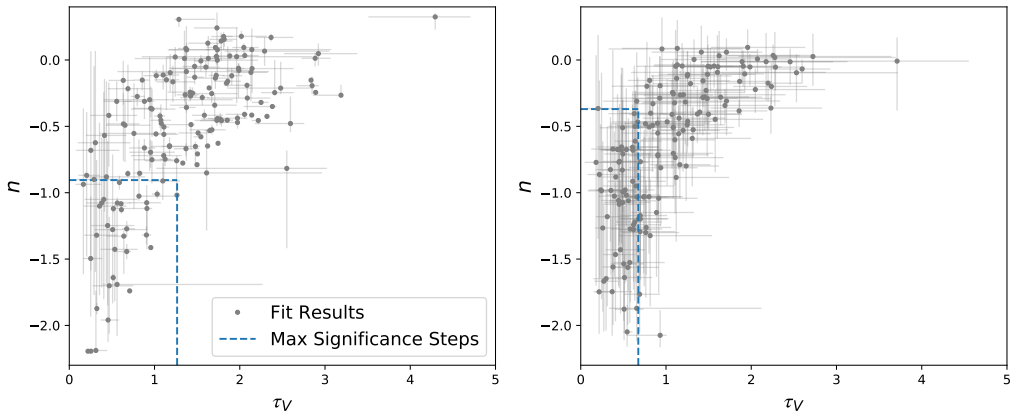

Figure 4.12: Optimal location for the two dimensional "dust-step" for the first population division, shown in blue for the global (Left panel) and local (Right panel) cases.*Best-fit* values of n as a function of τ_V for the fitted DES galaxies are also plotted, in gray.

9.22. This step corresponds to a maximum significance of 2.52σ, a step magnitude of 0.206 ± 0.079 mag and $\Delta RMS = 0.0083$. In the local case, the optimal step is $\mathrm{Log}(M_\star/M_\odot) = 9.02$, with a maximum significance of 3.47σ, a step magnitude of 0.240 ± 0.068 mag and $\Delta RMS = 0.0288$.

While taking the R_V values into account does seem to lower the significance levels of the recovered "mass-steps", this appears to be a consequence of the increased level of scatter in the Hubble residuals, as evidenced by the large step magnitudes and error margins. It should be noted, however, that the values of ΔRMS indicate the new calibration ends up strengthening the "mass-step", rather than reducing it. On the whole, it seems that the "mass-step" cannot be fully eliminated by SNe Ia calibration when considering only the attenuation laws for the respective host galaxies.

The Dust Steps

For the sake of completion, we will also analyse the behaviour of both the "τ_V-step" and the "n-step" for the new R_V calibrations. These results are displayed in Figs. 4.18 and 4.19, respectively. These plots are not particularly informative to identify possible dust related "steps", but instead show how the new R_V calibration introduces a large level of bias into the Hubble residuals, which is apparent in both the large step magnitudes and significance levels. In general, we can see that the absolute step magnitude increases with both τ_V and n, which indicates that the mean absolute value for the Hubble residuals is growing, moving further away from 0. This is once again explained by the differences between host galaxy attenuation and SN extinction, which become more pronounced as τ_V and n increase.

Overall, both these results and those obtained for the "mass-step" confirm that the SNe Ia calibration cannot be enhanced by simply including information about the host galaxy's attenuation law. A more in-depth study of the SNe inherent extinction is needed to obtain a truly correct calibration.

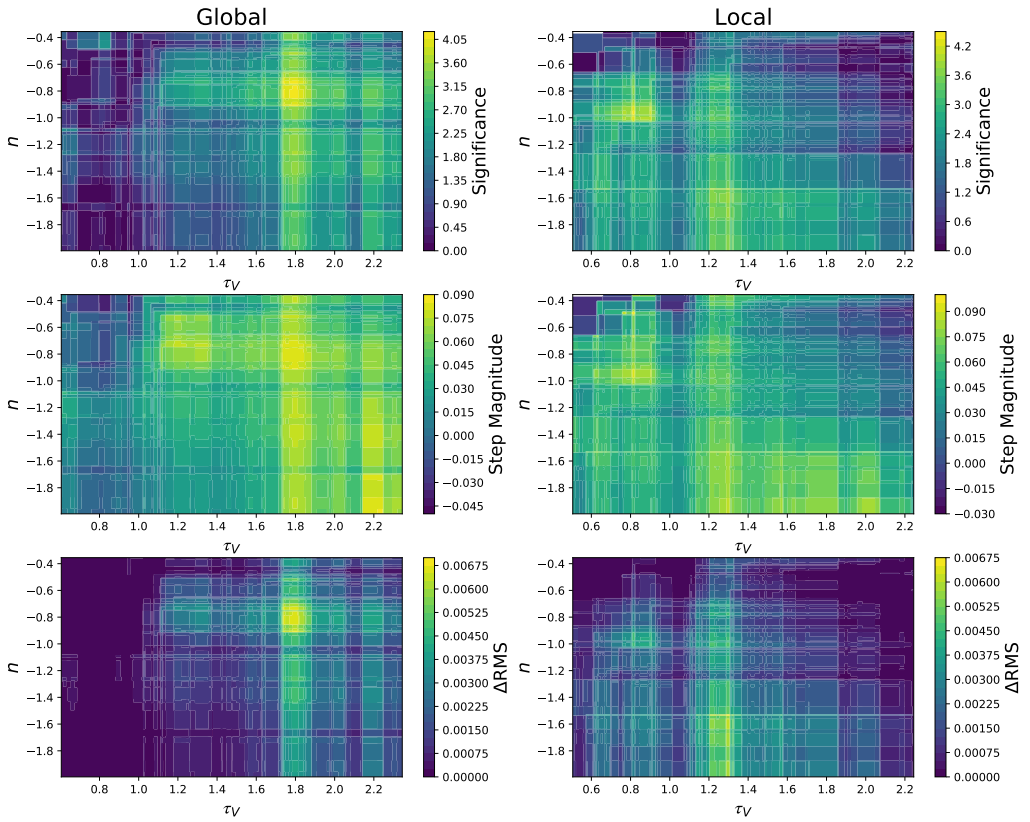

Figure 4.13: Evolution of the two dimensional "dust-step" significance, magnitude and ΔRMS using SNe Ia standard β calibration for the second population division for the global (Left panels) and local (Right panels) cases. In each case, and for each step locations, the top panel shows the significance of the step in σ, the middle panel shows the magnitude of the step in solid black, with the grey region showing the uncertainty, and the lower panel shows the difference between RMS_{mean} and RMS_{step}.

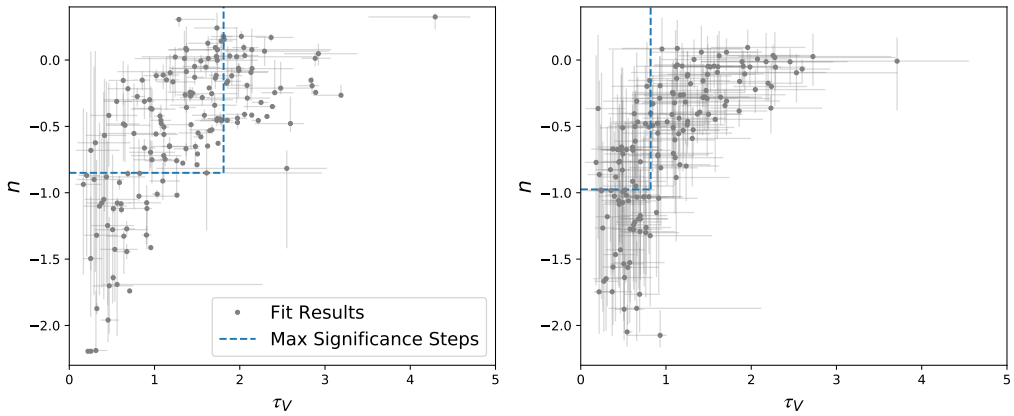

Figure 4.14: Optimal location for the two dimensional "dust-step" for the second population division, shown in blue for the global (Left panel) and local (Right panel) cases.*Best-fit* values of n as a function of τ_V for the fitted DES galaxies are also plotted, in gray.

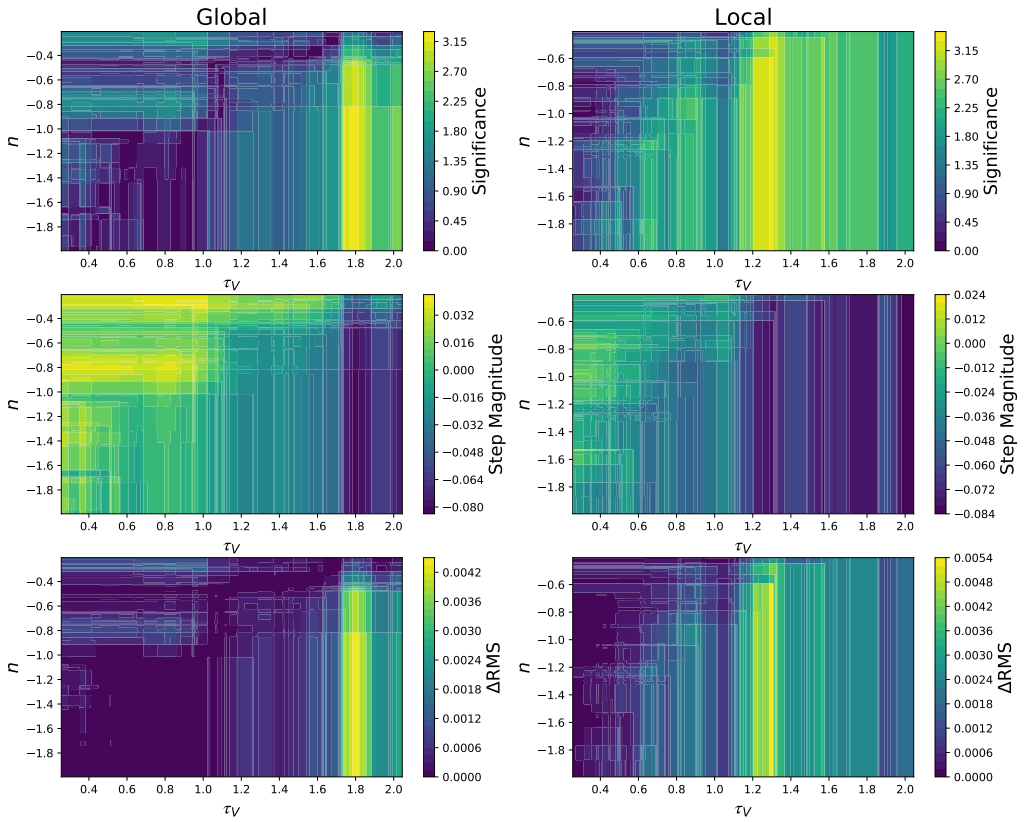

Figure 4.15: Evolution of the two dimensional "dust-step" significance, magnitude and ΔRMS using SNe Ia standard β calibration for the third population division for the global (Left panels) and local (Right panels) cases. In each case, and for each step locations, the top panel shows the significance of the step in σ, the middle panel shows the magnitude of the step in solid black, with the grey region showing the uncertainty, and the lower panel shows the difference between RMS_{mean} and RMS_{step}.

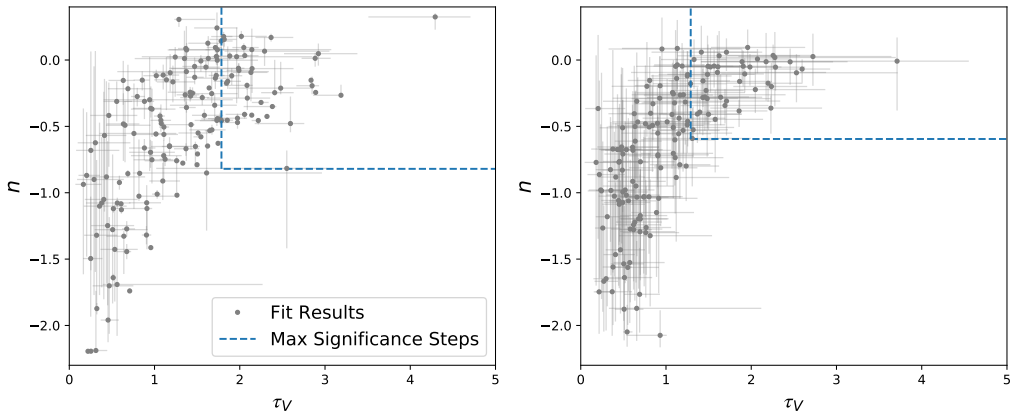

Figure 4.16: Optimal location for the two dimensional "dust-step" for the third population division, shown in blue for the global (Left panel) and local (Right panel) cases.*Best-fit* values of n as a function of τ_V for the fitted DES galaxies are also plotted, in gray.

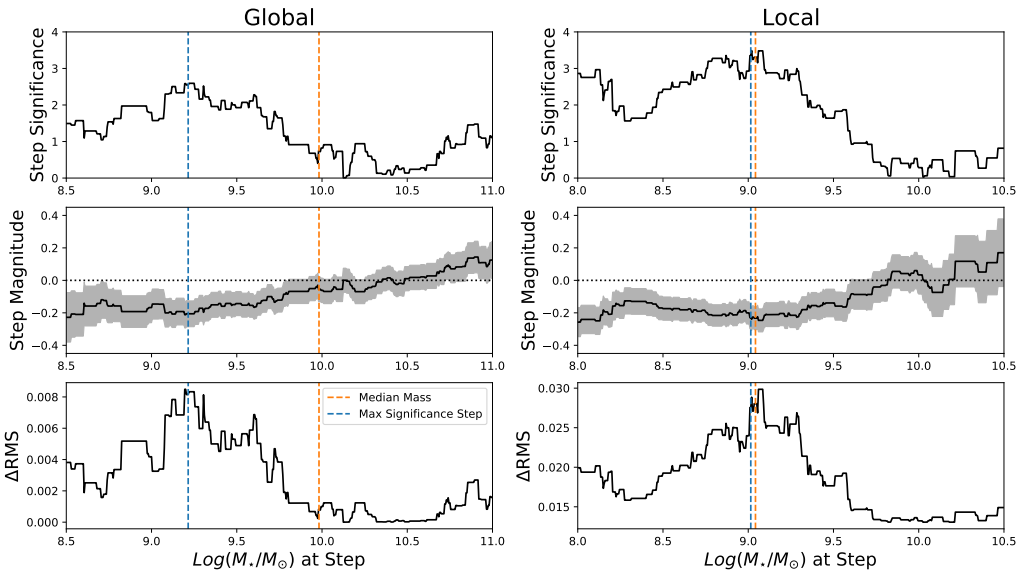

Figure 4.17: Evolution of the "mass-step" significance, magnitude and ΔRMS using SNe Ia individual β calibration for the global (Left panels) and local (Right panels) cases. In each case, and for each step location, the top panel shows the significance of the step in σ, the middle panel shows the magnitude of the step in solid black, with the grey region showing the uncertainty, and the lower panel shows the difference between RMS_{mean} and RMS_{step}. In these three panels, the location of the step of maximum significance is shown in blue and the median mass of the sample is shown in orange.

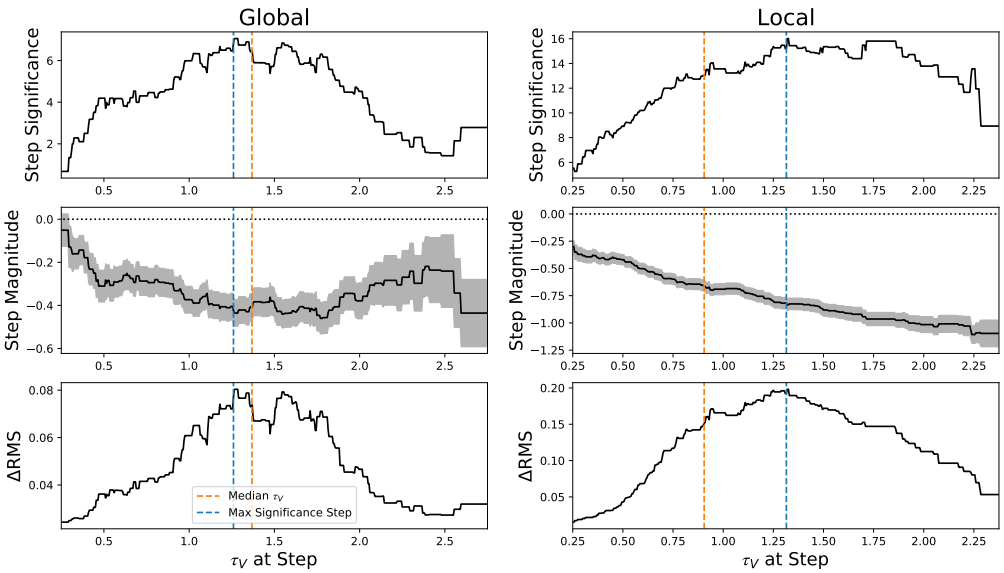

Figure 4.18: Evolution of the "τ_V-step" significance, magnitude and ΔRMS using SNe Ia individual β calibration for the global (Left panels) and local (Right panels) cases. In each case, and for each step location, the top panel shows the significance of the step in σ, the middle panel shows the magnitude of the step in solid black, with the grey region showing the uncertainty, and the lower panel shows the difference between RMS_{mean} and RMS_{step}. In these three panels, the location of the step of maximum significance is shown in blue and the median τ_V of the sample is shown in orange.

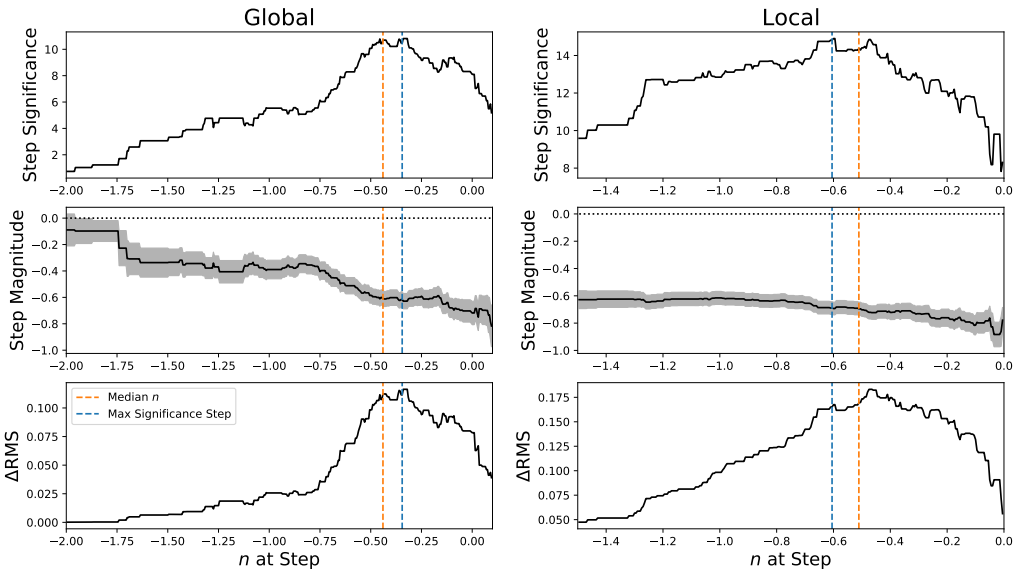

Figure 4.19: Evolution of the "n-step" significance, magnitude and ΔRMS using SNe Ia individual β calibration for the global (Left panels) and local (Right panels) cases. In each case, and for each step location, the top panel shows the significance of the step in σ, the middle panel shows the magnitude of the step in solid black, with the grey region showing the uncertainty, and the lower panel shows the difference between RMS_{mean} and RMS_{step}. In these three panels, the location of the step of maximum significance is shown in blue and the median n of the sample is shown in orange.

Chapter 5

Conclusions

The problem of SNe Ia calibration and the study of astronomical dust remain central to the field of Cosmology. In this work we have explored ways to better probe the dust contents of SNe Ia host galaxies.

We have shown through simulations that, although extra data can be helpful, DECam *griz* photometry is enough to recover dust properties for simulated SNe Ia host galaxies, provided one employs a well calibrated Bayesian fitting procedure.

Using such a method, we found that using both global and local DECam griz photometry we can recover dust properties for host galaxies that are consistent with literature predictions based on both simulations and observations. We find a relation of the dust attenuation slope with the dust optical depth, both locally and globally, that is best explained with varying star to dust geometry with galaxy orientation. Most importantly, we show that dust properties vary greatly across different galaxies, meaning a universal SNe Ia β correction cannot be assumed.

The relation between both attenuation parameters is found to be very different from the extinction relations obtained directly for SNe Ia, making the comparison between the two somewhat difficult. On one hand, the values of τ_V obtained for the hosts give a good insight into the dust optical depths affecting the respective SNe Ia, as this property is not particularly affected by dust/star geometry. On the other hand, SNe reddening does not seem to be well described by values found for the slope of the host's attenuation laws. This is due to the different phenomena involved in extinction and attenuation.

Shifting our attention to the Hubble residuals resulting from the standard SNe Ia calibration, we conclude that there is some evidence for both an individual "τ_V-step" and an individual "n-step", even though both of these appear to reflect the same tendency expressed by the "mass-step", although less clearly. However, when using both attenuation parameters to define a two dimensional "dust-step" for the global case, we were able to recover a step with roughly the same significance, magnitude and RMS improvement observed for the "mass-step". This opens the door for a fully attenuation based description of the phenomenon.

Finally, we conclude that an alternative SNe Ia calibration, incorporating both the R_V and $E(B-V)$ values obtained for the respective host galaxies as an approximation of the extinction for the SNe, results

in a worse model fit of the observed distance modulus for the SNe. This is mostly attributed to the large differences between host galaxy attenuation and SN Ia extinction, meaning the values for β_{R_V} cannot be correctly determined.

Generally, we can say that, although the results related to host galaxy attenuation presented in this work constitute an important step forward, their applicability to SNe Ia cosmology is still mostly limited and deserves further study.

Bibliography

[1] Wolfgang Hillebrandt and Jens C. Niemeyer. “Type Ia Supernova Explosion Models”. In: *Annual Review of Astronomy and Astrophysics* 38.1 (2000), 191–230. ISSN: 1545-4282. DOI: 10.1146/annurev.astro.38.1.191. URL: http://dx.doi.org/10.1146/annurev.astro.38.1.191.

[2] Ashley J. Ruiter. “Type Ia supernova sub-classes and progenitor origin”. In: *Proceedings of the International Astronomical Union* 15.S357 (2019), 1–15. ISSN: 1743-9221. DOI: 10.1017/s1743921320000587. URL: http://dx.doi.org/10.1017/S1743921320000587.

[3] Adam G. Riess et al. “Observational Evidence from Supernovae for an Accelerating Universe and a Cosmological Constant”. In: *Astronomical Journal* 116.3 (Sept. 1998), pp. 1009–1038. DOI: 10.1086/300499. arXiv: astro-ph/9805201 [astro-ph].

[4] S. Perlmutter et al. “Measurements of Ω and Λ from 42 High-Redshift Supernovae”. In: *Astrophysical Journal, Supplement* 517.2 (June 1999), pp. 565–586. DOI: 10.1086/307221. arXiv: astro-ph/9812133 [astro-ph].

[5] Robert Tripp. “A two-parameter luminosity correction for Type IA supernovae”. In: *Astronomy and Astrophysics* 331 (Mar. 1998), pp. 815–820.

[6] M. Sullivan et al. “The dependence of Type Ia Supernovae luminosities on their host galaxies”. In: *Monthly Notices of the Royal Astronomical Society* 406.2 (July 2010), pp. 782–802.

[7] R. Kessler and D. Scolnic. “Correcting Type Ia Supernova Distances for Selection Biases and Contamination in Photometrically Identified Samples”. In: *The Astrophysical Journal* 836.1 (2017), p. 56. DOI: 10.3847/1538-4357/836/1/56. URL: https://doi.org/10.3847/1538-4357/836/1/56.

[8] R Kessler et al. “First cosmology results using Type Ia supernova from the Dark Energy Survey: simulations to correct supernova distance biases”. In: *Monthly Notices of the Royal Astronomical Society* 485.1 (Feb. 2019), pp. 1171–1187. ISSN: 0035-8711. DOI: 10.1093/mnras/stz463. eprint: https://academic.oup.com/mnras/article-pdf/485/1/1171/27989728/stz463.pdf. URL: https://doi.org/10.1093/mnras/stz463.

[9] D. Brout et al. “First Cosmology Results Using SNe Ia from the Dark Energy Survey: Analysis, Systematic Uncertainties, and Validation”. In: *The Astrophysical Journal* 874.2 (2019), p. 150. ISSN: 1538-4357. DOI: 10.3847/1538-4357/ab08a0. URL: http://dx.doi.org/10.3847/1538-4357/ab08a0.

[10] J. J. Condon and A. M. Matthews. “CDM Cosmology for Astronomers”. In: *Publications of the Astronomical Society of the Pacific* 130.989 (2018), p. 073001. ISSN: 1538-3873. DOI: 10.1088/1538-3873/aac1b2. URL: http://dx.doi.org/10.1088/1538-3873/aac1b2.

[11] Samir Salim and Desika Narayanan. “The Dust Attenuation Law in Galaxies”. In: *Annual Review of Astronomy and Astrophysics* 58.1 (2020), 529–575. ISSN: 1545-4282. DOI: 10.1146/annurev-astro-032620-021933. URL: http://dx.doi.org/10.1146/annurev-astro-032620-021933.

[12] Bradley W. Carroll and Dale A. Ostlie. *An Introduction to Modern Astrophysics*. Ed. by San Francisco: Pearson Addison-Wesley. 2nd (International). 2007.

[13] S González-Gaitán et al. “The effects of varying colour-luminosity relations on type Ia supernova science”. In: *Monthly Notices of the Royal Astronomical Society* (2021). ISSN: 1365-2966. DOI: 10.1093/mnras/stab2802. URL: http://dx.doi.org/10.1093/mnras/stab2802.

[14] Samir Salim, Médéric Boquien, and Janice C. Lee. “Dust Attenuation Curves in the Local Universe: Demographics and New Laws for Star-forming Galaxies and High-redshift Analogs”. In: *The Astrophysical Journal* 859.1 (2018), p. 11. DOI: 10.3847/1538-4357/aabf3c. URL: https://doi.org/10.3847/1538-4357/aabf3c.

[15] Dark Energy Survey Collaboration: et al. “The Dark Energy Survey: more than dark energy – an overview”. In: *Monthly Notices of the Royal Astronomical Society* 460.2 (Mar. 2016), pp. 1270–1299. ISSN: 0035-8711. DOI: 10.1093/mnras/stw641. eprint: https://academic.oup.com/mnras/article-pdf/460/2/1270/8117541/stw641.pdf. URL: https://doi.org/10.1093/mnras/stw641.

[16] L Kelsey et al. “The effect of environment on Type Ia supernovae in the Dark Energy Survey three-year cosmological sample”. In: *Monthly Notices of the Royal Astronomical Society* 501.4 (2020), 4861–4876. ISSN: 1365-2966. DOI: 10.1093/mnras/staa3924. URL: http://dx.doi.org/10.1093/mnras/staa3924.

[17] D. Christopher Martin et al. “The Galaxy Evolution Explorer: A Space Ultraviolet Survey Mission”. In: *Astrophysical Journal, Letters* 619.1 (Jan. 2005), pp. L1–L6. DOI: 10.1086/426387. arXiv: astro-ph/0411302 [astro-ph].

[18] M. F. Skrutskie et al. “The Two Micron All Sky Survey (2MASS)”. In: *Astronomical Journal* 131.2 (Feb. 2006), pp. 1163–1183. DOI: 10.1086/498708.

[19] Gustavo Bruzual A. “Star clusters as simple stellar populations”. In: *Philosophical Transactions of the Royal Society A: Mathematical, Physical and Engineering Sciences* 368.1913 (2010), pp. 783–799. DOI: 10.1098/rsta.2009.0258. eprint: https://royalsocietypublishing.org/doi/pdf/10.1098/rsta.2009.0258. URL: https://royalsocietypublishing.org/doi/abs/10.1098/rsta.2009.0258.

[20] Joel Leja et al. “Deriving Physical Properties from Broadband Photometry with Prospector: Description of the Model and a Demonstration of its Accuracy Using 129 Galaxies in the Local Universe”. In: *The Astrophysical Journal* 837.2 (2017), p. 170. ISSN: 1538-4357. DOI: 10.3847/1538-4357/aa5ffe. URL: http://dx.doi.org/10.3847/1538-4357/aa5ffe.

[21] David W. Hogg and Daniel Foreman-Mackey. “Data Analysis Recipes: Using Markov Chain Monte Carlo”. In: *The Astrophysical Journal Supplement Series* 236.1 (2018), p. 11. DOI: 10.3847/1538-4365/aab76e. URL: https://doi.org/10.3847/1538-4365/aab76e.

[22] Jonathan Goodman and Jonathan Weare. “Ensemble samplers with affine invariance”. In: *Communications in Applied Mathematics and Computational Science* 5.1 (2010), 65–80. DOI: 10.2140/camcos.2010.5.65.

[23] Daniel Foreman-Mackey et al. “emcee: The MCMC Hammer”. In: *Publications of the ASP* 125.925 (Mar. 2013), p. 306. DOI: 10.1086/670067. arXiv: 1202.3665 [astro-ph.IM].

[24] P. Marigo and L. Girardi. “Evolution of asymptotic giant branch stars. I. Updated synthetic TP-AGB models and their basic calibration”. In: *Astronomy and Astrophysics* 469.1 (July 2007), pp. 239–263. DOI: 10.1051/0004-6361:20066772. arXiv: astro-ph/0703139 [astro-ph].

[25] Charlie Conroy, James E. Gunn, and Martin White. “The Propagation of Uncertainties in Stellar Population Synthesis Modeling. I. The Relevance of Uncertain Aspects of Stellar Evolution and the Initial Mass Function to the Derived Physical Properties of Galaxies”. In: *Astrophysical Journal, Supplement* 699.1 (July 2009), pp. 486–506. DOI: 10.1088/0004-637X/699/1/486. arXiv: 0809.4261 [astro-ph].

[26] Charlie Conroy and James E. Gunn. “The Propagation of Uncertainties in Stellar Population Synthesis Modeling. III. Model Calibration, Comparison, and Evaluation”. In: *Astrophysical Journal, Supplement* 712.2 (Apr. 2010), pp. 833–857. DOI: 10.1088/0004-637X/712/2/833. arXiv: 0911.3151 [astro-ph.CO].

[27] Pavel Kroupa. “On the variation of the initial mass function”. In: *Monthly Notices of the RAS* 322.2 (Apr. 2001), pp. 231–246. DOI: 10.1046/j.1365-8711.2001.04022.x. arXiv: astro-ph/0009005 [astro-ph].

[28] E R Stanway and J J Eldridge. “Re-evaluating old stellar populations”. In: *Monthly Notices of the Royal Astronomical Society* 479.1 (2018), 75–93. ISSN: 1365-2966. DOI: 10.1093/mnras/sty1353. URL: http://dx.doi.org/10.1093/mnras/sty1353.

[29] Charlie Conroy. “Modeling the Panchromatic Spectral Energy Distributions of Galaxies”. In: *Annual Review of Astronomy and Astrophysics* 51.1 (Aug. 2013), pp. 393–455. DOI: 10.1146/annurev-astro-082812-141017. arXiv: 1301.7095 [astro-ph.CO].

[30] Daniela Calzetti et al. “The Dust Content and Opacity of Actively Star-forming Galaxies”. In: *The Astrophysical Journal* 533.2 (2000), 682–695. ISSN: 1538-4357. DOI: 10.1086/308692. URL: http://dx.doi.org/10.1086/308692.

[31] Noll, S. et al. “Analysis of galaxy spectral energy distributions from far-UV to far-IR with CIGALE: studying a SINGS test sample”. In: *A&A* 507.3 (2009), pp. 1793–1813. DOI: 10.1051/0004-6361/200912497. URL: https://doi.org/10.1051/0004-6361/200912497.

[32] Mariska Kriek and Charlie Conroy. “THE DUST ATTENUATION LAW IN DISTANT GALAXIES: EVIDENCE FOR VARIATION WITH SPECTRAL TYPE”. In: *The Astrophysical Journal* 775.1 (2013), p. L16. ISSN: 2041-8213. DOI: 10.1088/2041-8205/775/1/l16. URL: http://dx.doi.org/10.1088/2041-8205/775/1/L16.

[33] M Smith et al. “First cosmology results using type Ia supernovae from the Dark Energy Survey: the effect of host galaxy properties on supernova luminosity”. In: *Monthly Notices of the Royal Astronomical Society* 494.3 (Apr. 2020), pp. 4426–4447. ISSN: 0035-8711. DOI: 10.1093/mnras/staa946. eprint: https://academic.oup.com/mnras/article-pdf/494/3/4426/33191817/staa946.pdf. URL: https://doi.org/10.1093/mnras/staa946.

[34] J. Chevallard et al. “Insights into the content and spatial distribution of dust from the integrated spectral properties of galaxies”. In: *Monthly Notices of the RAS* 432.3 (July 2013), pp. 2061–2091. DOI: 10.1093/mnras/stt523. arXiv: 1303.6631 [astro-ph.CO].

[35] P Wiseman et al. “Supernova host galaxies in the dark energy survey: I. Deep coadds, photometry, and stellar masses”. In: *Monthly Notices of the Royal Astronomical Society* 495.4 (2020), 4040–4060. ISSN: 1365-2966. DOI: 10.1093/mnras/staa1302. URL: http://dx.doi.org/10.1093/mnras/staa1302.

[36] B. Flaugher et al. “THE DARK ENERGY CAMERA”. In: *The Astronomical Journal* 150.5 (2015), p. 150. DOI: 10.1088/0004-6256/150/5/150. URL: https://doi.org/10.1088/0004-6256/150/5/150.

[37] Bertin, E. and Arnouts, S. “SExtractor: Software for source extraction”. In: *Astron. Astrophys. Suppl. Ser.* 117.2 (1996), pp. 393–404. DOI: 10.1051/aas:1996164. URL: https://doi.org/10.1051/aas:1996164.

[38] R. G. Kron. “Photometry of a complete sample of faint galaxies.” In: *Astrophysical Journal, Supplement* 43 (June 1980), pp. 305–325. DOI: 10.1086/190669.

[39] David J. Schlegel, Douglas P. Finkbeiner, and Marc Davis. “Maps of Dust Infrared Emission for Use in Estimation of Reddening and Cosmic Microwave Background Radiation Foregrounds”. In: *The Astrophysical Journal* 500.2 (1998), pp. 525–553. DOI: 10.1086/305772. URL: https://doi.org/10.1086/305772.

[40] E. L. Fitzpatrick. “Interstellar extinction variations in the Large Magellanic Cloud.” In: *Astrophysical Journal, Supplement* 299 (Dec. 1985), pp. 219–235. DOI: 10.1086/163694.

[41] Bradley L. and et al. *astropy/photutils: v0.6*. 2019. DOI: 10.5281/zenodo.2533376.

[42] Collin Erickson. *GauPro: Gaussian Process Fitting*. R package version 0.2.4. 2021. URL: https://CRAN.R-project.org/package=GauPro.

[43] Collin Erickson. *Introduction to gaussian processes*. 2021. URL: https://cran.r-project.org/web/packages/GauPro/vignettes/IntroductionToGPs.html.

[44] Desika Narayanan et al. “A Theory for the Variation of Dust Attenuation Laws in Galaxies”. In: *The Astrophysical Journal* 869.1 (2018), p. 70. DOI: 10.3847/1538-4357/aaed25. URL: https://doi.org/10.3847/1538-4357/aaed25.

[45] Kaisey S. Mandel, Gautham Narayan, and Robert P. Kirshner. “TYPE Ia SUPERNOVA LIGHT CURVE INFERENCE: HIERARCHICAL MODELS IN THE OPTICAL AND NEAR-INFRARED”. In: *The Astrophysical Journal* 731.2 (2011), p. 120. ISSN: 1538-4357. DOI: 10.1088/0004-637x/731/2/120. URL: http://dx.doi.org/10.1088/0004-637X/731/2/120.

[46] Christopher R. Burns et al. “THE CARNEGIE SUPERNOVA PROJECT: INTRINSIC COLORS OF TYPE Ia SUPERNOVAE”. In: *The Astrophysical Journal* 789.1 (2014), p. 32. ISSN: 1538-4357. DOI: 10.1088/0004-637x/789/1/32. URL: http://dx.doi.org/10.1088/0004-637X/789/1/32.

[47] M. Childress et al. “HOST GALAXY PROPERTIES AND HUBBLE RESIDUALS OF TYPE Ia SUPERNOVAE FROM THE NEARBY SUPERNOVA FACTORY”. In: *The Astrophysical Journal* 770.2 (2013), p. 108. ISSN: 1538-4357. DOI: 10.1088/0004-637x/770/2/108. URL: http://dx.doi.org/10.1088/0004-637X/770/2/108.

[48] Dillon Brout and Daniel Scolnic. “It’s Dust: Solving the Mysteries of the Intrinsic Scatter and Host-galaxy Dependence of Standardized Type Ia Supernova Brightnesses”. In: *The Astrophysical Journal* 909.1 (2021), p. 26. ISSN: 1538-4357. DOI: 10.3847/1538-4357/abd69b. URL: http://dx.doi.org/10.3847/1538-4357/abd69b.

[49] Michael J. I. Brown et al. “AN ATLAS OF GALAXY SPECTRAL ENERGY DISTRIBUTIONS FROM THE ULTRAVIOLET TO THE MID-INFRARED”. In: *The Astrophysical Journal Supplement Series* 212.2 (2014), p. 18. ISSN: 1538-4365. DOI: 10.1088/0067-0049/212/2/18. URL: http://dx.doi.org/10.1088/0067-0049/212/2/18.

[50] *Aperture photometry*. URL: https://sextractor.readthedocs.io/en/latest/Photom.html.

[51] *Isophotal Measurements*. URL: https://sextractor.readthedocs.io/en/latest/Position.html.

Appendix A

Galaxy Test Data

In this appendix we present the parameters used to simulate the test galaxies SEDs in Section 2.3, displayed in Tab. A.1, as well as the best-fit results obtained from fits of their respective photometric data: fits obtained with DECam *griz* photometry are displayed in Table A.2; fits obtained with GALEX *NUV*/*FUV* and DECam *griz* photometry are displayed in Table A.3; fits obtained with GALEX *NUV*/*FUV* and 2MASS *JHKs* are displayed in Table A.4; fits obtained with GALEX *NUV*/*FUV*, 2MASS *JHKs* and DECam *griz* photometry are displayed in Table A.5.

Table A.1: Parameters used to simulate each test galaxy.

Galaxy	Log($M_\star/M_\odot$)	Log($Z_\star/Z_\odot$)	t_{age} (Gyr)	τ_V	n	z
1	8.22	1.70	8.38	2.08	-1.98	0.22
2	8.23	2.47	10.63	0.56	-1.65	0.55
3	10.58	1.49	5.56	0.36	-1.84	0.34
4	10.99	-1.17	2.44	3.59	0.17	0.37
5	10.15	0.52	1.23	3.98	-0.33	0.18
6	9.00	1.20	6.44	2.97	-1.74	0.08
7	10.67	0.91	12.26	4.23	-0.71	0.01
8	8.91	0.37	8.13	0.24	-2.00	0.23
9	8.47	-0.34	3.93	4.72	-1.72	0.23
10	8.36	-0.43	8.25	3.50	-1.07	0.55
11	11.18	1.50	10.65	0.47	-0.59	0.05
12	10.47	1.52	12.42	2.64	-0.15	0.35
13	9.85	-0.88	3.37	2.92	-1.29	0.03
14	10.06	-0.23	4.12	5.13	-0.81	0.46
15	8.11	-1.10	11.76	1.46	-0.62	0.20
16	11.84	1.45	0.94	1.87	-0.67	0.41
17	10.51	1.74	8.19	1.77	-0.95	0.07
18	8.03	-1.30	1.56	4.60	-1.62	0.39
19	10.01	0.68	5.73	5.69	-1.25	0.19
20	8.45	1.00	8.61	1.41	-1.07	0.05
21	10.54	1.17	13.28	0.99	0.14	0.28
22	10.67	-0.50	10.46	3.42	0.35	0.01
23	8.61	2.05	11.77	3.44	-0.51	0.16
24	10.52	1.06	3.19	1.68	-2.04	0.36
25	8.55	1.29	1.33	3.34	-0.86	0.51

Table A.1: Continued from above.

Galaxy	Log($M_\star/M_\odot$)	Log($Z_\star/Z_\odot$)	t_{age} (Gyr)	τ_V	n	z
26	11.30	-0.18	4.69	3.44	-0.88	0.43
27	11.71	-0.45	0.52	2.59	0.36	0.56
28	8.54	-0.80	2.03	4.95	-0.95	0.01
29	10.66	0.90	0.41	4.60	-0.91	0.37
30	12.00	-1.20	5.08	4.73	-0.25	0.05
31	9.43	1.22	7.28	4.16	-0.38	0.03
32	8.01	2.03	4.69	5.94	-0.55	0.37
33	11.83	0.12	5.42	3.26	-0.14	0.24
34	8.81	2.25	9.60	5.96	-0.29	0.27
35	11.20	1.14	2.22	2.23	-2.15	0.18
36	10.68	1.74	9.96	5.76	0.07	0.50
37	11.47	1.71	2.25	2.91	-1.10	0.04
38	11.69	0.37	2.53	2.17	0.25	0.11
39	8.41	-1.59	8.91	0.88	-1.31	0.11
40	9.12	-0.43	4.80	3.91	-0.95	0.58
41	9.38	0.13	1.48	5.95	-2.13	0.08
42	9.39	0.32	0.00	1.26	-0.78	0.04
43	11.76	-0.59	4.49	1.21	-0.28	0.18
44	11.11	0.01	6.11	0.53	-0.13	0.07
45	11.19	-0.49	4.16	1.02	-0.95	0.49
46	10.74	1.15	6.35	3.39	-0.00	0.12
47	10.54	-1.41	3.45	2.08	-0.75	0.06
48	10.30	2.17	13.31	1.69	-0.37	0.09
49	10.27	-0.40	10.89	0.50	-1.36	0.07
50	10.86	-0.37	12.15	5.73	-1.58	0.23
51	11.88	1.06	3.28	2.66	-1.27	0.25
52	10.40	1.72	10.95	3.57	-0.92	0.06
53	11.49	0.40	7.38	1.80	-0.86	0.08
54	9.05	-1.42	12.51	4.47	-2.03	0.11
55	8.03	2.29	7.06	1.44	0.04	0.51
56	8.14	-0.96	3.16	1.87	-0.42	0.42
57	11.56	-0.04	3.82	5.75	0.01	0.54
58	11.43	2.49	11.20	0.89	-0.07	0.29
59	8.96	-0.10	13.05	1.30	-0.28	0.23
60	9.21	0.11	5.50	5.57	-0.30	0.34
61	8.33	-0.89	6.77	0.78	-1.62	0.35
62	9.84	-0.00	5.21	3.02	-1.04	0.58
63	10.73	-0.10	11.87	2.76	0.25	0.33
64	10.20	0.02	1.12	2.46	-0.33	0.40
65	10.41	-0.66	9.06	4.59	-0.67	0.41
66	11.71	1.61	12.72	3.98	0.34	0.12
67	8.33	1.52	12.53	3.78	-1.36	0.52
68	10.98	-1.34	10.79	3.19	-1.48	0.54
69	9.70	-0.22	5.30	3.07	-0.39	0.42
70	10.35	-0.25	9.86	1.67	-0.86	0.19
71	10.02	-1.54	13.58	0.75	-1.21	0.22
72	10.91	2.14	12.22	2.98	-1.99	0.03
73	8.59	1.84	8.31	4.87	0.26	0.54
74	8.80	0.78	7.86	0.08	-0.58	0.26

Table A.1: Continued from above.

Galaxy	$\mathrm{Log}(M_\star/M_\odot)$	$\mathrm{Log}(Z_\star/Z_\odot)$	t_{age} (Gyr)	τ_V	n	z
75	10.55	-1.69	4.16	0.03	-0.38	0.57

Table A.2: *Best-fit* results for the test galaxies fits with DECam *griz* photometry.

Galaxy	$\mathrm{Log}(Z_\star/Z_\odot)$	t_{age} (Gyr)	τ_V	n
1	$1.71^{+0.09}_{-0.99}$	$7.46^{+1.53}_{-0.99}$	$2.52^{+2.24}_{-0.42}$	$-2.04^{+0.15}_{-0.11}$
2	$2.33^{+0.13}_{-0.14}$	$13.29^{+0.32}_{-1.33}$	$0.95^{+0.20}_{-0.22}$	$-1.42^{+0.39}_{-0.42}$
3	$0.62^{+0.96}_{-1.70}$	$5.38^{+3.92}_{-2.43}$	$1.32^{+1.12}_{-0.77}$	$-0.35^{+0.30}_{-0.99}$
4	$0.42^{+1.11}_{-1.71}$	$4.40^{+2.46}_{-2.52}$	$2.19^{+1.25}_{-1.03}$	$0.09^{+0.15}_{-0.38}$
5	$-0.03^{+1.16}_{-1.04}$	$1.56^{+1.68}_{-0.96}$	$3.75^{+0.91}_{-0.93}$	$-0.41^{+0.21}_{-0.30}$
6	$0.01^{+0.89}_{-1.20}$	$9.36^{+2.82}_{-2.87}$	$3.42^{+0.63}_{-0.55}$	$-1.68^{+0.34}_{-0.35}$
7	$1.12^{+0.49}_{-1.23}$	$10.99^{+1.97}_{-3.06}$	$4.22^{+1.18}_{-1.24}$	$-0.67^{+0.24}_{-0.15}$
8	$-0.39^{+0.69}_{-0.93}$	$10.15^{+2.51}_{-3.00}$	$0.54^{+0.42}_{-0.29}$	$-0.99^{+0.58}_{-0.68}$
9	$-0.34^{+1.22}_{-1.01}$	$2.44^{+1.35}_{-0.96}$	$5.25^{+0.47}_{-0.55}$	$-1.65^{+0.16}_{-0.20}$
10	$1.69^{+0.33}_{-1.07}$	$1.56^{+5.28}_{-1.02}$	$4.49^{+1.04}_{-1.46}$	$-0.99^{+0.15}_{-0.26}$
11	$1.08^{+0.49}_{-1.22}$	$6.61^{+4.63}_{-3.36}$	$1.90^{+1.65}_{-1.06}$	$-0.35^{+0.30}_{-0.37}$
12	$0.62^{+0.95}_{-1.80}$	$6.31^{+4.00}_{-2.32}$	$5.15^{+0.54}_{-1.05}$	$-0.14^{+0.08}_{-0.13}$
13	$-0.43^{+0.97}_{-0.84}$	$2.09^{+1.09}_{-0.90}$	$3.27^{+0.68}_{-0.56}$	$-1.24^{+0.35}_{-0.44}$
14	$-0.55^{+1.25}_{-0.99}$	$6.76^{+4.29}_{-3.16}$	$4.44^{+0.85}_{-0.55}$	$-0.93^{+0.15}_{-0.12}$
15	$0.23^{+0.63}_{-1.14}$	$9.87^{+2.56}_{-2.91}$	$0.93^{+0.69}_{-0.45}$	$-0.92^{+0.44}_{-0.75}$
16	$-0.78^{+1.27}_{-0.83}$	$5.29^{+2.19}_{-2.40}$	$0.67^{+0.62}_{-0.33}$	$-1.06^{+0.49}_{-0.66}$
17	$1.76^{+0.14}_{-0.08}$	$7.99^{+1.38}_{-1.74}$	$1.97^{+0.78}_{-0.54}$	$-0.92^{+0.80}_{-0.85}$
18	$-0.79^{+1.04}_{-0.79}$	$1.70^{+1.26}_{-0.89}$	$4.50^{+0.56}_{-0.58}$	$-1.62^{+0.16}_{-0.19}$
19	$0.93^{+0.63}_{-1.19}$	$9.87^{+2.57}_{-2.96}$	$4.67^{+0.89}_{-1.15}$	$-1.48^{+0.23}_{-0.24}$
20	$1.35^{+0.47}_{-0.93}$	$6.38^{+4.13}_{-3.11}$	$1.55^{+1.37}_{-0.86}$	$-0.65^{+0.43}_{-0.48}$
21	$0.50^{+0.72}_{-1.39}$	$8.74^{+3.66}_{-3.51}$	$2.51^{+1.00}_{-1.00}$	$-0.05^{+0.13}_{-0.13}$
22	$-1.30^{+0.66}_{-0.49}$	$10.62^{+2.26}_{-3.26}$	$3.72^{+0.47}_{-0.29}$	$0.32^{+0.05}_{-0.08}$
23	$2.40^{+0.02}_{-0.16}$	$2.65^{+1.47}_{-0.34}$	$5.09^{+0.70}_{-1.07}$	$-1.06^{+0.51}_{-0.37}$
24	$-0.53^{+1.37}_{-0.99}$	$3.97^{+2.31}_{-1.88}$	$2.08^{+0.68}_{-0.49}$	$-1.55^{+0.35}_{-0.36}$
25	$-0.50^{+1.11}_{-0.97}$	$2.91^{+2.65}_{-1.73}$	$3.17^{+0.93}_{-0.94}$	$-0.86^{+0.19}_{-0.30}$
26	$0.43^{+0.93}_{-1.26}$	$8.41^{+3.72}_{-3.27}$	$2.25^{+0.71}_{-0.69}$	$-1.25^{+0.25}_{-0.38}$
27	$0.10^{+0.74}_{-1.39}$	$2.21^{+1.24}_{-1.58}$	$1.01^{+1.19}_{-0.78}$	$0.20^{+0.14}_{-0.36}$
28	$-0.64^{+1.02}_{-0.86}$	$3.02^{+1.41}_{-1.30}$	$4.29^{+0.73}_{-0.64}$	$-1.33^{+0.31}_{-0.41}$
29	$-0.55^{+1.25}_{-0.98}$	$2.66^{+2.07}_{-1.39}$	$3.25^{+0.73}_{-0.71}$	$-1.25^{+0.22}_{-0.29}$
30	$0.97^{+0.64}_{-1.20}$	$7.32^{+3.96}_{-3.19}$	$2.93^{+1.28}_{-1.09}$	$-0.31^{+0.24}_{-0.20}$

Table A.2: Continued from above.

Galaxy	$\mathrm{Log}(Z_\star/Z_\odot)$	t_{age} (Gyr)	τ_V	n
31	$1.38^{+0.57}_{-0.77}$	$5.78^{+4.81}_{-2.46}$	$4.55^{+0.96}_{-0.96}$	$-0.37^{+0.12}_{-0.12}$
32	$1.71^{+0.06}_{-0.06}$	$12.20^{+1.09}_{-1.22}$	$5.13^{+0.11}_{-0.13}$	$-0.48^{+0.13}_{-0.13}$
33	$-0.23^{+1.50}_{-1.26}$	$5.87^{+4.83}_{-3.01}$	$3.21^{+1.12}_{-0.98}$	$-0.24^{+0.14}_{-0.20}$
34	$2.30^{+0.03}_{-0.03}$	$8.79^{+0.70}_{-0.93}$	$4.22^{+0.98}_{-0.93}$	$-1.09^{+0.67}_{-0.69}$
35	$-1.11^{+1.12}_{-0.64}$	$2.95^{+0.93}_{-1.23}$	$2.60^{+0.54}_{-0.33}$	$-1.80^{+0.33}_{-0.27}$
36	$1.83^{+0.01}_{-0.01}$	$12.64^{+0.13}_{-0.12}$	$5.76^{+0.15}_{-0.20}$	$-0.21^{+0.08}_{-0.08}$
37	$-0.45^{+1.22}_{-1.03}$	$3.75^{+2.31}_{-1.82}$	$3.38^{+1.02}_{-0.92}$	$-0.84^{+0.32}_{-0.52}$
38	$0.69^{+0.89}_{-1.53}$	$3.47^{+2.44}_{-1.89}$	$1.29^{+1.34}_{-0.93}$	$0.03^{+0.26}_{-0.71}$
39	$-0.15^{+1.16}_{-1.15}$	$4.67^{+2.81}_{-2.32}$	$1.17^{+1.03}_{-0.57}$	$-0.56^{+0.47}_{-0.80}$
40	$-0.46^{+1.02}_{-0.93}$	$3.27^{+3.12}_{-1.84}$	$4.28^{+0.96}_{-0.98}$	$-0.94^{+0.15}_{-0.22}$
41	$0.13^{+0.77}_{-0.69}$	$1.58^{+0.34}_{-0.54}$	$5.90^{+0.07}_{-0.12}$	$-2.13^{+0.07}_{-0.05}$
42	$-0.89^{+0.42}_{-0.57}$	$0.09^{+0.15}_{-0.08}$	$0.53^{+0.31}_{-0.35}$	$-1.26^{+0.90}_{-0.64}$
43	$-0.28^{+1.17}_{-1.08}$	$2.94^{+2.45}_{-1.77}$	$1.46^{+1.01}_{-0.86}$	$-0.17^{+0.27}_{-0.55}$
44	$0.06^{+1.03}_{-1.16}$	$5.37^{+2.75}_{-2.42}$	$0.63^{+0.88}_{-0.37}$	$-0.54^{+0.59}_{-0.96}$
45	$-0.92^{+1.34}_{-0.79}$	$4.45^{+1.59}_{-1.99}$	$0.74^{+0.60}_{-0.27}$	$-1.42^{+0.53}_{-0.50}$
46	$0.34^{+0.85}_{-1.38}$	$9.40^{+2.99}_{-3.46}$	$3.60^{+0.91}_{-0.97}$	$0.09^{+0.09}_{-0.09}$
47	$0.25^{+0.99}_{-1.05}$	$2.84^{+1.57}_{-1.25}$	$1.77^{+0.84}_{-0.52}$	$-0.96^{+0.52}_{-0.70}$
48	$2.29^{+0.12}_{-0.11}$	$12.72^{+0.73}_{-0.68}$	$1.45^{+0.17}_{-0.20}$	$-0.17^{+0.42}_{-0.44}$
49	$-0.39^{+1.01}_{-1.07}$	$7.71^{+3.56}_{-3.30}$	$0.87^{+0.96}_{-0.53}$	$-0.36^{+0.42}_{-0.82}$
50	$0.64^{+0.61}_{-0.74}$	$10.63^{+2.18}_{-3.26}$	$5.21^{+0.52}_{-0.56}$	$-1.88^{+0.17}_{-0.18}$
51	$-0.50^{+1.35}_{-1.04}$	$5.02^{+3.29}_{-2.42}$	$2.59^{+0.93}_{-0.62}$	$-1.12^{+0.33}_{-0.35}$
52	$1.43^{+0.27}_{-0.74}$	$9.88^{+2.97}_{-2.43}$	$4.50^{+1.01}_{-1.25}$	$-1.39^{+0.38}_{-0.18}$
53	$-0.29^{+1.25}_{-1.22}$	$7.02^{+3.87}_{-3.32}$	$2.24^{+1.14}_{-0.97}$	$-0.64^{+0.36}_{-0.60}$
54	$1.82^{+0.07}_{-0.03}$	$7.23^{+0.60}_{-0.68}$	$0.25^{+0.26}_{-0.16}$	$-1.56^{+1.00}_{-0.48}$
55	$2.27^{+0.05}_{-0.04}$	$6.56^{+0.64}_{-0.72}$	$1.74^{+0.76}_{-0.73}$	$-0.11^{+0.39}_{-0.65}$
56	$-0.53^{+0.84}_{-0.78}$	$0.73^{+1.48}_{-0.55}$	$3.02^{+0.98}_{-0.94}$	$-0.27^{+0.19}_{-0.21}$
57	$0.61^{+0.99}_{-1.56}$	$5.58^{+3.60}_{-2.43}$	$4.73^{+0.77}_{-0.78}$	$-0.01^{+0.08}_{-0.19}$
58	$2.35^{+0.12}_{-0.18}$	$10.83^{+1.18}_{-0.57}$	$0.88^{+0.16}_{-0.19}$	$-0.30^{+0.40}_{-0.65}$
59	$0.58^{+0.84}_{-1.62}$	$6.81^{+4.33}_{-3.27}$	$1.88^{+1.07}_{-1.23}$	$-0.22^{+0.20}_{-0.38}$
60	$0.59^{+1.04}_{-1.68}$	$5.84^{+3.60}_{-2.59}$	$5.31^{+0.47}_{-0.73}$	$-0.40^{+0.08}_{-0.15}$
61	$-0.63^{+1.29}_{-0.94}$	$4.48^{+2.20}_{-2.17}$	$1.18^{+0.75}_{-0.41}$	$-1.27^{+0.47}_{-0.53}$
62	$-0.38^{+1.11}_{-1.01}$	$3.54^{+2.84}_{-1.96}$	$3.65^{+0.87}_{-0.94}$	$-0.91^{+0.16}_{-0.25}$
63	$1.29^{+0.76}_{-1.20}$	$2.68^{+8.79}_{-2.26}$	$3.94^{+1.15}_{-1.71}$	$-0.04^{+0.24}_{-0.50}$
64	$-0.48^{+0.91}_{-0.86}$	$1.20^{+1.84}_{-0.94}$	$2.34^{+1.07}_{-0.95}$	$-0.41^{+0.28}_{-0.32}$
65	$1.03^{+0.67}_{-1.01}$	$8.81^{+3.68}_{-2.46}$	$3.40^{+0.95}_{-1.23}$	$-0.68^{+0.19}_{-0.13}$
66	$0.76^{+0.46}_{-0.45}$	$11.46^{+1.67}_{-2.72}$	$5.59^{+0.28}_{-0.47}$	$-0.05^{+0.06}_{-0.05}$

Table A.2: Continued from above.

Galaxy	$\mathrm{Log}(Z_\star/Z_\odot)$	t_{age} (Gyr)	τ_V	n
67	$1.21^{+0.08}_{-0.09}$	$11.57^{+1.51}_{-2.28}$	$4.40^{+0.13}_{-0.18}$	$-1.49^{+0.11}_{-0.10}$
68	$-0.67^{+0.92}_{-0.83}$	$9.03^{+3.22}_{-3.70}$	$3.09^{+0.62}_{-0.40}$	$-1.53^{+0.21}_{-0.15}$
69	$0.72^{+1.11}_{-1.64}$	$3.99^{+2.27}_{-1.89}$	$2.81^{+1.31}_{-1.31}$	$-0.48^{+0.22}_{-0.85}$
70	$-0.68^{+1.20}_{-0.93}$	$8.64^{+3.42}_{-3.41}$	$1.92^{+0.66}_{-0.54}$	$-0.99^{+0.34}_{-0.40}$
71	$-0.33^{+0.72}_{-0.95}$	$9.98^{+2.59}_{-2.98}$	$0.51^{+0.40}_{-0.27}$	$-0.93^{+0.54}_{-0.68}$
72	$2.22^{+0.02}_{-0.06}$	$11.29^{+0.49}_{-0.55}$	$2.73^{+0.12}_{-0.13}$	$-2.06^{+0.12}_{-0.09}$
73	$1.87^{+0.10}_{-0.03}$	$7.82^{+0.50}_{-1.45}$	$4.93^{+0.29}_{-0.16}$	$0.07^{+0.16}_{-0.17}$
74	$0.13^{+1.13}_{-1.39}$	$5.14^{+3.42}_{-2.94}$	$1.35^{+1.19}_{-0.80}$	$0.01^{+0.20}_{-0.46}$
75	$-0.10^{+0.85}_{-1.40}$	$2.35^{+0.93}_{-1.02}$	$0.30^{+0.62}_{-0.24}$	$0.04^{+0.26}_{-0.61}$

Table A.3: *Best-fit* results for the test galaxies fits with GALEX *NUV*/*FUV* and DECam *griz* photometry.

Galaxy	$\mathrm{Log}(M_\star/M_\odot)$	$\mathrm{Log}(Z_\star/Z_\odot)$	t_{age} (Gyr)	τ_V	n
1	$8.27^{+1.81}_{-0.10}$	$1.80^{+0.56}_{-0.11}$	$8.28^{+0.33}_{-1.32}$	$2.23^{+2.39}_{-0.22}$	$-1.97^{+0.07}_{-0.13}$
2	$8.23^{+0.04}_{-0.05}$	$2.45^{+0.04}_{-0.21}$	$12.09^{+1.23}_{-1.72}$	$0.83^{+2.05}_{-0.27}$	$-1.45^{+0.57}_{-0.20}$
3	$10.60^{+0.10}_{-0.12}$	$1.59^{+0.19}_{-0.28}$	$5.22^{+0.72}_{-0.58}$	$0.41^{+0.09}_{-0.10}$	$-1.76^{+0.12}_{-0.16}$
4	$10.94^{+0.05}_{-0.07}$	$1.14^{+0.24}_{-0.81}$	$5.00^{+0.74}_{-1.21}$	$1.32^{+0.99}_{-0.51}$	$-0.15^{+0.21}_{-0.24}$
5	$10.99^{+0.23}_{-0.24}$	$-0.36^{+1.13}_{-0.94}$	$2.80^{+1.25}_{-1.28}$	$3.26^{+0.91}_{-0.83}$	$0.16^{+0.06}_{-0.09}$
6	$10.54^{+0.20}_{-0.25}$	$1.40^{+0.32}_{-0.48}$	$1.96^{+1.42}_{-0.99}$	$3.75^{+0.70}_{-0.74}$	$-0.34^{+0.08}_{-0.11}$
7	$9.04^{+0.11}_{-0.16}$	$1.35^{+0.16}_{-0.17}$	$6.27^{+1.72}_{-2.33}$	$3.01^{+0.50}_{-0.51}$	$-1.73^{+0.11}_{-0.14}$
8	$10.65^{+0.13}_{-0.11}$	$1.27^{+0.18}_{-0.33}$	$9.81^{+1.25}_{-0.25}$	$3.82^{+0.73}_{-0.71}$	$-0.84^{+0.16}_{-0.16}$
9	$8.67^{+0.19}_{-0.16}$	$-0.40^{+0.79}_{-0.92}$	$6.38^{+4.02}_{-2.15}$	$0.60^{+0.26}_{-0.20}$	$-1.39^{+0.21}_{-0.27}$
10	$8.48^{+0.09}_{-0.14}$	$-0.11^{+0.79}_{-0.54}$	$3.51^{+1.13}_{-1.12}$	$4.72^{+0.19}_{-0.19}$	$-1.72^{+0.03}_{-0.03}$
11	$11.57^{+0.20}_{-0.24}$	$1.17^{+0.15}_{-0.15}$	$10.47^{+0.43}_{-0.39}$	$2.02^{+0.64}_{-0.79}$	$0.27^{+0.10}_{-0.23}$
12	$10.48^{+0.25}_{-0.17}$	$1.47^{+0.05}_{-0.23}$	$12.28^{+0.62}_{-1.82}$	$2.80^{+0.95}_{-0.41}$	$-0.11^{+0.13}_{-0.09}$
13	$10.38^{+0.12}_{-0.22}$	$0.76^{+0.37}_{-0.75}$	$7.52^{+1.15}_{-2.47}$	$2.01^{+0.54}_{-0.42}$	$-1.52^{+0.16}_{-0.18}$
14	$9.99^{+0.23}_{-0.15}$	$-0.17^{+0.92}_{-1.17}$	$3.90^{+1.78}_{-1.45}$	$5.17^{+0.39}_{-0.53}$	$-0.80^{+0.04}_{-0.06}$
15	$8.18^{+1.63}_{-0.13}$	$-1.03^{+3.33}_{-0.56}$	$11.71^{+1.62}_{-2.48}$	$1.61^{+0.49}_{-0.41}$	$-0.62^{+0.16}_{-0.20}$
16	$11.56^{+0.19}_{-0.23}$	$-0.27^{+1.03}_{-1.27}$	$1.52^{+1.49}_{-0.81}$	$1.42^{+0.27}_{-0.30}$	$-0.83^{+0.09}_{-0.12}$
17	$10.56^{+0.16}_{-0.14}$	$1.83^{+0.06}_{-0.10}$	$10.53^{+1.20}_{-2.27}$	$2.01^{+0.56}_{-0.54}$	$-0.81^{+0.20}_{-0.20}$
18	$8.04^{+0.03}_{-0.02}$	$-0.60^{+1.23}_{-0.87}$	$2.01^{+0.82}_{-0.89}$	$4.35^{+0.32}_{-0.26}$	$-1.66^{+0.05}_{-0.05}$
19	$9.91^{+0.14}_{-0.16}$	$-1.25^{+1.03}_{-0.45}$	$8.79^{+3.69}_{-2.78}$	$5.77^{+0.15}_{-0.23}$	$-1.22^{+0.03}_{-0.03}$
20	$8.40^{+0.31}_{-0.15}$	$0.67^{+0.56}_{-0.85}$	$7.71^{+1.28}_{-1.43}$	$1.95^{+0.66}_{-0.65}$	$-0.88^{+0.18}_{-0.27}$
21	$10.69^{+0.20}_{-0.20}$	$1.11^{+0.13}_{-0.17}$	$11.87^{+1.13}_{-0.95}$	$1.68^{+0.66}_{-0.69}$	$0.26^{+0.10}_{-0.21}$
22	$10.09^{+0.26}_{-0.18}$	$-0.82^{+0.60}_{-0.66}$	$6.74^{+2.03}_{-1.63}$	$2.90^{+0.56}_{-0.67}$	$-0.05^{+0.18}_{-0.15}$

Table A.3: Continued from above.

Galaxy	$\mathrm{Log}(M_\star/M_\odot)$	$\mathrm{Log}(Z_\star/Z_\odot)$	t_{age} (Gyr)	τ_V	n
23	$8.56^{+1.12}_{-0.12}$	$2.04^{+0.40}_{-0.03}$	$11.68^{+0.34}_{-1.83}$	$3.32^{+0.36}_{-0.32}$	$-0.56^{+0.06}_{-0.08}$
24	$10.98^{+0.35}_{-0.28}$	$2.07^{+0.24}_{-0.39}$	$2.14^{+0.63}_{-1.04}$	$1.94^{+1.18}_{-0.18}$	$-1.93^{+0.32}_{-0.07}$
25	$8.62^{+0.36}_{-0.20}$	$-0.08^{+1.07}_{-1.07}$	$3.80^{+2.19}_{-1.56}$	$2.92^{+0.39}_{-0.49}$	$-0.93^{+0.07}_{-0.09}$
26	$11.18^{+0.23}_{-0.15}$	$-0.07^{+0.68}_{-1.04}$	$4.61^{+1.94}_{-1.90}$	$3.43^{+0.45}_{-0.56}$	$-0.88^{+0.06}_{-0.09}$
27	$11.71^{+0.19}_{-0.22}$	$-0.59^{+0.86}_{-0.86}$	$1.52^{+0.87}_{-0.74}$	$1.56^{+0.61}_{-0.67}$	$0.26^{+0.08}_{-0.16}$
28	$9.11^{+0.05}_{-0.05}$	$1.51^{+0.04}_{-0.24}$	$8.73^{+0.51}_{-0.76}$	$1.77^{+0.82}_{-0.35}$	$-1.69^{+0.30}_{-0.17}$
29	$11.06^{+0.09}_{-0.16}$	$-1.25^{+0.86}_{-0.54}$	$6.47^{+2.68}_{-3.97}$	$3.30^{+0.66}_{-0.34}$	$-1.07^{+0.07}_{-0.06}$
30	$11.90^{+0.07}_{-0.10}$	$0.03^{+0.84}_{-0.82}$	$6.47^{+1.38}_{-1.48}$	$3.68^{+0.75}_{-0.94}$	$-0.34^{+0.09}_{-0.15}$
31	$9.53^{+0.10}_{-0.12}$	$1.15^{+0.21}_{-0.40}$	$5.03^{+1.02}_{-0.72}$	$5.56^{+0.33}_{-0.63}$	$-0.25^{+0.03}_{-0.05}$
32	$9.56^{+0.54}_{-1.54}$	$2.03^{+0.11}_{-0.15}$	$7.85^{+1.94}_{-3.03}$	$5.81^{+0.13}_{-0.34}$	$-0.58^{+0.03}_{-0.08}$
33	$11.90^{+0.07}_{-0.11}$	$-0.33^{+0.72}_{-0.65}$	$5.61^{+1.32}_{-1.76}$	$3.71^{+0.71}_{-0.74}$	$-0.07^{+0.05}_{-0.09}$
34	$8.79^{+0.04}_{-0.05}$	$2.25^{+0.12}_{-0.02}$	$9.52^{+0.45}_{-0.29}$	$5.93^{+0.05}_{-0.10}$	$-0.30^{+0.01}_{-0.02}$
35	$11.07^{+0.19}_{-0.27}$	$-0.44^{+1.05}_{-0.94}$	$2.65^{+1.53}_{-1.34}$	$2.26^{+0.14}_{-0.12}$	$-2.14^{+0.04}_{-0.04}$
36	$10.64^{+0.10}_{-0.15}$	$1.75^{+0.01}_{-0.01}$	$10.00^{+0.05}_{-0.04}$	$5.76^{+0.18}_{-0.32}$	$0.08^{+0.01}_{-0.03}$
37	$11.59^{+0.10}_{-0.14}$	$1.42^{+0.26}_{-0.20}$	$4.32^{+1.77}_{-1.57}$	$2.32^{+0.44}_{-0.49}$	$-1.26^{+0.12}_{-0.16}$
38	$11.64^{+0.20}_{-0.30}$	$-0.02^{+0.85}_{-0.99}$	$2.01^{+1.71}_{-1.30}$	$2.45^{+0.68}_{-0.86}$	$0.23^{+0.07}_{-0.09}$
39	$8.49^{+1.36}_{-0.13}$	$-0.07^{+2.44}_{-0.65}$	$8.43^{+1.59}_{-1.48}$	$0.54^{+0.38}_{-0.18}$	$-1.68^{+0.36}_{-0.28}$
40	$9.57^{+0.26}_{-0.20}$	$0.89^{+0.60}_{-0.48}$	$5.03^{+1.85}_{-1.45}$	$3.94^{+0.50}_{-0.52}$	$-0.95^{+0.07}_{-0.07}$
41	$9.33^{+0.04}_{-0.05}$	$0.19^{+0.72}_{-0.76}$	$1.34^{+0.44}_{-0.46}$	$5.88^{+0.08}_{-0.13}$	$-2.15^{+0.02}_{-0.02}$
42	$10.04^{+0.12}_{-0.25}$	$-1.60^{+0.55}_{-0.29}$	$0.73^{+0.62}_{-0.45}$	$0.56^{+0.18}_{-0.17}$	$-1.21^{+0.17}_{-0.21}$
43	$11.82^{+0.11}_{-0.12}$	$-1.11^{+0.91}_{-0.59}$	$5.43^{+1.87}_{-2.09}$	$1.03^{+0.56}_{-0.41}$	$-0.28^{+0.15}_{-0.25}$
44	$11.21^{+0.12}_{-0.14}$	$0.65^{+0.34}_{-0.71}$	$5.93^{+0.93}_{-1.42}$	$0.42^{+0.83}_{-0.34}$	$-0.31^{+0.38}_{-0.80}$
45	$11.27^{+0.19}_{-0.13}$	$-0.39^{+0.81}_{-0.87}$	$4.15^{+1.51}_{-1.51}$	$1.05^{+0.36}_{-0.30}$	$-0.95^{+0.15}_{-0.17}$
46	$10.75^{+0.22}_{-0.19}$	$-0.31^{+1.02}_{-0.96}$	$5.72^{+1.43}_{-1.54}$	$4.82^{+0.73}_{-1.00}$	$0.13^{+0.08}_{-0.07}$
47	$10.97^{+0.08}_{-0.12}$	$1.03^{+0.15}_{-0.24}$	$7.91^{+0.88}_{-1.42}$	$0.51^{+0.35}_{-0.20}$	$-1.62^{+0.34}_{-0.34}$
48	$10.24^{+0.05}_{-0.08}$	$2.49^{+0.00}_{-0.01}$	$2.94^{+0.12}_{-0.05}$	$2.20^{+0.23}_{-0.55}$	$-0.95^{+0.10}_{-0.20}$
49	$10.28^{+0.06}_{-0.06}$	$-0.22^{+0.27}_{-0.23}$	$11.25^{+1.87}_{-1.67}$	$0.39^{+0.21}_{-0.14}$	$-1.50^{+0.31}_{-0.33}$
50	$10.93^{+0.03}_{-0.04}$	$1.58^{+0.08}_{-0.11}$	$10.70^{+1.06}_{-1.76}$	$3.83^{+0.45}_{-0.33}$	$-1.96^{+0.10}_{-0.09}$
51	$11.47^{+0.25}_{-0.29}$	$-0.68^{+1.03}_{-0.89}$	$2.10^{+3.17}_{-1.35}$	$2.91^{+0.30}_{-0.46}$	$-1.22^{+0.06}_{-0.09}$
52	$10.36^{+0.05}_{-0.05}$	$1.73^{+0.03}_{-0.03}$	$12.20^{+0.98}_{-0.94}$	$3.04^{+0.25}_{-0.39}$	$-1.05^{+0.06}_{-0.10}$
53	$11.45^{+0.17}_{-0.12}$	$-0.87^{+0.59}_{-0.69}$	$7.70^{+2.80}_{-1.86}$	$2.47^{+0.41}_{-0.49}$	$-0.63^{+0.11}_{-0.14}$
54	$9.05^{+0.04}_{-0.04}$	$-0.48^{+0.66}_{-1.01}$	$11.91^{+1.28}_{-2.03}$	$4.16^{+0.27}_{-0.25}$	$-2.09^{+0.06}_{-0.06}$
55	$8.01^{+0.02}_{-0.01}$	$2.30^{+0.02}_{-0.03}$	$7.15^{+0.13}_{-0.16}$	$1.38^{+0.30}_{-0.26}$	$0.04^{+0.11}_{-0.12}$
56	$8.62^{+1.60}_{-0.45}$	$-0.32^{+2.52}_{-1.17}$	$1.41^{+1.13}_{-0.82}$	$3.62^{+1.47}_{-0.96}$	$-0.17^{+0.19}_{-0.12}$
57	$11.43^{+0.20}_{-0.21}$	$-0.07^{+0.80}_{-0.96}$	$4.86^{+0.94}_{-0.89}$	$5.16^{+0.58}_{-0.86}$	$-0.02^{+0.04}_{-0.07}$
58	$11.54^{+0.23}_{-0.17}$	$2.47^{+0.02}_{-0.04}$	$11.44^{+0.36}_{-0.45}$	$1.29^{+0.56}_{-0.41}$	$0.14^{+0.15}_{-0.17}$

Table A.3: Continued from above.

Galaxy	$\mathrm{Log}(M_\star/M_\odot)$	$\mathrm{Log}(Z_\star/Z_\odot)$	t_{age} (Gyr)	τ_V	n
59	$9.05^{+0.13}_{-0.11}$	$0.09^{+0.31}_{-0.16}$	$13.03^{+0.51}_{-0.65}$	$1.33^{+0.43}_{-0.38}$	$-0.27^{+0.16}_{-0.20}$
60	$9.33^{+0.17}_{-0.18}$	$0.63^{+0.41}_{-0.76}$	$5.40^{+0.92}_{-0.71}$	$5.64^{+0.27}_{-0.51}$	$-0.31^{+0.02}_{-0.04}$
61	$9.54^{+1.41}_{-1.36}$	$1.13^{+1.05}_{-2.22}$	$3.93^{+3.87}_{-2.80}$	$2.50^{+2.69}_{-1.30}$	$-1.04^{+0.54}_{-0.38}$
62	$9.87^{+0.28}_{-0.19}$	$0.19^{+1.02}_{-0.89}$	$3.89^{+2.15}_{-1.56}$	$3.43^{+0.39}_{-0.51}$	$-0.97^{+0.06}_{-0.08}$
63	$10.61^{+0.21}_{-0.17}$	$0.50^{+0.25}_{-0.30}$	$12.75^{+0.66}_{-0.67}$	$1.88^{+0.68}_{-0.52}$	$0.09^{+0.15}_{-0.16}$
64	$10.59^{+0.32}_{-0.23}$	$0.86^{+0.70}_{-1.49}$	$2.25^{+1.45}_{-1.12}$	$2.21^{+0.64}_{-0.55}$	$-0.36^{+0.11}_{-0.13}$
65	$10.25^{+0.11}_{-0.09}$	$-0.15^{+0.59}_{-0.70}$	$10.60^{+1.34}_{-0.83}$	$3.77^{+0.57}_{-0.58}$	$-0.78^{+0.09}_{-0.09}$
66	$11.62^{+0.22}_{-0.24}$	$1.63^{+0.03}_{-0.03}$	$13.00^{+0.61}_{-1.12}$	$3.66^{+0.66}_{-0.74}$	$0.29^{+0.06}_{-0.09}$
67	$8.12^{+0.20}_{-0.09}$	$1.17^{+0.28}_{-0.27}$	$11.49^{+1.51}_{-3.12}$	$4.01^{+0.44}_{-0.23}$	$-1.72^{+0.38}_{-0.13}$
68	$10.34^{+0.37}_{-0.36}$	$0.79^{+0.54}_{-0.80}$	$0.50^{+0.68}_{-0.34}$	$4.41^{+0.14}_{-0.14}$	$-1.32^{+0.02}_{-0.02}$
69	$9.98^{+0.33}_{-0.29}$	$0.98^{+0.64}_{-1.35}$	$1.54^{+1.38}_{-0.79}$	$4.91^{+0.63}_{-0.76}$	$-0.21^{+0.05}_{-0.07}$
70	$10.47^{+0.10}_{-0.08}$	$-0.51^{+0.44}_{-0.38}$	$9.38^{+2.30}_{-1.43}$	$2.08^{+0.44}_{-0.36}$	$-0.73^{+0.10}_{-0.14}$
71	$9.91^{+0.09}_{-0.15}$	$-1.24^{+0.49}_{-0.48}$	$10.85^{+1.93}_{-3.27}$	$0.57^{+0.15}_{-0.17}$	$-1.53^{+0.18}_{-0.22}$
72	$11.10^{+0.14}_{-0.10}$	$1.95^{+0.20}_{-0.07}$	$6.76^{+2.54}_{-1.44}$	$5.01^{+0.93}_{-1.03}$	$-1.92^{+0.30}_{-0.23}$
73	$8.89^{+1.19}_{-0.33}$	$1.84^{+0.37}_{-0.00}$	$8.28^{+0.13}_{-0.71}$	$5.24^{+0.55}_{-0.59}$	$0.26^{+0.05}_{-0.61}$
74	$8.78^{+0.12}_{-0.12}$	$0.46^{+0.27}_{-0.35}$	$8.01^{+0.40}_{-0.61}$	$0.25^{+0.48}_{-0.20}$	$0.24^{+0.12}_{-0.33}$
75	$10.63^{+0.21}_{-0.17}$	$0.58^{+0.60}_{-1.37}$	$2.41^{+0.68}_{-0.62}$	$0.30^{+0.33}_{-0.19}$	$-0.06^{+0.26}_{-0.45}$

Table A.4: *Best-fit* results for the test galaxies fits with 2MASS *JHKs* and DECam *griz* photometry.

Galaxy	$\mathrm{Log}(M_\star/M_\odot)$	$\mathrm{Log}(Z_\star/Z_\odot)$	t_{age} (Gyr)	τ_V	n
1	$8.14^{+0.07}_{-0.09}$	$-0.52^{+0.60}_{-0.82}$	$10.74^{+2.08}_{-2.29}$	$5.24^{+0.43}_{-0.38}$	$-2.01^{+0.14}_{-0.14}$
2	$8.22^{+0.03}_{-0.03}$	$2.41^{+0.06}_{-0.08}$	$12.21^{+0.23}_{-0.31}$	$0.79^{+0.16}_{-0.13}$	$-1.59^{+0.19}_{-0.19}$
3	$10.34^{+0.31}_{-0.46}$	$-0.47^{+0.87}_{-1.05}$	$2.99^{+3.72}_{-2.28}$	$2.28^{+0.53}_{-0.80}$	$-0.39^{+0.23}_{-0.29}$
4	$10.87^{+0.12}_{-0.16}$	$1.46^{+0.27}_{-0.61}$	$4.62^{+1.39}_{-1.64}$	$0.91^{+0.91}_{-0.52}$	$-0.60^{+0.55}_{-0.92}$
5	$10.61^{+0.30}_{-0.33}$	$-0.78^{+1.41}_{-0.84}$	$4.67^{+5.47}_{-2.87}$	$3.82^{+0.53}_{-1.13}$	$-0.23^{+0.16}_{-0.20}$
6	$8.94^{+0.23}_{-0.41}$	$0.71^{+0.62}_{-1.08}$	$5.61^{+4.79}_{-3.51}$	$3.74^{+0.68}_{-0.67}$	$-1.59^{+0.38}_{-0.37}$
7	$10.66^{+0.09}_{-0.15}$	$0.96^{+0.58}_{-1.14}$	$11.18^{+1.79}_{-4.64}$	$4.37^{+1.15}_{-1.13}$	$-0.73^{+0.19}_{-0.19}$
8	$8.87^{+0.17}_{-0.45}$	$0.00^{+0.48}_{-0.89}$	$7.28^{+4.28}_{-4.75}$	$0.80^{+0.56}_{-0.50}$	$-0.90^{+0.55}_{-0.78}$
9	$8.86^{+0.17}_{-0.33}$	$-1.28^{+0.60}_{-0.48}$	$7.40^{+4.28}_{-4.10}$	$4.97^{+0.32}_{-0.29}$	$-1.62^{+0.09}_{-0.11}$
10	$8.26^{+0.14}_{-0.14}$	$0.28^{+1.00}_{-0.94}$	$7.24^{+3.91}_{-1.93}$	$2.95^{+0.55}_{-0.65}$	$-1.24^{+0.15}_{-0.30}$
11	$11.18^{+0.08}_{-0.18}$	$1.15^{+0.30}_{-0.94}$	$10.49^{+2.15}_{-4.73}$	$1.21^{+1.09}_{-0.66}$	$-0.57^{+0.35}_{-0.51}$
12	$9.90^{+0.12}_{-0.14}$	$1.91^{+0.22}_{-0.19}$	$4.32^{+1.09}_{-1.28}$	$2.38^{+0.47}_{-0.36}$	$-1.08^{+0.34}_{-0.42}$
13	$10.16^{+0.25}_{-0.49}$	$-0.12^{+0.52}_{-0.78}$	$6.02^{+5.15}_{-4.41}$	$2.55^{+0.60}_{-0.54}$	$-1.48^{+0.34}_{-0.42}$
14	$10.16^{+0.09}_{-0.08}$	$1.86^{+0.11}_{-0.13}$	$5.33^{+0.64}_{-0.85}$	$2.43^{+0.57}_{-0.45}$	$-1.62^{+0.38}_{-0.31}$

Table A.4: Continued from above.

Galaxy	$\mathrm{Log}(M_\star/M_\odot)$	$\mathrm{Log}(Z_\star/Z_\odot)$	t_{age} (Gyr)	τ_V	n
15	$8.07^{+0.07}_{-0.05}$	$-1.05^{+0.78}_{-0.65}$	$11.58^{+1.51}_{-1.94}$	$1.40^{+0.32}_{-0.52}$	$-0.78^{+0.26}_{-0.39}$
16	$11.68^{+0.23}_{-0.58}$	$0.99^{+0.53}_{-0.48}$	$0.72^{+0.61}_{-0.57}$	$1.81^{+0.43}_{-0.34}$	$-0.77^{+0.36}_{-0.35}$
17	$10.37^{+0.11}_{-0.13}$	$1.86^{+0.21}_{-0.15}$	$6.43^{+2.09}_{-1.51}$	$1.91^{+0.60}_{-0.58}$	$-1.64^{+0.82}_{-0.43}$
18	$8.29^{+0.27}_{-0.21}$	$-1.54^{+0.58}_{-0.33}$	$4.95^{+4.86}_{-2.55}$	$3.97^{+0.45}_{-0.30}$	$-1.71^{+0.09}_{-0.09}$
19	$10.09^{+0.08}_{-0.16}$	$0.93^{+0.55}_{-0.80}$	$10.30^{+2.30}_{-3.98}$	$4.78^{+0.77}_{-0.90}$	$-1.45^{+0.20}_{-0.22}$
20	$8.56^{+0.11}_{-0.18}$	$0.19^{+1.00}_{-0.93}$	$9.61^{+2.91}_{-3.66}$	$2.37^{+0.83}_{-0.98}$	$-0.36^{+0.20}_{-0.35}$
21	$10.08^{+0.25}_{-0.37}$	$-0.94^{+1.29}_{-0.74}$	$5.61^{+5.25}_{-3.99}$	$2.72^{+0.60}_{-0.99}$	$-0.48^{+0.19}_{-0.23}$
22	$10.51^{+0.22}_{-0.30}$	$-0.59^{+1.05}_{-0.84}$	$6.47^{+4.41}_{-3.11}$	$3.83^{+0.52}_{-0.81}$	$0.31^{+0.06}_{-0.12}$
23	$8.25^{+0.20}_{-0.16}$	$2.11^{+0.15}_{-0.20}$	$5.32^{+2.30}_{-1.36}$	$2.31^{+0.28}_{-0.27}$	$-0.67^{+0.37}_{-0.78}$
24	$10.57^{+0.36}_{-0.36}$	$-1.05^{+0.99}_{-0.65}$	$3.63^{+5.30}_{-2.89}$	$2.52^{+0.72}_{-0.57}$	$-1.25^{+0.15}_{-0.26}$
25	$8.91^{+0.30}_{-0.15}$	$1.54^{+0.42}_{-0.68}$	$3.96^{+4.01}_{-1.41}$	$2.16^{+0.60}_{-0.54}$	$-1.18^{+0.47}_{-0.56}$
26	$11.49^{+0.15}_{-0.21}$	$1.19^{+0.48}_{-0.88}$	$6.97^{+5.45}_{-2.31}$	$2.01^{+0.95}_{-0.76}$	$-1.15^{+0.26}_{-0.56}$
27	$11.91^{+0.07}_{-0.17}$	$1.02^{+0.34}_{-0.73}$	$2.93^{+0.81}_{-1.22}$	$0.45^{+0.82}_{-0.34}$	$-0.01^{+0.29}_{-0.77}$
28	$8.96^{+0.21}_{-0.40}$	$-0.36^{+1.30}_{-1.11}$	$5.90^{+4.93}_{-3.64}$	$4.34^{+0.57}_{-1.05}$	$-1.09^{+0.22}_{-0.49}$
29	$11.36^{+0.32}_{-0.33}$	$1.27^{+0.57}_{-0.82}$	$4.26^{+4.69}_{-2.44}$	$3.19^{+0.77}_{-0.73}$	$-1.00^{+0.28}_{-0.45}$
30	$11.79^{+0.16}_{-0.32}$	$0.84^{+0.72}_{-1.00}$	$4.24^{+2.01}_{-2.29}$	$3.56^{+0.88}_{-0.90}$	$-0.48^{+0.19}_{-0.28}$
31	$8.61^{+0.71}_{-0.33}$	$1.72^{+0.41}_{-0.84}$	$1.56^{+4.96}_{-0.76}$	$4.24^{+0.80}_{-0.61}$	$-1.13^{+0.59}_{-0.59}$
32	$8.05^{+0.09}_{-0.04}$	$1.87^{+0.05}_{-0.09}$	$5.92^{+0.80}_{-0.41}$	$5.50^{+0.21}_{-0.21}$	$-0.31^{+0.11}_{-0.08}$
33	$11.49^{+0.32}_{-0.35}$	$-0.92^{+1.24}_{-0.76}$	$2.78^{+3.71}_{-1.91}$	$3.75^{+0.60}_{-0.83}$	$-0.38^{+0.13}_{-0.19}$
34	$8.75^{+0.05}_{-0.07}$	$2.30^{+0.01}_{-0.03}$	$7.20^{+1.02}_{-0.23}$	$4.98^{+0.57}_{-0.44}$	$0.21^{+0.14}_{-0.33}$
35	$11.36^{+0.33}_{-0.45}$	$-0.99^{+0.65}_{-0.69}$	$4.34^{+5.36}_{-3.44}$	$2.57^{+0.59}_{-0.39}$	$-1.68^{+0.22}_{-0.26}$
36	$9.85^{+0.09}_{-0.09}$	$1.82^{+0.01}_{-0.03}$	$12.83^{+0.16}_{-0.16}$	$3.72^{+0.53}_{-0.42}$	$-0.92^{+0.21}_{-0.25}$
37	$11.68^{+0.21}_{-0.16}$	$1.64^{+0.42}_{-0.84}$	$4.12^{+2.52}_{-1.37}$	$2.14^{+1.06}_{-0.95}$	$-1.07^{+0.44}_{-0.61}$
38	$11.79^{+0.08}_{-0.14}$	$1.66^{+0.22}_{-0.54}$	$3.66^{+0.85}_{-0.99}$	$0.65^{+0.70}_{-0.43}$	$-0.33^{+0.50}_{-0.90}$
39	$8.42^{+0.11}_{-0.23}$	$-0.71^{+0.46}_{-0.78}$	$9.03^{+3.30}_{-3.80}$	$0.69^{+0.41}_{-0.31}$	$-1.01^{+0.53}_{-0.68}$
40	$9.25^{+0.15}_{-0.31}$	$-0.32^{+0.84}_{-1.04}$	$7.14^{+4.01}_{-3.55}$	$3.40^{+0.54}_{-0.61}$	$-1.10^{+0.10}_{-0.15}$
41	$10.09^{+0.16}_{-0.34}$	$-0.52^{+0.53}_{-0.72}$	$7.86^{+3.96}_{-4.07}$	$5.70^{+0.22}_{-0.33}$	$-2.03^{+0.13}_{-0.12}$
42	$10.11^{+0.26}_{-0.34}$	$-1.28^{+1.40}_{-0.53}$	$0.79^{+1.07}_{-0.68}$	$0.97^{+0.36}_{-0.82}$	$-0.11^{+0.38}_{-0.77}$
43	$11.75^{+0.18}_{-0.31}$	$-0.80^{+0.61}_{-0.74}$	$5.04^{+2.75}_{-2.89}$	$0.96^{+0.47}_{-0.56}$	$-0.38^{+0.39}_{-0.50}$
44	$11.16^{+0.21}_{-0.36}$	$0.08^{+0.56}_{-0.87}$	$5.85^{+4.16}_{-3.49}$	$0.79^{+0.71}_{-0.56}$	$-0.29^{+0.49}_{-0.85}$
45	$11.37^{+0.33}_{-0.31}$	$0.27^{+0.42}_{-0.66}$	$4.82^{+5.32}_{-2.56}$	$0.67^{+0.53}_{-0.44}$	$-1.27^{+0.49}_{-0.54}$
46	$10.12^{+0.36}_{-0.47}$	$1.85^{+0.28}_{-0.55}$	$2.78^{+3.02}_{-1.58}$	$2.38^{+0.71}_{-0.54}$	$-0.89^{+0.67}_{-0.81}$
47	$10.64^{+0.29}_{-0.48}$	$-0.10^{+0.52}_{-0.82}$	$5.20^{+5.48}_{-3.86}$	$1.45^{+0.58}_{-0.61}$	$-1.16^{+0.46}_{-0.54}$
48	$10.22^{+0.04}_{-0.04}$	$2.20^{+0.06}_{-0.05}$	$13.56^{+0.18}_{-0.38}$	$1.16^{+0.25}_{-0.27}$	$-0.96^{+0.36}_{-0.51}$
49	$10.19^{+0.23}_{-0.45}$	$-0.12^{+0.71}_{-1.06}$	$5.80^{+5.04}_{-3.99}$	$1.19^{+0.70}_{-0.80}$	$-0.39^{+0.43}_{-0.80}$
50	$10.64^{+0.14}_{-0.32}$	$-0.12^{+0.66}_{-0.69}$	$8.12^{+3.83}_{-4.14}$	$5.70^{+0.22}_{-0.44}$	$-1.85^{+0.11}_{-0.14}$

Table A.4: Continued from above.

Galaxy	$\mathrm{Log}(M_\star/M_\odot)$	$\mathrm{Log}(Z_\star/Z_\odot)$	t_{age} (Gyr)	τ_V	n
51	$11.70^{+0.22}_{-0.46}$	$-0.58^{+0.82}_{-0.86}$	$1.96^{+2.04}_{-1.50}$	$3.48^{+0.66}_{-0.59}$	$-0.90^{+0.14}_{-0.24}$
52	$10.32^{+0.15}_{-0.28}$	$1.25^{+0.47}_{-0.61}$	$6.82^{+3.54}_{-3.45}$	$5.59^{+0.30}_{-0.70}$	$-1.42^{+0.15}_{-0.25}$
53	$11.67^{+0.15}_{-0.29}$	$-0.75^{+0.83}_{-0.78}$	$8.75^{+3.53}_{-4.37}$	$2.86^{+0.44}_{-0.71}$	$-0.30^{+0.16}_{-0.21}$
54	$8.78^{+0.22}_{-0.40}$	$-0.79^{+0.59}_{-0.72}$	$6.47^{+4.82}_{-4.05}$	$4.50^{+0.32}_{-0.30}$	$-2.03^{+0.17}_{-0.12}$
55	$8.01^{+0.02}_{-0.01}$	$2.26^{+0.07}_{-0.03}$	$6.92^{+0.41}_{-0.41}$	$1.80^{+0.43}_{-0.54}$	$0.14^{+0.13}_{-0.09}$
56	$8.41^{+0.17}_{-0.28}$	$-1.29^{+0.80}_{-0.50}$	$7.59^{+4.22}_{-4.06}$	$1.23^{+0.44}_{-0.39}$	$-0.57^{+0.22}_{-0.22}$
57	$11.05^{+0.20}_{-0.13}$	$1.93^{+0.21}_{-0.32}$	$4.00^{+1.50}_{-0.84}$	$2.26^{+0.64}_{-0.58}$	$-0.92^{+0.46}_{-0.55}$
58	$11.30^{+0.08}_{-0.06}$	$2.44^{+0.05}_{-0.12}$	$12.04^{+0.69}_{-0.38}$	$0.56^{+0.19}_{-0.13}$	$-1.76^{+0.54}_{-0.32}$
59	$8.58^{+0.31}_{-0.31}$	$-0.89^{+1.08}_{-0.75}$	$4.58^{+5.17}_{-2.69}$	$2.19^{+0.52}_{-0.72}$	$-0.56^{+0.21}_{-0.29}$
60	$8.78^{+0.16}_{-0.21}$	$1.96^{+0.32}_{-0.29}$	$3.81^{+1.54}_{-1.53}$	$2.82^{+0.62}_{-0.42}$	$-1.27^{+0.38}_{-0.70}$
61	$8.33^{+0.16}_{-0.22}$	$-1.62^{+0.47}_{-0.28}$	$7.48^{+4.10}_{-3.21}$	$0.81^{+0.25}_{-0.16}$	$-1.76^{+0.31}_{-0.27}$
62	$10.13^{+0.05}_{-0.07}$	$1.57^{+0.04}_{-0.09}$	$9.33^{+0.49}_{-1.62}$	$0.42^{+0.94}_{-0.31}$	$-1.19^{+0.85}_{-0.51}$
63	$9.97^{+0.26}_{-0.66}$	$0.64^{+0.60}_{-0.72}$	$5.56^{+4.99}_{-4.55}$	$1.66^{+0.75}_{-1.00}$	$-0.90^{+0.36}_{-0.48}$
64	$10.56^{+0.30}_{-0.44}$	$-0.61^{+0.90}_{-0.91}$	$3.26^{+3.73}_{-2.53}$	$2.11^{+0.56}_{-0.76}$	$-0.30^{+0.27}_{-0.25}$
65	$10.23^{+0.07}_{-0.08}$	$1.49^{+0.14}_{-1.11}$	$12.66^{+0.76}_{-1.80}$	$1.71^{+1.72}_{-0.58}$	$-1.16^{+0.35}_{-0.50}$
66	$10.87^{+0.34}_{-0.32}$	$1.70^{+0.47}_{-0.82}$	$4.30^{+4.76}_{-1.99}$	$3.80^{+0.93}_{-0.77}$	$-0.71^{+0.32}_{-0.59}$
67	$8.11^{+0.07}_{-0.07}$	$1.20^{+0.35}_{-0.25}$	$8.66^{+3.22}_{-2.04}$	$4.06^{+0.25}_{-0.34}$	$-1.78^{+0.10}_{-0.14}$
68	$10.83^{+0.13}_{-0.27}$	$-0.22^{+0.70}_{-1.16}$	$8.27^{+3.61}_{-4.03}$	$2.75^{+0.47}_{-0.42}$	$-1.69^{+0.16}_{-0.16}$
69	$9.54^{+0.27}_{-0.35}$	$-0.63^{+1.15}_{-0.95}$	$4.89^{+4.08}_{-3.24}$	$2.92^{+0.55}_{-0.72}$	$-0.51^{+0.16}_{-0.22}$
70	$10.23^{+0.16}_{-0.35}$	$-1.05^{+0.63}_{-0.61}$	$7.91^{+4.05}_{-4.64}$	$2.03^{+0.37}_{-0.39}$	$-1.06^{+0.21}_{-0.28}$
71	$9.87^{+0.12}_{-0.26}$	$-1.00^{+0.48}_{-0.62}$	$8.89^{+3.31}_{-4.08}$	$0.67^{+0.28}_{-0.27}$	$-1.28^{+0.46}_{-0.51}$
72	$10.96^{+0.05}_{-0.06}$	$1.94^{+0.06}_{-0.04}$	$8.14^{+1.24}_{-1.04}$	$2.42^{+0.19}_{-0.15}$	$-2.06^{+0.15}_{-0.10}$
73	$8.07^{+0.14}_{-0.05}$	$1.85^{+0.01}_{-0.00}$	$8.16^{+0.16}_{-0.15}$	$3.62^{+0.43}_{-0.15}$	$0.03^{+0.09}_{-0.06}$
74	$8.58^{+0.26}_{-0.31}$	$-1.00^{+0.95}_{-0.71}$	$5.34^{+4.38}_{-3.17}$	$1.32^{+0.50}_{-0.66}$	$-0.34^{+0.38}_{-0.37}$
75	$10.34^{+0.15}_{-0.20}$	$-1.23^{+0.77}_{-0.52}$	$2.29^{+0.91}_{-0.93}$	$0.14^{+0.22}_{-0.10}$	$-0.54^{+0.61}_{-0.83}$

Table A.5: *Best-fit* results for the test galaxies fits with GALEX *NUV*/*FUV*, 2MASS *JHKs* and DECam *griz* photometry.

Galaxy	$\mathrm{Log}(M_\star/M_\odot)$	$\mathrm{Log}(Z_\star/Z_\odot)$	t_{age} (Gyr)	τ_V	n
1	$8.13^{+0.07}_{-0.08}$	$-0.38^{+0.55}_{-0.86}$	$10.38^{+2.30}_{-2.14}$	$5.14^{+0.49}_{-0.31}$	$-2.05^{+0.16}_{-0.11}$
2	$8.26^{+0.02}_{-0.03}$	$2.46^{+0.03}_{-0.05}$	$12.72^{+0.15}_{-2.02}$	$0.79^{+0.07}_{-0.08}$	$-1.43^{+0.05}_{-0.07}$
3	$10.55^{+0.04}_{-0.04}$	$1.38^{+0.11}_{-0.12}$	$5.85^{+0.59}_{-0.53}$	$0.34^{+0.06}_{-0.06}$	$-1.87^{+0.11}_{-0.11}$
4	$10.94^{+0.05}_{-0.07}$	$1.14^{+0.24}_{-0.81}$	$5.00^{+0.74}_{-1.21}$	$1.32^{+0.99}_{-0.51}$	$-0.15^{+0.21}_{-0.24}$
5	$11.10^{+0.06}_{-0.06}$	$-1.63^{+0.24}_{-0.25}$	$12.16^{+0.85}_{-0.59}$	$3.90^{+0.18}_{-0.19}$	$-0.01^{+0.03}_{-0.03}$
6	$9.02^{+0.09}_{-0.14}$	$1.27^{+0.10}_{-0.13}$	$6.28^{+1.47}_{-1.70}$	$3.07^{+0.37}_{-0.36}$	$-1.71^{+0.08}_{-0.09}$

Table A.5: Continued from above.

Galaxy	$\mathrm{Log}(M_\star/M_\odot)$	$\mathrm{Log}(Z_\star/Z_\odot)$	t_{age} (Gyr)	τ_V	n
7	$10.70^{+0.07}_{-0.04}$	$0.94^{+0.17}_{-0.09}$	$11.55^{+1.47}_{-1.46}$	$4.29^{+0.17}_{-0.20}$	$-0.71^{+0.04}_{-0.06}$
8	$8.77^{+0.10}_{-0.13}$	$0.22^{+0.20}_{-0.19}$	$6.25^{+1.37}_{-1.57}$	$0.52^{+0.25}_{-0.18}$	$-1.54^{+0.22}_{-0.25}$
9	$8.47^{+0.09}_{-0.13}$	$-0.13^{+0.36}_{-0.28}$	$3.61^{+0.80}_{-0.96}$	$4.72^{+0.17}_{-0.17}$	$-1.72^{+0.03}_{-0.03}$
10	$8.40^{+0.06}_{-0.10}$	$0.43^{+0.29}_{-0.78}$	$10.86^{+1.91}_{-2.08}$	$2.76^{+0.56}_{-0.30}$	$-1.20^{+0.10}_{-0.06}$
11	$11.17^{+0.05}_{-0.04}$	$1.42^{+0.07}_{-0.09}$	$10.97^{+0.61}_{-0.42}$	$0.59^{+0.28}_{-0.25}$	$-0.36^{+0.24}_{-0.35}$
12	$10.34^{+0.06}_{-0.06}$	$1.52^{+0.03}_{-0.04}$	$12.47^{+0.44}_{-0.48}$	$2.34^{+0.20}_{-0.17}$	$-0.21^{+0.05}_{-0.05}$
13	$10.09^{+0.19}_{-0.29}$	$-0.20^{+0.33}_{-0.40}$	$5.31^{+2.64}_{-2.81}$	$2.55^{+0.56}_{-0.43}$	$-1.35^{+0.11}_{-0.12}$
14	$10.22^{+0.14}_{-0.23}$	$0.41^{+0.43}_{-0.69}$	$5.78^{+1.76}_{-2.25}$	$4.61^{+0.67}_{-0.53}$	$-0.86^{+0.07}_{-0.06}$
15	$8.02^{+0.02}_{-0.01}$	$0.56^{+0.13}_{-0.14}$	$9.56^{+0.65}_{-0.58}$	$0.48^{+0.13}_{-0.12}$	$-1.48^{+0.14}_{-0.18}$
16	$11.79^{+0.16}_{-0.35}$	$1.33^{+0.23}_{-0.50}$	$1.05^{+0.44}_{-0.66}$	$1.68^{+0.27}_{-0.17}$	$-0.73^{+0.06}_{-0.06}$
17	$10.48^{+0.04}_{-0.07}$	$1.73^{+0.01}_{-0.01}$	$8.55^{+0.92}_{-0.47}$	$1.72^{+0.36}_{-0.43}$	$-1.00^{+0.12}_{-0.37}$
18	$8.04^{+0.03}_{-0.02}$	$-1.55^{+0.50}_{-0.28}$	$1.86^{+0.93}_{-0.78}$	$4.49^{+0.31}_{-0.33}$	$-1.64^{+0.05}_{-0.06}$
19	$9.93^{+0.12}_{-0.10}$	$0.23^{+0.37}_{-0.32}$	$6.28^{+1.33}_{-1.10}$	$5.65^{+0.26}_{-0.35}$	$-1.25^{+0.03}_{-0.04}$
20	$8.66^{+0.05}_{-0.05}$	$-0.82^{+0.18}_{-0.41}$	$12.37^{+1.03}_{-1.58}$	$2.96^{+0.30}_{-0.22}$	$-0.41^{+0.04}_{-0.05}$
21	$10.33^{+0.05}_{-0.05}$	$1.22^{+0.07}_{-0.10}$	$12.79^{+0.68}_{-0.92}$	$0.56^{+0.27}_{-0.19}$	$-0.21^{+0.20}_{-0.23}$
22	$10.68^{+0.06}_{-0.07}$	$-0.78^{+0.23}_{-0.44}$	$9.85^{+0.76}_{-1.09}$	$3.75^{+0.31}_{-0.26}$	$0.32^{+0.06}_{-0.07}$
23	$8.48^{+0.05}_{-0.05}$	$2.04^{+0.02}_{-0.02}$	$11.73^{+0.18}_{-0.20}$	$3.14^{+0.17}_{-0.15}$	$-0.57^{+0.04}_{-0.04}$
24	$10.52^{+0.20}_{-0.11}$	$0.80^{+0.40}_{-0.99}$	$3.48^{+4.25}_{-0.89}$	$1.67^{+0.07}_{-0.24}$	$-2.04^{+0.03}_{-0.07}$
25	$8.83^{+0.16}_{-0.20}$	$0.98^{+0.32}_{-0.30}$	$3.32^{+2.57}_{-1.29}$	$2.92^{+0.31}_{-0.53}$	$-0.93^{+0.05}_{-0.10}$
26	$11.45^{+0.10}_{-0.20}$	$0.52^{+0.32}_{-0.48}$	$7.15^{+1.72}_{-2.39}$	$2.71^{+0.62}_{-0.44}$	$-1.00^{+0.11}_{-0.09}$
27	$11.92^{+0.05}_{-0.10}$	$1.17^{+0.21}_{-0.37}$	$3.33^{+0.47}_{-0.68}$	$0.19^{+0.40}_{-0.15}$	$-0.50^{+0.51}_{-0.78}$
28	$8.68^{+0.15}_{-0.17}$	$-0.89^{+0.73}_{-0.66}$	$2.46^{+2.02}_{-1.24}$	$4.93^{+0.44}_{-0.61}$	$-0.95^{+0.05}_{-0.08}$
29	$10.90^{+0.20}_{-0.28}$	$0.82^{+0.31}_{-0.38}$	$1.41^{+0.95}_{-0.73}$	$4.16^{+0.19}_{-0.21}$	$-0.97^{+0.02}_{-0.03}$
30	$11.93^{+0.05}_{-0.07}$	$-0.01^{+0.63}_{-0.75}$	$5.79^{+0.97}_{-1.12}$	$3.98^{+0.59}_{-0.63}$	$-0.32^{+0.06}_{-0.08}$
31	$9.40^{+0.03}_{-0.03}$	$1.38^{+0.08}_{-0.15}$	$7.21^{+0.36}_{-0.47}$	$3.86^{+0.43}_{-0.31}$	$-0.43^{+0.06}_{-0.05}$
32	$8.02^{+0.03}_{-0.01}$	$1.72^{+0.02}_{-0.02}$	$12.46^{+0.26}_{-0.23}$	$4.97^{+0.10}_{-0.08}$	$-0.59^{+0.01}_{-0.01}$
33	$11.84^{+0.06}_{-0.07}$	$0.01^{+0.80}_{-0.89}$	$6.74^{+1.18}_{-1.15}$	$3.00^{+0.75}_{-0.85}$	$-0.15^{+0.09}_{-0.14}$
34	$8.69^{+0.04}_{-0.21}$	$2.24^{+0.03}_{-0.01}$	$9.45^{+0.18}_{-0.62}$	$5.76^{+0.12}_{-0.70}$	$-0.31^{+0.02}_{-0.11}$
35	$11.09^{+0.14}_{-0.23}$	$0.18^{+0.32}_{-0.40}$	$2.58^{+1.10}_{-1.20}$	$2.26^{+0.13}_{-0.11}$	$-2.14^{+0.04}_{-0.03}$
36	$10.38^{+0.08}_{-0.09}$	$1.76^{+0.01}_{-0.01}$	$10.03^{+0.04}_{-0.03}$	$5.05^{+0.26}_{-0.26}$	$0.02^{+0.03}_{-0.03}$
37	$11.63^{+0.09}_{-0.12}$	$1.61^{+0.10}_{-0.11}$	$3.62^{+1.04}_{-0.97}$	$2.54^{+0.26}_{-0.28}$	$-1.20^{+0.07}_{-0.08}$
38	$11.84^{+0.08}_{-0.13}$	$1.03^{+0.34}_{-0.78}$	$3.88^{+0.92}_{-1.28}$	$1.40^{+0.80}_{-0.57}$	$0.17^{+0.10}_{-0.17}$
39	$8.43^{+0.08}_{-0.10}$	$-0.80^{+0.32}_{-0.66}$	$9.55^{+2.17}_{-2.26}$	$0.65^{+0.30}_{-0.20}$	$-1.48^{+0.21}_{-0.24}$
40	$9.34^{+0.09}_{-0.21}$	$0.36^{+0.39}_{-0.65}$	$7.91^{+1.63}_{-2.54}$	$3.07^{+0.62}_{-0.40}$	$-1.08^{+0.09}_{-0.07}$
41	$9.33^{+0.05}_{-0.05}$	$0.30^{+0.22}_{-0.22}$	$1.27^{+0.21}_{-0.19}$	$5.90^{+0.07}_{-0.10}$	$-2.15^{+0.02}_{-0.02}$
42	$9.94^{+0.24}_{-0.28}$	$-1.39^{+1.03}_{-0.46}$	$0.34^{+1.35}_{-0.29}$	$0.88^{+0.30}_{-0.60}$	$-0.94^{+0.15}_{-0.64}$

Table A.5: Continued from above.

Galaxy	$\mathrm{Log}(M_\star/M_\odot)$	$\mathrm{Log}(Z_\star/Z_\odot)$	t_{age} (Gyr)	τ_V	n
43	$11.85^{+0.10}_{-0.12}$	$-1.32^{+0.59}_{-0.44}$	$6.14^{+1.47}_{-1.33}$	$0.99^{+0.27}_{-0.28}$	$-0.26^{+0.16}_{-0.20}$
44	$11.12^{+0.10}_{-0.11}$	$-0.16^{+0.68}_{-0.92}$	$5.01^{+1.05}_{-1.29}$	$1.08^{+0.64}_{-0.66}$	$-0.01^{+0.18}_{-0.31}$
45	$11.60^{+0.06}_{-0.08}$	$0.25^{+0.16}_{-0.17}$	$8.34^{+0.85}_{-0.99}$	$0.26^{+0.14}_{-0.09}$	$-1.68^{+0.24}_{-0.23}$
46	$10.63^{+0.05}_{-0.05}$	$1.16^{+0.14}_{-0.31}$	$7.33^{+0.66}_{-0.87}$	$2.77^{+0.57}_{-0.43}$	$-0.05^{+0.07}_{-0.08}$
47	$10.36^{+0.15}_{-0.21}$	$-0.74^{+0.64}_{-0.72}$	$1.86^{+1.71}_{-1.02}$	$2.20^{+0.49}_{-0.53}$	$-0.76^{+0.10}_{-0.14}$
48	$10.22^{+0.05}_{-0.13}$	$2.24^{+0.12}_{-0.05}$	$13.09^{+0.27}_{-2.41}$	$1.29^{+0.17}_{-0.24}$	$-0.56^{+0.10}_{-0.19}$
49	$10.33^{+0.03}_{-0.04}$	$0.32^{+0.18}_{-0.20}$	$9.74^{+0.69}_{-0.72}$	$0.29^{+0.13}_{-0.09}$	$-1.84^{+0.24}_{-0.24}$
50	$10.88^{+0.02}_{-0.03}$	$-0.67^{+0.22}_{-0.21}$	$13.05^{+0.54}_{-0.96}$	$5.94^{+0.05}_{-0.09}$	$-1.56^{+0.01}_{-0.01}$
51	$11.44^{+0.30}_{-0.47}$	$0.28^{+0.31}_{-0.30}$	$1.42^{+1.74}_{-1.05}$	$3.07^{+0.21}_{-0.33}$	$-1.18^{+0.04}_{-0.07}$
52	$10.43^{+0.04}_{-0.03}$	$1.74^{+0.03}_{-0.04}$	$10.93^{+0.59}_{-0.33}$	$3.44^{+0.20}_{-0.18}$	$-0.96^{+0.04}_{-0.04}$
53	$11.73^{+0.06}_{-0.12}$	$-0.88^{+0.21}_{-0.54}$	$11.42^{+1.71}_{-3.10}$	$2.67^{+0.31}_{-0.24}$	$-0.44^{+0.05}_{-0.09}$
54	$9.04^{+0.03}_{-0.03}$	$-0.96^{+0.52}_{-0.64}$	$12.55^{+0.88}_{-1.29}$	$4.28^{+0.21}_{-0.26}$	$-2.07^{+0.05}_{-0.06}$
55	$8.02^{+0.03}_{-0.01}$	$2.38^{+0.08}_{-0.12}$	$13.34^{+0.36}_{-3.77}$	$2.73^{+0.45}_{-0.39}$	$-1.25^{+0.39}_{-0.36}$
56	$8.23^{+0.07}_{-0.08}$	$-1.25^{+0.70}_{-0.52}$	$4.52^{+0.88}_{-0.99}$	$1.52^{+0.30}_{-0.36}$	$-0.51^{+0.08}_{-0.13}$
57	$11.45^{+0.06}_{-0.07}$	$0.96^{+0.23}_{-0.59}$	$6.07^{+0.54}_{-0.77}$	$3.97^{+0.66}_{-0.44}$	$-0.12^{+0.06}_{-0.05}$
58	$11.31^{+0.05}_{-0.05}$	$2.43^{+0.05}_{-0.11}$	$10.95^{+0.27}_{-0.31}$	$0.68^{+0.12}_{-0.11}$	$-0.17^{+0.10}_{-0.11}$
59	$8.95^{+0.03}_{-0.03}$	$0.21^{+0.25}_{-0.19}$	$13.18^{+0.42}_{-0.54}$	$0.99^{+0.21}_{-0.21}$	$-0.43^{+0.12}_{-0.16}$
60	$9.15^{+0.05}_{-0.05}$	$1.53^{+0.03}_{-0.05}$	$12.13^{+0.48}_{-0.77}$	$2.53^{+0.18}_{-0.12}$	$-0.69^{+0.05}_{-0.03}$
61	$8.22^{+0.10}_{-0.13}$	$-1.61^{+0.42}_{-0.27}$	$5.28^{+1.96}_{-1.69}$	$1.03^{+0.23}_{-0.22}$	$-1.47^{+0.11}_{-0.12}$
62	$9.75^{+0.13}_{-0.16}$	$-0.57^{+0.47}_{-0.74}$	$4.56^{+1.92}_{-1.86}$	$3.26^{+0.40}_{-0.46}$	$-1.00^{+0.06}_{-0.08}$
63	$10.41^{+0.06}_{-0.05}$	$0.61^{+0.18}_{-0.25}$	$13.02^{+0.55}_{-0.69}$	$1.32^{+0.32}_{-0.26}$	$-0.07^{+0.13}_{-0.13}$
64	$10.47^{+0.13}_{-0.16}$	$-1.01^{+0.90}_{-0.66}$	$2.35^{+1.18}_{-0.99}$	$2.33^{+0.44}_{-0.46}$	$-0.33^{+0.06}_{-0.09}$
65	$10.26^{+0.06}_{-0.05}$	$-0.16^{+0.55}_{-0.65}$	$10.45^{+1.17}_{-0.70}$	$3.82^{+0.47}_{-0.51}$	$-0.77^{+0.08}_{-0.08}$
66	$11.45^{+0.08}_{-0.09}$	$1.64^{+0.03}_{-0.02}$	$13.25^{+0.41}_{-0.88}$	$3.04^{+0.23}_{-0.24}$	$0.21^{+0.04}_{-0.05}$
67	$8.12^{+0.09}_{-0.08}$	$1.17^{+0.29}_{-0.21}$	$9.67^{+2.78}_{-2.77}$	$4.08^{+0.25}_{-0.24}$	$-1.76^{+0.12}_{-0.12}$
68	$10.97^{+0.05}_{-0.04}$	$-1.41^{+0.48}_{-0.40}$	$11.29^{+1.42}_{-1.22}$	$3.18^{+0.10}_{-0.17}$	$-1.48^{+0.02}_{-0.03}$
69	$9.64^{+0.08}_{-0.07}$	$-1.04^{+0.82}_{-0.66}$	$5.73^{+0.80}_{-0.79}$	$3.11^{+0.32}_{-0.51}$	$-0.38^{+0.05}_{-0.09}$
70	$10.35^{+0.06}_{-0.05}$	$-0.40^{+0.20}_{-0.22}$	$10.24^{+1.74}_{-1.23}$	$1.69^{+0.24}_{-0.20}$	$-0.85^{+0.07}_{-0.08}$
71	$9.87^{+0.11}_{-0.18}$	$-1.02^{+0.33}_{-0.46}$	$9.50^{+2.72}_{-3.44}$	$0.56^{+0.17}_{-0.16}$	$-1.57^{+0.18}_{-0.19}$
72	$10.94^{+0.09}_{-0.08}$	$1.92^{+0.11}_{-0.08}$	$6.51^{+1.46}_{-0.96}$	$5.78^{+0.14}_{-0.33}$	$-1.67^{+0.06}_{-0.12}$
73	$8.26^{+0.45}_{-0.09}$	$1.84^{+0.00}_{-0.00}$	$8.38^{+0.33}_{-0.08}$	$4.15^{+1.34}_{-0.23}$	$0.21^{+0.09}_{-0.03}$
74	$8.72^{+0.04}_{-0.04}$	$0.47^{+0.16}_{-0.23}$	$8.21^{+0.26}_{-0.43}$	$0.10^{+0.24}_{-0.08}$	$0.09^{+0.23}_{-0.54}$
75	$10.50^{+0.07}_{-0.12}$	$-1.69^{+0.53}_{-0.22}$	$3.24^{+0.57}_{-0.72}$	$0.13^{+0.16}_{-0.08}$	$-0.37^{+0.32}_{-0.42}$

Appendix B

DES Fit Data

In this appendix we present the best-fit results obtained from the global and local photometric fits of 162 of the DES SN Ia's host galaxies, discussed in Section 3.3. These are displayed in Tables B.1 and B.2, respectively. Furthermore, the results for additional global photometry fits for 33 of those galaxies, discussed in Section 3.4, are displayed in Table B.3.

Table B.1: *Best-fit* results for the DES host galaxies fits with DECam *griz* global photometry.

SNID	$\mathrm{Log}(Z_\star/Z_\odot)$	t_{age} (Gyr)	τ_V	n
1248677	$-0.01^{+0.07}_{-0.09}$	$0.40^{+0.07}_{-0.03}$	$1.37^{+0.05}_{-0.09}$	$0.09^{+0.02}_{-0.06}$
1250017	$-1.64^{+0.31}_{-0.18}$	$0.36^{+0.54}_{-0.14}$	$1.11^{+0.21}_{-0.38}$	$-0.72^{+0.12}_{-0.18}$
1253039	$0.16^{+0.91}_{-0.66}$	$0.21^{+0.33}_{-0.18}$	$2.29^{+0.76}_{-0.47}$	$0.07^{+0.10}_{-0.11}$
1253101	$-0.57^{+0.71}_{-0.63}$	$0.93^{+0.66}_{-0.49}$	$0.76^{+0.50}_{-0.41}$	$-0.55^{+0.38}_{-0.57}$
1253920	$-1.98^{+0.04}_{-0.02}$	$2.34^{+0.15}_{-0.15}$	$0.91^{+0.06}_{-0.05}$	$-1.32^{+0.07}_{-0.07}$
1255502	$1.29^{+0.01}_{-0.01}$	$0.24^{+0.00}_{-0.00}$	$2.89^{+0.02}_{-0.02}$	$-0.24^{+0.01}_{-0.01}$
1257366	$-1.66^{+0.35}_{-0.05}$	$2.45^{+0.61}_{-0.11}$	$0.64^{+0.04}_{-0.20}$	$-1.33^{+0.04}_{-0.28}$
1257695	$-1.96^{+0.44}_{-0.03}$	$0.17^{+0.28}_{-0.01}$	$1.26^{+0.04}_{-0.37}$	$-0.76^{+0.04}_{-0.24}$
1258906	$0.13^{+0.48}_{-0.50}$	$0.38^{+0.23}_{-0.16}$	$1.18^{+0.17}_{-0.21}$	$-0.10^{+0.14}_{-0.14}$
1258940	$-0.05^{+0.22}_{-0.20}$	$1.15^{+0.49}_{-0.15}$	$1.42^{+0.06}_{-0.26}$	$-0.24^{+0.04}_{-0.07}$
1259412	$-2.00^{+0.25}_{-0.00}$	$0.30^{+0.10}_{-0.01}$	$1.54^{+0.01}_{-0.09}$	$-0.58^{+0.01}_{-0.01}$
1261579	$-1.00^{+1.25}_{-0.43}$	$5.45^{+0.26}_{-1.45}$	$0.31^{+0.13}_{-0.05}$	$-2.19^{+0.45}_{-0.01}$
1263369	$-0.88^{+0.24}_{-0.15}$	$0.56^{+0.17}_{-0.14}$	$1.99^{+0.13}_{-0.14}$	$-0.08^{+0.05}_{-0.04}$
1263715	$0.01^{+0.56}_{-0.51}$	$0.87^{+0.36}_{-0.30}$	$0.63^{+0.19}_{-0.20}$	$-0.48^{+0.23}_{-0.28}$
1275946	$-0.67^{+1.02}_{-0.91}$	$1.60^{+0.55}_{-0.62}$	$0.45^{+0.31}_{-0.19}$	$-1.25^{+0.64}_{-0.60}$
1279500	$-1.70^{+0.25}_{-0.22}$	$0.51^{+0.39}_{-0.15}$	$1.51^{+0.12}_{-0.23}$	$-0.55^{+0.02}_{-0.02}$
1280217	$-0.09^{+1.02}_{-0.71}$	$0.09^{+0.54}_{-0.09}$	$1.96^{+0.89}_{-1.11}$	$0.02^{+0.22}_{-0.35}$
1281668	$-0.09^{+0.18}_{-0.15}$	$0.56^{+0.11}_{-0.08}$	$1.71^{+0.08}_{-0.10}$	$0.09^{+0.02}_{-0.04}$
1281886	$-0.59^{+0.55}_{-0.32}$	$1.56^{+0.46}_{-0.52}$	$0.97^{+0.28}_{-0.25}$	$-0.37^{+0.15}_{-0.21}$
1282736	$-1.95^{+0.14}_{-0.04}$	$0.78^{+0.13}_{-0.05}$	$1.65^{+0.03}_{-0.06}$	$-0.53^{+0.03}_{-0.01}$

Table B.1: Continued from above.

SNID	$\mathrm{Log}(Z_\star/Z_\odot)$	t_{age} (Gyr)	τ_V	n
1282757	$-1.97^{+0.57}_{-0.03}$	$0.11^{+0.21}_{-0.01}$	$1.73^{+0.03}_{-0.38}$	$-0.42^{+0.02}_{-0.03}$
1283373	$-0.54^{+0.07}_{-0.07}$	$4.91^{+0.03}_{-0.03}$	$0.56^{+0.03}_{-0.03}$	$-1.08^{+0.04}_{-0.05}$
1283878	$1.29^{+0.00}_{-0.26}$	$0.10^{+0.18}_{-0.00}$	$3.19^{+0.01}_{-0.33}$	$-0.27^{+0.08}_{-0.00}$
1283936	$-0.48^{+0.32}_{-0.48}$	$0.52^{+0.11}_{-0.24}$	$1.74^{+0.25}_{-0.14}$	$0.08^{+0.05}_{-0.12}$
1284587	$-1.92^{+0.20}_{-0.07}$	$0.70^{+0.39}_{-0.12}$	$1.66^{+0.08}_{-0.19}$	$-0.63^{+0.02}_{-0.02}$
1285317	$-0.06^{+0.50}_{-0.68}$	$0.56^{+0.15}_{-0.20}$	$0.17^{+0.21}_{-0.09}$	$-0.94^{+0.57}_{-0.68}$
1286398	$-0.13^{+0.03}_{-0.01}$	$3.39^{+0.02}_{-0.03}$	$0.52^{+0.01}_{-0.01}$	$-1.12^{+0.02}_{-0.03}$
1287626	$-0.76^{+0.79}_{-0.74}$	$1.20^{+0.44}_{-0.51}$	$0.35^{+0.32}_{-0.18}$	$-1.10^{+0.63}_{-0.67}$
1289288	$-1.61^{+0.17}_{-0.11}$	$0.67^{+0.34}_{-0.12}$	$1.85^{+0.07}_{-0.18}$	$-0.45^{+0.02}_{-0.02}$
1289555	$-0.10^{+0.42}_{-0.38}$	$0.61^{+0.25}_{-0.29}$	$0.46^{+0.33}_{-0.22}$	$-0.42^{+0.25}_{-0.39}$
1289600	$-0.59^{+0.15}_{-0.05}$	$0.19^{+0.07}_{-0.04}$	$1.63^{+0.16}_{-0.23}$	$0.13^{+0.02}_{-0.03}$
1289656	$-0.33^{+0.98}_{-1.04}$	$0.95^{+0.38}_{-0.38}$	$0.32^{+0.24}_{-0.15}$	$-1.32^{+0.57}_{-0.54}$
1289664	$-0.09^{+0.88}_{-0.90}$	$0.48^{+0.94}_{-0.37}$	$1.37^{+0.97}_{-0.81}$	$-0.09^{+0.34}_{-0.67}$
1290816	$0.33^{+0.36}_{-0.38}$	$0.58^{+0.18}_{-0.14}$	$1.14^{+0.15}_{-0.14}$	$-0.15^{+0.17}_{-0.23}$
1291080	$-0.35^{+1.11}_{-1.14}$	$1.57^{+0.66}_{-0.74}$	$0.51^{+0.41}_{-0.21}$	$-1.28^{+0.57}_{-0.56}$
1291090	$-0.11^{+0.21}_{-0.39}$	$0.39^{+0.08}_{-0.06}$	$0.86^{+0.09}_{-0.10}$	$-0.15^{+0.07}_{-0.08}$
1291794	$-1.69^{+0.23}_{-0.21}$	$0.84^{+0.56}_{-0.14}$	$1.78^{+0.05}_{-0.25}$	$-0.46^{+0.03}_{-0.04}$
1292145	$-0.53^{+0.37}_{-0.31}$	$0.26^{+0.20}_{-0.14}$	$1.74^{+0.48}_{-0.37}$	$-0.00^{+0.10}_{-0.14}$
1292332	$-0.85^{+0.30}_{-0.37}$	$3.38^{+0.10}_{-0.20}$	$0.67^{+0.10}_{-0.06}$	$-1.27^{+0.06}_{-0.06}$
1292336	$-1.89^{+0.13}_{-0.08}$	$1.36^{+0.51}_{-0.35}$	$0.91^{+0.17}_{-0.21}$	$-1.08^{+0.13}_{-0.20}$
1292560	$0.28^{+0.35}_{-0.38}$	$0.18^{+0.09}_{-0.07}$	$1.73^{+0.24}_{-0.27}$	$0.24^{+0.12}_{-0.20}$
1293319	$-0.74^{+0.38}_{-0.38}$	$0.65^{+0.20}_{-0.28}$	$1.22^{+0.26}_{-0.19}$	$-0.16^{+0.12}_{-0.15}$
1293758	$-2.00^{+0.00}_{-0.00}$	$0.77^{+0.01}_{-0.01}$	$1.50^{+0.00}_{-0.01}$	$-0.79^{+0.00}_{-0.01}$
1294014	$-0.08^{+0.35}_{-0.31}$	$0.53^{+0.18}_{-0.14}$	$0.63^{+0.13}_{-0.17}$	$-0.15^{+0.15}_{-0.18}$
1294743	$-1.99^{+0.29}_{-0.01}$	$0.19^{+0.12}_{-0.01}$	$2.06^{+0.04}_{-0.22}$	$-0.41^{+0.02}_{-0.03}$
1295027	$-0.76^{+0.30}_{-0.24}$	$0.73^{+0.19}_{-0.19}$	$1.60^{+0.16}_{-0.15}$	$-0.05^{+0.05}_{-0.08}$
1296321	$-1.62^{+0.20}_{-0.17}$	$0.49^{+0.34}_{-0.21}$	$1.18^{+0.22}_{-0.22}$	$-0.65^{+0.07}_{-0.07}$
1296657	$-1.28^{+0.22}_{-0.34}$	$0.03^{+0.18}_{-0.01}$	$1.98^{+0.07}_{-0.81}$	$-0.06^{+0.04}_{-0.22}$
1297026	$-1.00^{+0.00}_{-0.01}$	$5.11^{+0.02}_{-0.02}$	$0.83^{+0.01}_{-0.01}$	$-0.85^{+0.01}_{-0.01}$
1297465	$0.13^{+0.20}_{-0.16}$	$0.56^{+0.06}_{-0.05}$	$1.73^{+0.05}_{-0.04}$	$0.03^{+0.05}_{-0.06}$
1298281	$-1.41^{+0.54}_{-0.35}$	$3.49^{+0.25}_{-0.43}$	$0.45^{+0.13}_{-0.09}$	$-1.96^{+0.25}_{-0.17}$
1298893	$-0.86^{+0.06}_{-0.07}$	$4.53^{+0.05}_{-0.05}$	$0.61^{+0.03}_{-0.02}$	$-1.13^{+0.03}_{-0.03}$
1299643	$-0.96^{+0.69}_{-0.69}$	$0.45^{+0.32}_{-0.22}$	$2.13^{+0.19}_{-0.21}$	$-0.09^{+0.14}_{-0.22}$
1299775	$-1.72^{+0.02}_{-0.02}$	$1.37^{+0.24}_{-0.19}$	$2.25^{+0.09}_{-0.11}$	$-0.32^{+0.01}_{-0.01}$
1299785	$-0.44^{+0.20}_{-0.24}$	$1.70^{+0.14}_{-0.18}$	$0.80^{+0.09}_{-0.07}$	$-0.27^{+0.07}_{-0.07}$
1300516	$1.39^{+0.05}_{-0.37}$	$0.16^{+0.53}_{-0.04}$	$2.59^{+0.16}_{-0.42}$	$-0.48^{+0.20}_{-0.07}$

Table B.1: Continued from above.

SNID	$\mathrm{Log}(Z_\star/Z_\odot)$	t_{age} (Gyr)	τ_V	n
1300912	$0.03^{+0.67}_{-0.33}$	$0.79^{+0.37}_{-0.35}$	$0.88^{+0.11}_{-0.24}$	$-0.31^{+0.16}_{-0.13}$
1301933	$-0.58^{+0.23}_{-0.32}$	$0.71^{+0.07}_{-0.19}$	$1.54^{+0.17}_{-0.07}$	$-0.01^{+0.04}_{-0.08}$
1302058	$-1.87^{+0.21}_{-0.10}$	$0.25^{+0.21}_{-0.05}$	$1.97^{+0.11}_{-0.25}$	$-0.44^{+0.03}_{-0.05}$
1302187	$-1.74^{+0.30}_{-0.07}$	$0.41^{+0.51}_{-0.05}$	$2.38^{+0.05}_{-0.34}$	$-0.35^{+0.01}_{-0.00}$
1302523	$-1.70^{+0.89}_{-0.22}$	$0.09^{+0.49}_{-0.04}$	$2.48^{+0.38}_{-0.61}$	$-0.21^{+0.20}_{-0.05}$
1302648	$-1.94^{+0.09}_{-0.04}$	$2.94^{+0.19}_{-0.12}$	$1.03^{+0.04}_{-0.06}$	$-1.01^{+0.03}_{-0.03}$
1303279	$1.14^{+0.00}_{-0.01}$	$0.22^{+0.00}_{-0.00}$	$2.84^{+0.01}_{-0.01}$	$-0.15^{+0.00}_{-0.01}$
1303496	$-2.00^{+0.00}_{-0.00}$	$0.46^{+0.07}_{-0.02}$	$2.22^{+0.02}_{-0.08}$	$-0.46^{+0.01}_{-0.03}$
1303883	$0.03^{+0.08}_{-0.03}$	$3.06^{+0.07}_{-0.13}$	$1.02^{+0.03}_{-0.02}$	$-0.56^{+0.02}_{-0.02}$
1303952	$-0.25^{+0.00}_{-0.01}$	$2.01^{+0.10}_{-0.11}$	$1.11^{+0.06}_{-0.06}$	$-0.51^{+0.03}_{-0.04}$
1304442	$-0.14^{+0.08}_{-0.61}$	$0.43^{+0.03}_{-0.19}$	$1.29^{+0.43}_{-0.05}$	$0.31^{+0.02}_{-0.06}$
1304678	$1.26^{+0.01}_{-0.01}$	$0.70^{+0.01}_{-0.01}$	$2.14^{+0.01}_{-0.01}$	$-0.42^{+0.01}_{-0.01}$
1305504	$0.25^{+0.00}_{-0.01}$	$3.52^{+0.06}_{-0.69}$	$0.82^{+0.45}_{-0.03}$	$-1.03^{+0.43}_{-0.04}$
1305626	$-0.28^{+0.47}_{-0.38}$	$0.84^{+0.18}_{-0.26}$	$1.47^{+0.15}_{-0.14}$	$-0.05^{+0.07}_{-0.09}$
1306073	$-0.99^{+0.02}_{-0.01}$	$5.21^{+0.03}_{-0.03}$	$0.32^{+0.01}_{-0.01}$	$-1.87^{+0.04}_{-0.04}$
1306141	$0.70^{+0.25}_{-0.69}$	$0.31^{+0.21}_{-0.15}$	$1.36^{+0.17}_{-0.10}$	$-0.26^{+0.30}_{-0.08}$
1306360	$-0.75^{+0.01}_{-0.01}$	$0.89^{+0.04}_{-0.04}$	$1.84^{+0.04}_{-0.04}$	$-0.17^{+0.01}_{-0.01}$
1306390	$-1.25^{+0.26}_{-0.20}$	$1.59^{+0.34}_{-0.51}$	$1.58^{+0.22}_{-0.15}$	$-0.42^{+0.04}_{-0.04}$
1306537	$-0.09^{+0.59}_{-0.62}$	$0.29^{+0.30}_{-0.19}$	$2.92^{+0.46}_{-0.40}$	$0.05^{+0.08}_{-0.09}$
1306626	$-0.44^{+0.45}_{-0.39}$	$0.48^{+0.20}_{-0.20}$	$0.69^{+0.27}_{-0.23}$	$-0.22^{+0.18}_{-0.26}$
1306785	$-0.30^{+0.35}_{-0.26}$	$3.47^{+0.46}_{-0.68}$	$1.10^{+0.20}_{-0.16}$	$-0.91^{+0.14}_{-0.14}$
1306980	$-0.48^{+0.24}_{-0.16}$	$0.56^{+0.12}_{-0.16}$	$1.88^{+0.23}_{-0.14}$	$0.03^{+0.03}_{-0.03}$
1306991	$-0.74^{+0.04}_{-0.02}$	$2.06^{+0.06}_{-0.06}$	$1.18^{+0.03}_{-0.03}$	$-0.65^{+0.02}_{-0.02}$
1307277	$-0.82^{+0.37}_{-0.25}$	$0.89^{+0.15}_{-0.21}$	$1.91^{+0.12}_{-0.11}$	$-0.12^{+0.06}_{-0.07}$
1307830	$-0.75^{+0.00}_{-0.01}$	$7.10^{+0.01}_{-0.01}$	$0.25^{+0.00}_{-0.00}$	$-2.19^{+0.01}_{-0.00}$
1308326	$1.06^{+0.09}_{-0.37}$	$0.21^{+0.35}_{-0.07}$	$1.11^{+0.17}_{-0.33}$	$-0.56^{+0.06}_{-0.05}$
1308582	$-0.00^{+0.01}_{-0.75}$	$1.71^{+0.95}_{-0.07}$	$1.43^{+0.04}_{-0.35}$	$-0.49^{+0.02}_{-0.19}$
1308884	$-1.25^{+0.00}_{-0.00}$	$1.13^{+0.00}_{-0.01}$	$1.08^{+0.00}_{-0.00}$	$-0.48^{+0.00}_{-0.00}$
1309288	$-2.00^{+0.00}_{-0.00}$	$1.11^{+0.03}_{-0.03}$	$1.50^{+0.01}_{-0.02}$	$-0.71^{+0.01}_{-0.01}$
1309492	$0.85^{+0.15}_{-0.84}$	$0.20^{+0.26}_{-0.07}$	$1.86^{+0.16}_{-0.17}$	$-0.16^{+0.26}_{-0.06}$
1312274	$-0.70^{+0.35}_{-0.31}$	$0.68^{+0.17}_{-0.21}$	$2.88^{+0.18}_{-0.16}$	$0.01^{+0.04}_{-0.06}$
1313594	$-0.27^{+0.14}_{-0.22}$	$0.05^{+0.12}_{-0.04}$	$4.29^{+0.41}_{-0.78}$	$0.32^{+0.03}_{-0.10}$
1314897	$0.97^{+0.14}_{-0.96}$	$0.23^{+0.42}_{-0.10}$	$2.41^{+0.22}_{-0.16}$	$-0.25^{+0.25}_{-0.02}$
1315192	$-1.54^{+0.08}_{-0.08}$	$0.71^{+0.19}_{-0.12}$	$1.74^{+0.07}_{-0.11}$	$-0.44^{+0.01}_{-0.01}$
1315259	$-2.00^{+0.00}_{-0.00}$	$1.88^{+0.02}_{-0.02}$	$1.33^{+0.01}_{-0.01}$	$-0.78^{+0.00}_{-0.00}$
1315296	$-0.66^{+0.36}_{-0.09}$	$0.46^{+0.11}_{-0.09}$	$1.02^{+0.14}_{-0.15}$	$-0.12^{+0.05}_{-0.05}$

Table B.1: Continued from above.

SNID	$\mathrm{Log}(Z_\star/Z_\odot)$	t_{age} (Gyr)	τ_V	n
1316385	$1.38^{+0.01}_{-0.01}$	$0.55^{+0.01}_{-0.01}$	$1.75^{+0.01}_{-0.01}$	$-0.63^{+0.01}_{-0.01}$
1316431	$-0.56^{+0.88}_{-0.62}$	$0.25^{+0.15}_{-0.16}$	$0.29^{+0.35}_{-0.20}$	$-0.90^{+0.85}_{-0.87}$
1316437	$-0.33^{+0.40}_{-0.32}$	$0.57^{+0.15}_{-0.18}$	$0.56^{+0.18}_{-0.15}$	$-0.31^{+0.15}_{-0.15}$
1316465	$-0.59^{+0.28}_{-0.33}$	$0.68^{+0.11}_{-0.20}$	$1.10^{+0.19}_{-0.11}$	$-0.11^{+0.08}_{-0.11}$
1317164	$-2.00^{+0.00}_{-0.00}$	$8.56^{+0.04}_{-0.04}$	$0.96^{+0.01}_{-0.01}$	$-1.41^{+0.01}_{-0.01}$
1317277	$0.22^{+0.35}_{-0.53}$	$2.69^{+0.75}_{-0.42}$	$0.67^{+0.05}_{-0.13}$	$-1.44^{+0.06}_{-0.06}$
1317286	$-0.02^{+0.81}_{-0.92}$	$0.74^{+0.34}_{-0.40}$	$0.25^{+0.33}_{-0.17}$	$-0.68^{+0.75}_{-0.90}$
1317666	$-1.99^{+0.23}_{-0.00}$	$0.30^{+0.18}_{-0.01}$	$1.97^{+0.02}_{-0.19}$	$-0.47^{+0.01}_{-0.05}$
1319366	$-1.60^{+0.40}_{-0.30}$	$0.13^{+0.37}_{-0.06}$	$1.71^{+0.26}_{-0.53}$	$-0.34^{+0.08}_{-0.11}$
1319821	$0.13^{+0.40}_{-0.37}$	$0.29^{+0.05}_{-0.06}$	$1.78^{+0.13}_{-0.04}$	$0.14^{+0.06}_{-0.15}$
1322229	$-0.11^{+0.32}_{-0.23}$	$0.31^{+0.12}_{-0.08}$	$1.82^{+0.14}_{-0.17}$	$0.16^{+0.04}_{-0.05}$
1322979	$1.01^{+0.51}_{-2.10}$	$0.50^{+0.63}_{-0.32}$	$0.47^{+0.28}_{-0.19}$	$-1.70^{+0.52}_{-0.36}$
1324542	$-0.25^{+0.79}_{-0.64}$	$0.14^{+0.54}_{-0.13}$	$2.14^{+0.93}_{-0.97}$	$0.08^{+0.16}_{-0.16}$
1327978	$1.49^{+0.01}_{-0.02}$	$2.08^{+0.04}_{-0.02}$	$0.71^{+0.00}_{-0.01}$	$-1.74^{+0.02}_{-0.02}$
1328066	$-0.11^{+0.48}_{-0.34}$	$1.70^{+0.51}_{-0.59}$	$0.97^{+0.25}_{-0.21}$	$-0.75^{+0.14}_{-0.18}$
1328105	$-0.36^{+0.23}_{-0.38}$	$0.53^{+0.11}_{-0.11}$	$2.06^{+0.16}_{-0.12}$	$0.03^{+0.03}_{-0.02}$
1329312	$-0.74^{+0.02}_{-0.01}$	$1.76^{+0.04}_{-0.04}$	$1.64^{+0.02}_{-0.02}$	$-0.21^{+0.01}_{-0.01}$
1329615	$-0.39^{+0.12}_{-0.09}$	$4.42^{+0.13}_{-0.14}$	$0.59^{+0.03}_{-0.03}$	$-0.92^{+0.05}_{-0.05}$
1330031	$-1.99^{+0.31}_{-0.01}$	$0.39^{+0.55}_{-0.04}$	$1.48^{+0.05}_{-0.39}$	$-0.65^{+0.04}_{-0.16}$
1330426	$-0.14^{+1.00}_{-0.96}$	$1.21^{+0.60}_{-0.65}$	$0.41^{+0.40}_{-0.22}$	$-1.05^{+0.81}_{-0.75}$
1331123	$0.01^{+0.02}_{-0.01}$	$4.56^{+0.03}_{-0.05}$	$0.61^{+0.01}_{-0.01}$	$-1.08^{+0.02}_{-0.01}$
1333246	$-0.68^{+0.18}_{-0.20}$	$0.96^{+0.10}_{-0.14}$	$1.72^{+0.10}_{-0.09}$	$-0.12^{+0.02}_{-0.04}$
1334084	$-1.60^{+0.20}_{-0.14}$	$0.19^{+0.36}_{-0.09}$	$2.09^{+0.27}_{-0.47}$	$-0.29^{+0.07}_{-0.09}$
1334087	$-1.15^{+0.14}_{-0.15}$	$4.46^{+0.06}_{-0.08}$	$0.51^{+0.03}_{-0.03}$	$-1.64^{+0.03}_{-0.03}$
1334302	$-1.39^{+0.22}_{-0.32}$	$0.23^{+0.13}_{-0.06}$	$2.85^{+0.08}_{-0.18}$	$-0.19^{+0.07}_{-0.06}$
1334423	$0.76^{+0.12}_{-0.72}$	$0.17^{+0.24}_{-0.05}$	$0.96^{+0.12}_{-0.21}$	$-0.36^{+0.17}_{-0.07}$
1334448	$1.52^{+0.08}_{-0.20}$	$0.33^{+1.40}_{-0.18}$	$2.55^{+0.47}_{-1.53}$	$-0.82^{+0.13}_{-0.60}$
1334597	$-1.32^{+0.70}_{-0.49}$	$2.96^{+0.45}_{-0.77}$	$0.53^{+0.27}_{-0.17}$	$-1.43^{+0.34}_{-0.39}$
1334620	$-2.00^{+0.01}_{-0.00}$	$0.45^{+0.03}_{-0.02}$	$1.62^{+0.02}_{-0.04}$	$-0.65^{+0.01}_{-0.02}$
1334644	$-1.00^{+0.01}_{-0.01}$	$7.90^{+0.01}_{-0.01}$	$0.22^{+0.00}_{-0.00}$	$-2.19^{+0.01}_{-0.00}$
1334645	$-1.96^{+0.81}_{-0.04}$	$2.50^{+1.26}_{-0.17}$	$0.91^{+0.06}_{-0.41}$	$-1.12^{+0.06}_{-0.31}$
1335717	$0.77^{+0.07}_{-0.12}$	$0.32^{+0.06}_{-0.04}$	$1.45^{+0.04}_{-0.04}$	$-0.25^{+0.04}_{-0.04}$
1336008	$-0.53^{+0.24}_{-0.14}$	$0.29^{+0.09}_{-0.10}$	$2.37^{+0.26}_{-0.18}$	$0.17^{+0.03}_{-0.03}$
1336009	$0.88^{+0.21}_{-1.03}$	$0.24^{+0.46}_{-0.13}$	$1.67^{+0.30}_{-0.31}$	$-0.25^{+0.16}_{-0.07}$
1336453	$-1.37^{+0.13}_{-0.08}$	$0.37^{+0.20}_{-0.11}$	$0.88^{+0.13}_{-0.18}$	$-0.66^{+0.07}_{-0.09}$
1336480	$-1.97^{+0.34}_{-0.02}$	$0.21^{+0.20}_{-0.02}$	$1.73^{+0.05}_{-0.26}$	$-0.46^{+0.02}_{-0.04}$

Table B.1: Continued from above.

SNID	$\mathrm{Log}(Z_\star/Z_\odot)$	t_{age} (Gyr)	τ_V	n
1336687	$-0.37^{+0.44}_{-0.41}$	$1.13^{+0.16}_{-0.28}$	$0.20^{+0.16}_{-0.10}$	$-0.87^{+0.48}_{-0.61}$
1337117	$-0.70^{+0.74}_{-0.67}$	$0.48^{+0.60}_{-0.40}$	$0.94^{+0.98}_{-0.54}$	$-0.30^{+0.32}_{-0.54}$
1337228	$-0.90^{+0.35}_{-0.39}$	$0.17^{+0.74}_{-0.11}$	$2.14^{+0.49}_{-0.95}$	$-0.06^{+0.13}_{-0.18}$
1337272	$-0.25^{+0.56}_{-0.40}$	$0.14^{+0.24}_{-0.10}$	$1.35^{+0.70}_{-0.58}$	$0.01^{+0.21}_{-0.32}$
1337649	$-0.03^{+0.60}_{-0.78}$	$1.76^{+0.36}_{-0.54}$	$0.25^{+0.14}_{-0.09}$	$-1.50^{+0.47}_{-0.44}$
1337687	$-0.09^{+0.62}_{-0.56}$	$0.69^{+0.31}_{-0.29}$	$0.41^{+0.26}_{-0.22}$	$-0.57^{+0.43}_{-0.57}$
1337703	$-0.25^{+0.02}_{-0.03}$	$1.88^{+0.12}_{-0.12}$	$1.12^{+0.07}_{-0.06}$	$-0.75^{+0.05}_{-0.05}$
1337838	$-0.41^{+0.87}_{-0.87}$	$1.14^{+0.58}_{-0.59}$	$0.44^{+0.45}_{-0.25}$	$-0.88^{+0.72}_{-0.80}$
1338128	$0.83^{+0.14}_{-0.25}$	$0.22^{+0.11}_{-0.06}$	$1.07^{+0.12}_{-0.12}$	$-0.45^{+0.12}_{-0.09}$
1338170	$1.00^{+0.05}_{-0.07}$	$0.70^{+0.18}_{-0.17}$	$1.37^{+0.15}_{-0.14}$	$-0.67^{+0.04}_{-0.05}$
1338278	$-0.28^{+0.27}_{-0.22}$	$1.98^{+0.45}_{-0.60}$	$0.65^{+0.30}_{-0.22}$	$-0.49^{+0.18}_{-0.28}$
1338430	$0.24^{+0.05}_{-0.41}$	$0.73^{+0.48}_{-0.07}$	$2.08^{+0.07}_{-0.27}$	$-0.19^{+0.02}_{-0.03}$
1338471	$-0.86^{+0.24}_{-0.28}$	$0.67^{+0.31}_{-0.26}$	$1.71^{+0.21}_{-0.26}$	$-0.14^{+0.05}_{-0.08}$
1338675	$0.42^{+0.21}_{-0.43}$	$0.18^{+0.05}_{-0.05}$	$1.63^{+0.09}_{-0.10}$	$0.01^{+0.17}_{-0.08}$
1339002	$-1.00^{+0.03}_{-0.03}$	$4.21^{+0.06}_{-0.06}$	$0.69^{+0.02}_{-0.02}$	$-0.86^{+0.03}_{-0.03}$
1339149	$0.32^{+0.22}_{-0.22}$	$0.26^{+0.06}_{-0.08}$	$1.47^{+0.11}_{-0.10}$	$-0.13^{+0.07}_{-0.05}$
1339392	$-2.00^{+0.00}_{-0.00}$	$1.71^{+0.05}_{-0.05}$	$1.26^{+0.02}_{-0.02}$	$-1.02^{+0.01}_{-0.01}$
1339450	$-0.25^{+0.00}_{-0.01}$	$1.81^{+0.13}_{-0.10}$	$1.06^{+0.06}_{-0.07}$	$-0.42^{+0.03}_{-0.04}$
1340454	$-0.37^{+0.33}_{-0.31}$	$0.50^{+0.11}_{-0.15}$	$2.05^{+0.17}_{-0.13}$	$0.09^{+0.03}_{-0.04}$
1341370	$-0.03^{+0.81}_{-0.89}$	$1.35^{+0.51}_{-0.63}$	$0.38^{+0.34}_{-0.19}$	$-1.08^{+0.50}_{-0.64}$
1341894	$-1.65^{+0.28}_{-0.17}$	$0.41^{+0.35}_{-0.10}$	$1.77^{+0.12}_{-0.22}$	$-0.44^{+0.05}_{-0.04}$
1342255	$-1.79^{+0.29}_{-0.17}$	$0.38^{+0.38}_{-0.12}$	$1.67^{+0.16}_{-0.26}$	$-0.53^{+0.04}_{-0.04}$
1343208	$-0.25^{+0.02}_{-0.02}$	$1.60^{+0.14}_{-0.17}$	$1.37^{+0.11}_{-0.08}$	$-0.36^{+0.04}_{-0.04}$
1343337	$-0.04^{+0.18}_{-0.34}$	$0.25^{+0.10}_{-0.04}$	$1.81^{+0.10}_{-0.15}$	$0.18^{+0.04}_{-0.10}$
1343401	$-2.00^{+0.01}_{-0.00}$	$0.74^{+0.05}_{-0.04}$	$2.32^{+0.03}_{-0.03}$	$-0.42^{+0.01}_{-0.01}$
1343533	$-0.04^{+0.15}_{-0.19}$	$1.52^{+0.52}_{-0.19}$	$1.56^{+0.08}_{-0.26}$	$-0.28^{+0.03}_{-0.06}$
1343759	$-0.52^{+0.10}_{-0.07}$	$0.21^{+0.08}_{-0.08}$	$1.38^{+0.28}_{-0.22}$	$0.08^{+0.05}_{-0.07}$
1344692	$1.17^{+0.73}_{-0.92}$	$0.52^{+1.90}_{-0.48}$	$1.61^{+1.35}_{-0.87}$	$-0.85^{+0.32}_{-0.43}$
1345553	$-1.55^{+0.56}_{-0.36}$	$3.64^{+0.70}_{-0.87}$	$0.95^{+0.29}_{-0.25}$	$-0.70^{+0.09}_{-0.12}$
1345594	$-0.27^{+0.03}_{-0.07}$	$2.21^{+0.13}_{-0.15}$	$1.42^{+0.08}_{-0.06}$	$-0.27^{+0.03}_{-0.03}$
1346137	$-0.51^{+0.42}_{-0.15}$	$0.19^{+0.09}_{-0.07}$	$2.02^{+0.30}_{-0.25}$	$0.18^{+0.04}_{-0.03}$
1346387	$0.63^{+1.58}_{-1.30}$	$1.81^{+0.92}_{-1.77}$	$0.56^{+1.71}_{-0.17}$	$-1.69^{+0.56}_{-0.39}$
1346956	$-0.36^{+0.86}_{-0.76}$	$0.46^{+0.26}_{-0.26}$	$0.31^{+0.41}_{-0.21}$	$-0.62^{+0.69}_{-0.97}$
1346966	$0.07^{+0.70}_{-0.11}$	$0.33^{+0.06}_{-0.16}$	$1.24^{+0.09}_{-0.10}$	$0.02^{+0.08}_{-0.30}$

Table B.2: *Best-fit* results for the DES host galaxies fits with DECam *griz* global photometry.

SNID	$\mathrm{Log}(Z_\star/Z_\odot)$	t_{age} (Gyr)	τ_V	n
1248677	$-0.20^{+0.64}_{-0.54}$	$0.10^{+0.17}_{-0.08}$	$1.41^{+0.71}_{-0.58}$	$0.06^{+0.20}_{-0.34}$
1250017	$-1.26^{+0.57}_{-0.57}$	$0.11^{+0.74}_{-0.09}$	$1.48^{+0.75}_{-0.89}$	$-0.29^{+0.24}_{-0.44}$
1253039	$-0.59^{+0.70}_{-0.77}$	$0.58^{+1.44}_{-0.49}$	$1.60^{+1.28}_{-1.01}$	$-0.09^{+0.28}_{-0.50}$
1253101	$-0.36^{+0.57}_{-0.52}$	$0.15^{+0.19}_{-0.12}$	$1.11^{+0.68}_{-0.46}$	$-0.05^{+0.27}_{-0.39}$
1253920	$-1.48^{+0.55}_{-0.36}$	$2.96^{+0.60}_{-1.05}$	$0.70^{+0.41}_{-0.23}$	$-1.29^{+0.43}_{-0.49}$
1255502	$-0.90^{+0.68}_{-0.64}$	$0.55^{+1.27}_{-0.53}$	$2.28^{+1.42}_{-1.00}$	$0.02^{+0.19}_{-0.37}$
1257366	$-1.29^{+0.81}_{-0.53}$	$1.50^{+0.90}_{-1.24}$	$0.90^{+0.87}_{-0.43}$	$-0.55^{+0.21}_{-0.41}$
1257695	$-0.61^{+0.42}_{-0.43}$	$1.10^{+0.33}_{-0.40}$	$0.49^{+0.33}_{-0.22}$	$-0.71^{+0.41}_{-0.56}$
1258906	$-0.35^{+0.65}_{-0.50}$	$0.53^{+0.34}_{-0.25}$	$1.25^{+0.32}_{-0.34}$	$-0.11^{+0.17}_{-0.24}$
1258940	$-0.85^{+0.81}_{-0.65}$	$1.74^{+0.52}_{-0.64}$	$0.49^{+0.30}_{-0.22}$	$-0.99^{+0.34}_{-0.47}$
1259412	$0.20^{+0.70}_{-0.72}$	$0.23^{+0.31}_{-0.19}$	$1.62^{+0.95}_{-0.49}$	$0.03^{+0.19}_{-0.31}$
1261579	$-0.54^{+0.80}_{-0.67}$	$1.25^{+0.97}_{-0.65}$	$1.64^{+0.49}_{-0.51}$	$-0.28^{+0.17}_{-0.21}$
1263369	$0.26^{+0.53}_{-0.58}$	$0.44^{+0.32}_{-0.19}$	$1.92^{+0.22}_{-0.27}$	$-0.10^{+0.12}_{-0.14}$
1263715	$-0.51^{+0.59}_{-0.52}$	$0.85^{+0.33}_{-0.33}$	$0.64^{+0.31}_{-0.24}$	$-0.61^{+0.37}_{-0.44}$
1275946	$-0.62^{+0.55}_{-0.53}$	$0.56^{+0.26}_{-0.31}$	$0.48^{+0.45}_{-0.24}$	$-0.68^{+0.57}_{-0.75}$
1279500	$-0.40^{+0.98}_{-0.98}$	$2.17^{+0.54}_{-0.70}$	$0.41^{+0.23}_{-0.14}$	$-1.47^{+0.54}_{-0.50}$
1280217	$1.05^{+0.30}_{-1.15}$	$0.46^{+0.70}_{-0.27}$	$0.37^{+0.23}_{-0.19}$	$-1.75^{+0.56}_{-0.33}$
1281668	$-0.24^{+0.71}_{-0.45}$	$0.30^{+0.32}_{-0.21}$	$1.96^{+0.67}_{-0.43}$	$0.09^{+0.14}_{-0.15}$
1281886	$-0.53^{+0.68}_{-0.66}$	$1.05^{+0.74}_{-0.47}$	$1.17^{+0.38}_{-0.43}$	$-0.26^{+0.18}_{-0.27}$
1282736	$-0.62^{+0.64}_{-0.66}$	$0.80^{+0.66}_{-0.40}$	$1.86^{+0.38}_{-0.46}$	$-0.16^{+0.12}_{-0.20}$
1282757	$-1.00^{+0.64}_{-0.62}$	$0.56^{+0.54}_{-0.39}$	$0.98^{+0.49}_{-0.41}$	$-0.50^{+0.29}_{-0.33}$
1283373	$-0.16^{+0.97}_{-0.74}$	$3.98^{+0.85}_{-1.23}$	$0.62^{+0.21}_{-0.17}$	$-1.28^{+0.36}_{-0.45}$
1283878	$-1.02^{+1.79}_{-0.75}$	$3.35^{+0.49}_{-1.35}$	$0.51^{+0.23}_{-0.11}$	$-1.88^{+0.41}_{-0.23}$
1283936	$-0.32^{+0.66}_{-0.57}$	$0.47^{+0.31}_{-0.21}$	$1.56^{+0.33}_{-0.31}$	$-0.05^{+0.12}_{-0.16}$
1284587	$-0.36^{+0.87}_{-0.74}$	$2.00^{+0.85}_{-0.82}$	$0.80^{+0.48}_{-0.32}$	$-0.73^{+0.42}_{-0.64}$
1285317	$-1.51^{+0.56}_{-0.32}$	$0.27^{+0.14}_{-0.08}$	$0.22^{+0.15}_{-0.06}$	$-1.75^{+0.75}_{-0.32}$
1286398	$0.65^{+0.91}_{-0.83}$	$2.12^{+1.36}_{-1.04}$	$0.91^{+0.46}_{-0.33}$	$-1.04^{+0.58}_{-0.72}$
1287626	$2.26^{+0.17}_{-0.74}$	$0.04^{+0.12}_{-0.01}$	$0.93^{+0.08}_{-0.40}$	$-2.07^{+0.19}_{-0.09}$
1289288	$-1.19^{+0.79}_{-0.51}$	$0.56^{+0.70}_{-0.47}$	$2.05^{+0.82}_{-0.54}$	$-0.22^{+0.16}_{-0.18}$
1289555	$-0.71^{+0.79}_{-0.52}$	$0.74^{+0.22}_{-0.34}$	$0.23^{+0.29}_{-0.14}$	$-0.98^{+0.49}_{-0.66}$
1289600	$-0.42^{+0.38}_{-0.34}$	$0.39^{+0.18}_{-0.15}$	$0.81^{+0.28}_{-0.26}$	$-0.15^{+0.18}_{-0.26}$
1289656	$-0.19^{+0.57}_{-0.53}$	$0.46^{+0.39}_{-0.30}$	$0.66^{+0.60}_{-0.40}$	$-0.31^{+0.37}_{-0.58}$
1289664	$-0.54^{+0.89}_{-0.49}$	$0.20^{+0.38}_{-0.17}$	$0.95^{+0.94}_{-0.63}$	$0.08^{+0.24}_{-0.49}$
1290816	$-0.57^{+0.63}_{-0.58}$	$0.85^{+0.55}_{-0.47}$	$0.76^{+0.54}_{-0.39}$	$-0.48^{+0.44}_{-0.70}$
1291080	$0.63^{+0.69}_{-1.48}$	$1.47^{+1.01}_{-0.80}$	$0.51^{+0.33}_{-0.19}$	$-1.64^{+0.54}_{-0.40}$
1291090	$-0.11^{+0.58}_{-0.58}$	$0.56^{+0.26}_{-0.22}$	$0.85^{+0.25}_{-0.22}$	$-0.33^{+0.22}_{-0.27}$

Table B.2: Continued from above.

SNID	$\mathrm{Log}(Z_\star/Z_\odot)$	t_{age} (Gyr)	τ_V	n
1291794	$-1.24^{+0.76}_{-0.49}$	$0.48^{+0.61}_{-0.30}$	$2.24^{+0.42}_{-0.45}$	$-0.20^{+0.18}_{-0.14}$
1292145	$-0.33^{+0.59}_{-0.58}$	$0.42^{+0.39}_{-0.23}$	$1.29^{+0.43}_{-0.44}$	$-0.18^{+0.17}_{-0.25}$
1292332	$-0.64^{+1.13}_{-0.85}$	$3.40^{+0.96}_{-1.21}$	$0.80^{+0.37}_{-0.27}$	$-1.03^{+0.33}_{-0.43}$
1292336	$-1.29^{+0.74}_{-0.54}$	$1.09^{+0.90}_{-0.86}$	$1.09^{+0.71}_{-0.46}$	$-0.51^{+0.22}_{-0.29}$
1292560	$-0.66^{+0.57}_{-0.59}$	$1.07^{+0.40}_{-0.47}$	$0.49^{+0.37}_{-0.23}$	$-0.83^{+0.53}_{-0.69}$
1293319	$-1.17^{+1.05}_{-0.56}$	$1.63^{+0.49}_{-0.59}$	$0.47^{+0.29}_{-0.17}$	$-1.43^{+0.52}_{-0.48}$
1293758	$-0.06^{+0.75}_{-0.63}$	$1.05^{+0.86}_{-0.45}$	$1.49^{+0.55}_{-0.47}$	$-0.11^{+0.29}_{-0.41}$
1294014	$-0.42^{+0.59}_{-0.59}$	$0.93^{+0.36}_{-0.35}$	$0.43^{+0.27}_{-0.22}$	$-0.67^{+0.42}_{-0.56}$
1294743	$-0.19^{+0.92}_{-0.97}$	$2.00^{+0.78}_{-0.88}$	$0.54^{+0.39}_{-0.24}$	$-1.02^{+0.52}_{-0.65}$
1295027	$-0.52^{+0.61}_{-0.63}$	$0.58^{+0.51}_{-0.30}$	$1.61^{+0.37}_{-0.44}$	$-0.05^{+0.11}_{-0.23}$
1296321	$-0.98^{+0.60}_{-0.40}$	$0.51^{+0.73}_{-0.46}$	$1.20^{+1.20}_{-0.61}$	$-0.26^{+0.34}_{-0.44}$
1296657	$-0.67^{+0.45}_{-0.30}$	$0.20^{+0.30}_{-0.18}$	$1.13^{+0.79}_{-0.65}$	$0.09^{+0.21}_{-0.38}$
1297026	$0.16^{+1.75}_{-1.01}$	$6.51^{+4.51}_{-6.18}$	$0.66^{+1.46}_{-0.33}$	$-1.87^{+0.51}_{-0.25}$
1297465	$-0.99^{+0.60}_{-0.61}$	$1.81^{+0.64}_{-0.73}$	$0.61^{+0.39}_{-0.29}$	$-0.91^{+0.44}_{-0.63}$
1298281	$-0.52^{+1.07}_{-0.89}$	$2.84^{+0.76}_{-1.05}$	$0.68^{+0.35}_{-0.22}$	$-1.20^{+0.46}_{-0.53}$
1298893	$-0.45^{+0.98}_{-0.79}$	$2.71^{+1.05}_{-0.97}$	$1.20^{+0.43}_{-0.37}$	$-0.53^{+0.20}_{-0.31}$
1299643	$-0.27^{+0.72}_{-0.54}$	$0.49^{+0.40}_{-0.24}$	$1.91^{+0.39}_{-0.38}$	$-0.05^{+0.12}_{-0.15}$
1299775	$-0.01^{+1.04}_{-0.93}$	$2.62^{+1.34}_{-1.10}$	$1.58^{+0.56}_{-0.49}$	$-0.45^{+0.22}_{-0.40}$
1299785	$-0.49^{+0.69}_{-0.61}$	$1.38^{+0.47}_{-0.55}$	$0.45^{+0.35}_{-0.23}$	$-0.77^{+0.41}_{-0.63}$
1300516	$-0.84^{+0.72}_{-0.67}$	$1.85^{+0.99}_{-0.91}$	$1.37^{+0.52}_{-0.45}$	$-0.41^{+0.20}_{-0.22}$
1300912	$0.19^{+0.75}_{-0.85}$	$1.00^{+0.75}_{-0.56}$	$0.61^{+0.45}_{-0.32}$	$-0.68^{+0.45}_{-0.63}$
1302058	$-0.53^{+0.77}_{-0.71}$	$1.40^{+0.82}_{-0.68}$	$1.01^{+0.51}_{-0.43}$	$-0.47^{+0.32}_{-0.48}$
1302187	$-1.82^{+0.32}_{-0.13}$	$11.21^{+0.70}_{-0.69}$	$0.54^{+0.06}_{-0.05}$	$-2.05^{+0.20}_{-0.11}$
1302523	$-0.53^{+0.57}_{-0.48}$	$0.54^{+0.37}_{-0.25}$	$1.98^{+0.37}_{-0.38}$	$-0.05^{+0.10}_{-0.14}$
1302648	$-0.17^{+0.99}_{-1.09}$	$3.36^{+0.96}_{-1.18}$	$0.70^{+0.32}_{-0.23}$	$-1.20^{+0.38}_{-0.46}$
1303279	$-1.46^{+0.53}_{-0.40}$	$5.10^{+1.50}_{-1.90}$	$1.12^{+0.62}_{-0.39}$	$-0.89^{+0.34}_{-0.48}$
1303496	$-0.63^{+0.70}_{-0.58}$	$1.56^{+1.11}_{-0.85}$	$1.71^{+0.63}_{-0.56}$	$-0.31^{+0.20}_{-0.26}$
1303883	$0.08^{+0.83}_{-0.83}$	$1.85^{+0.96}_{-0.79}$	$1.15^{+0.38}_{-0.33}$	$-0.56^{+0.21}_{-0.27}$
1303952	$-0.96^{+1.47}_{-0.76}$	$2.74^{+0.77}_{-1.17}$	$0.57^{+0.41}_{-0.19}$	$-1.53^{+0.52}_{-0.46}$
1304442	$-0.10^{+0.73}_{-0.65}$	$1.34^{+0.39}_{-0.52}$	$0.31^{+0.26}_{-0.14}$	$-1.18^{+0.68}_{-0.68}$
1304678	$-1.27^{+0.72}_{-0.54}$	$5.24^{+1.70}_{-1.85}$	$1.11^{+0.57}_{-0.39}$	$-0.74^{+0.27}_{-0.42}$
1305504	$-0.56^{+1.34}_{-1.04}$	$2.88^{+0.90}_{-1.18}$	$0.55^{+0.37}_{-0.18}$	$-1.56^{+0.47}_{-0.43}$
1305626	$-0.47^{+0.91}_{-0.88}$	$2.11^{+0.60}_{-0.74}$	$0.45^{+0.30}_{-0.20}$	$-1.09^{+0.47}_{-0.63}$
1306073	$-1.07^{+0.84}_{-0.68}$	$6.84^{+0.98}_{-1.40}$	$0.38^{+0.23}_{-0.12}$	$-1.56^{+0.54}_{-0.44}$
1306141	$-0.61^{+0.73}_{-0.77}$	$1.57^{+0.44}_{-0.56}$	$0.39^{+0.31}_{-0.18}$	$-1.03^{+0.48}_{-0.61}$
1306360	$-0.57^{+0.58}_{-0.57}$	$1.32^{+0.63}_{-0.51}$	$1.40^{+0.32}_{-0.34}$	$-0.39^{+0.11}_{-0.16}$

Table B.2: Continued from above.

SNID	$\mathrm{Log}(Z_\star/Z_\odot)$	t_{age} (Gyr)	τ_V	n
1306390	$-0.87^{+0.67}_{-0.60}$	$1.88^{+0.85}_{-0.77}$	$1.50^{+0.39}_{-0.39}$	$-0.41^{+0.14}_{-0.12}$
1306537	$-0.41^{+0.62}_{-0.76}$	$1.16^{+1.22}_{-0.68}$	$1.43^{+0.62}_{-0.66}$	$-0.28^{+0.22}_{-0.28}$
1306626	$-0.42^{+0.61}_{-0.55}$	$1.07^{+0.31}_{-0.36}$	$0.35^{+0.23}_{-0.17}$	$-0.83^{+0.40}_{-0.54}$
1306785	$-0.43^{+0.81}_{-0.80}$	$1.68^{+1.28}_{-1.00}$	$1.31^{+0.69}_{-0.56}$	$-0.59^{+0.23}_{-0.36}$
1306980	$-0.26^{+0.53}_{-0.38}$	$0.42^{+0.40}_{-0.21}$	$2.07^{+0.37}_{-0.45}$	$0.01^{+0.07}_{-0.11}$
1306991	$-0.67^{+0.75}_{-0.70}$	$2.00^{+0.83}_{-0.76}$	$1.16^{+0.36}_{-0.35}$	$-0.79^{+0.19}_{-0.26}$
1307277	$-0.53^{+0.81}_{-0.71}$	$1.22^{+1.00}_{-0.64}$	$1.46^{+0.52}_{-0.56}$	$-0.28^{+0.18}_{-0.25}$
1307830	$0.01^{+0.95}_{-0.92}$	$2.48^{+0.87}_{-1.07}$	$0.77^{+0.29}_{-0.22}$	$-1.26^{+0.31}_{-0.36}$
1308326	$-0.56^{+0.66}_{-0.70}$	$1.21^{+0.36}_{-0.46}$	$0.35^{+0.27}_{-0.18}$	$-0.98^{+0.52}_{-0.64}$
1308582	$1.40^{+0.19}_{-0.94}$	$1.24^{+1.27}_{-0.39}$	$0.69^{+0.24}_{-0.18}$	$-1.77^{+0.35}_{-0.29}$
1308884	$-0.62^{+0.42}_{-0.51}$	$2.18^{+0.21}_{-0.46}$	$0.26^{+0.21}_{-0.09}$	$-1.27^{+0.65}_{-0.63}$
1309288	$-0.60^{+0.41}_{-0.50}$	$0.09^{+1.96}_{-0.07}$	$3.71^{+0.84}_{-2.10}$	$-0.01^{+0.18}_{-0.37}$
1309492	$0.44^{+0.54}_{-0.66}$	$0.74^{+0.75}_{-0.42}$	$1.23^{+0.50}_{-0.49}$	$-0.32^{+0.23}_{-0.32}$
1312274	$-0.35^{+0.68}_{-0.62}$	$0.67^{+0.54}_{-0.30}$	$2.60^{+0.33}_{-0.42}$	$-0.07^{+0.07}_{-0.10}$
1313594	$-0.55^{+0.68}_{-0.63}$	$0.29^{+0.57}_{-0.22}$	$2.17^{+0.96}_{-0.76}$	$-0.01^{+0.22}_{-0.29}$
1314897	$0.88^{+0.43}_{-1.03}$	$0.98^{+1.02}_{-0.51}$	$0.94^{+0.43}_{-0.37}$	$-0.81^{+0.36}_{-0.44}$
1315192	$-0.97^{+0.58}_{-0.59}$	$1.21^{+0.78}_{-0.79}$	$1.15^{+0.54}_{-0.43}$	$-0.44^{+0.20}_{-0.26}$
1315259	$-0.91^{+0.87}_{-0.72}$	$2.83^{+0.66}_{-0.93}$	$0.66^{+0.37}_{-0.23}$	$-1.03^{+0.34}_{-0.44}$
1315296	$-0.38^{+0.46}_{-0.37}$	$0.31^{+0.18}_{-0.13}$	$1.13^{+0.32}_{-0.27}$	$-0.04^{+0.13}_{-0.18}$
1316385	$-0.15^{+0.92}_{-0.85}$	$2.51^{+0.86}_{-0.90}$	$0.63^{+0.32}_{-0.22}$	$-1.22^{+0.53}_{-0.59}$
1316431	$1.10^{+0.31}_{-0.34}$	$0.15^{+0.18}_{-0.08}$	$0.38^{+0.35}_{-0.25}$	$-0.67^{+0.75}_{-0.93}$
1316437	$1.10^{+0.33}_{-1.77}$	$0.36^{+0.50}_{-0.19}$	$0.30^{+0.19}_{-0.15}$	$-1.65^{+0.67}_{-0.39}$
1316465	$-0.49^{+0.54}_{-0.55}$	$0.76^{+0.37}_{-0.32}$	$0.49^{+0.35}_{-0.27}$	$-0.51^{+0.45}_{-0.63}$
1317164	$-0.14^{+1.07}_{-1.02}$	$3.94^{+1.49}_{-1.46}$	$0.74^{+0.45}_{-0.28}$	$-1.03^{+0.50}_{-0.68}$
1317277	$-0.40^{+1.02}_{-0.91}$	$3.76^{+0.94}_{-1.19}$	$0.70^{+0.32}_{-0.23}$	$-1.17^{+0.35}_{-0.45}$
1317286	$0.23^{+0.56}_{-1.02}$	$0.40^{+0.21}_{-0.21}$	$0.20^{+0.32}_{-0.15}$	$-0.37^{+0.55}_{-0.98}$
1317666	$0.02^{+0.91}_{-0.85}$	$2.01^{+0.84}_{-0.81}$	$0.56^{+0.33}_{-0.22}$	$-1.06^{+0.62}_{-0.68}$
1319366	$-0.86^{+0.61}_{-0.57}$	$0.47^{+0.44}_{-0.40}$	$1.08^{+0.85}_{-0.42}$	$-0.24^{+0.22}_{-0.33}$
1319821	$-0.05^{+0.80}_{-0.73}$	$1.28^{+0.82}_{-0.62}$	$0.80^{+0.46}_{-0.35}$	$-0.50^{+0.34}_{-0.48}$
1322229	$-0.46^{+0.72}_{-0.63}$	$0.90^{+0.48}_{-0.42}$	$0.64^{+0.38}_{-0.31}$	$-0.50^{+0.27}_{-0.39}$
1322979	$-1.15^{+1.79}_{-0.61}$	$0.68^{+0.34}_{-0.28}$	$0.27^{+0.17}_{-0.11}$	$-1.67^{+0.57}_{-0.38}$
1324542	$-0.36^{+0.82}_{-0.74}$	$0.55^{+0.23}_{-0.28}$	$0.22^{+0.30}_{-0.14}$	$-0.86^{+0.71}_{-0.78}$
1327978	$0.86^{+0.77}_{-1.07}$	$2.80^{+1.70}_{-1.55}$	$0.89^{+0.44}_{-0.30}$	$-1.15^{+0.37}_{-0.49}$
1328066	$-0.73^{+0.75}_{-0.68}$	$1.45^{+0.84}_{-0.68}$	$1.32^{+0.41}_{-0.41}$	$-0.53^{+0.17}_{-0.21}$
1328105	$-0.57^{+0.57}_{-0.59}$	$0.82^{+0.58}_{-0.36}$	$1.43^{+0.32}_{-0.40}$	$-0.16^{+0.13}_{-0.20}$
1329312	$-1.01^{+1.05}_{-0.69}$	$2.80^{+0.78}_{-0.97}$	$0.76^{+0.39}_{-0.27}$	$-1.30^{+0.40}_{-0.49}$

Table B.2: Continued from above.

SNID	$\mathrm{Log}(Z_\star/Z_\odot)$	t_{age} (Gyr)	τ_V	n
1329615	$-0.67^{+0.86}_{-0.73}$	$2.08^{+1.03}_{-0.89}$	$1.25^{+0.45}_{-0.44}$	$-0.49^{+0.18}_{-0.21}$
1330031	$-0.95^{+0.45}_{-0.44}$	$1.62^{+0.73}_{-0.99}$	$0.90^{+0.61}_{-0.38}$	$-0.48^{+0.28}_{-0.42}$
1330426	$-0.41^{+1.00}_{-0.90}$	$0.95^{+0.38}_{-0.45}$	$0.24^{+0.26}_{-0.16}$	$-0.99^{+0.89}_{-0.81}$
1331123	$-0.68^{+0.87}_{-0.82}$	$2.61^{+1.04}_{-1.11}$	$1.10^{+0.47}_{-0.40}$	$-0.60^{+0.23}_{-0.34}$
1333246	$-0.57^{+0.64}_{-0.68}$	$0.39^{+0.46}_{-0.24}$	$2.46^{+0.50}_{-0.50}$	$-0.01^{+0.10}_{-0.17}$
1334084	$-0.63^{+0.49}_{-0.42}$	$1.04^{+0.56}_{-0.53}$	$1.25^{+0.52}_{-0.43}$	$-0.12^{+0.19}_{-0.29}$
1334087	$-0.64^{+1.08}_{-0.93}$	$4.25^{+0.75}_{-1.16}$	$0.50^{+0.24}_{-0.15}$	$-1.54^{+0.45}_{-0.43}$
1334302	$-0.56^{+0.54}_{-0.73}$	$0.50^{+0.42}_{-0.25}$	$2.28^{+0.35}_{-0.39}$	$-0.05^{+0.09}_{-0.18}$
1334423	$-0.54^{+0.56}_{-0.56}$	$0.29^{+0.23}_{-0.16}$	$1.19^{+0.35}_{-0.34}$	$-0.05^{+0.17}_{-0.25}$
1334448	$0.03^{+0.67}_{-0.71}$	$0.89^{+1.12}_{-0.64}$	$2.23^{+0.60}_{-0.71}$	$-0.36^{+0.09}_{-0.19}$
1334597	$-0.18^{+0.97}_{-0.96}$	$2.40^{+0.82}_{-1.05}$	$0.58^{+0.38}_{-0.23}$	$-1.27^{+0.52}_{-0.55}$
1334620	$-0.55^{+0.61}_{-0.52}$	$1.05^{+0.62}_{-0.45}$	$1.47^{+0.44}_{-0.39}$	$-0.23^{+0.18}_{-0.23}$
1334644	$0.96^{+0.64}_{-1.76}$	$2.26^{+2.55}_{-1.50}$	$0.81^{+0.73}_{-0.36}$	$-1.32^{+0.42}_{-0.53}$
1334645	$-0.65^{+0.91}_{-0.79}$	$2.38^{+0.88}_{-0.92}$	$0.91^{+0.41}_{-0.34}$	$-0.72^{+0.29}_{-0.42}$
1335717	$0.03^{+0.68}_{-0.61}$	$1.41^{+0.68}_{-0.56}$	$0.61^{+0.31}_{-0.25}$	$-0.66^{+0.32}_{-0.43}$
1336008	$-0.43^{+0.57}_{-0.47}$	$0.47^{+0.46}_{-0.22}$	$1.89^{+0.33}_{-0.49}$	$-0.01^{+0.09}_{-0.17}$
1336009	$-0.32^{+0.68}_{-0.58}$	$0.52^{+0.34}_{-0.25}$	$1.52^{+0.34}_{-0.33}$	$-0.05^{+0.14}_{-0.19}$
1336453	$-0.60^{+0.58}_{-0.46}$	$1.18^{+0.36}_{-0.41}$	$0.45^{+0.31}_{-0.19}$	$-0.76^{+0.43}_{-0.61}$
1336480	$-0.87^{+0.49}_{-0.52}$	$0.76^{+0.53}_{-0.44}$	$1.10^{+0.39}_{-0.39}$	$-0.32^{+0.25}_{-0.26}$
1336687	$-0.82^{+0.44}_{-0.44}$	$0.49^{+0.28}_{-0.31}$	$0.53^{+0.43}_{-0.28}$	$-0.68^{+0.46}_{-0.57}$
1337117	$-0.30^{+0.52}_{-0.76}$	$0.31^{+0.44}_{-0.27}$	$0.93^{+0.92}_{-0.55}$	$-0.29^{+0.31}_{-0.55}$
1337228	$-0.57^{+0.81}_{-0.66}$	$1.21^{+0.41}_{-0.52}$	$0.41^{+0.34}_{-0.20}$	$-0.88^{+0.41}_{-0.58}$
1337272	$-0.43^{+0.52}_{-0.76}$	$0.26^{+0.27}_{-0.19}$	$0.78^{+0.61}_{-0.41}$	$-0.20^{+0.33}_{-0.38}$
1337649	$-0.09^{+0.94}_{-0.99}$	$1.47^{+0.59}_{-0.70}$	$0.44^{+0.33}_{-0.20}$	$-1.06^{+0.57}_{-0.64}$
1337687	$-0.51^{+0.55}_{-0.52}$	$0.54^{+0.32}_{-0.26}$	$0.93^{+0.35}_{-0.30}$	$-0.19^{+0.22}_{-0.33}$
1337703	$-0.27^{+0.49}_{-0.39}$	$0.95^{+0.57}_{-0.40}$	$1.86^{+0.33}_{-0.38}$	$-0.38^{+0.08}_{-0.12}$
1337838	$0.62^{+1.68}_{-0.94}$	$0.06^{+0.15}_{-0.05}$	$0.65^{+0.44}_{-0.39}$	$-0.95^{+0.72}_{-0.73}$
1338128	$-0.43^{+0.63}_{-0.50}$	$0.87^{+0.44}_{-0.35}$	$0.67^{+0.32}_{-0.30}$	$-0.47^{+0.34}_{-0.46}$
1338170	$-0.16^{+0.88}_{-1.05}$	$2.29^{+0.75}_{-0.91}$	$0.62^{+0.32}_{-0.21}$	$-1.24^{+0.33}_{-0.43}$
1338278	$-0.33^{+0.50}_{-0.41}$	$0.47^{+0.32}_{-0.22}$	$1.13^{+0.38}_{-0.35}$	$-0.14^{+0.15}_{-0.18}$
1338430	$0.15^{+1.07}_{-0.85}$	$0.52^{+1.47}_{-0.48}$	$2.53^{+1.19}_{-1.10}$	$-0.10^{+0.14}_{-0.22}$
1338471	$-0.90^{+0.79}_{-0.65}$	$1.91^{+0.78}_{-0.79}$	$0.70^{+0.41}_{-0.32}$	$-0.77^{+0.29}_{-0.43}$
1338675	$-0.02^{+0.66}_{-0.76}$	$0.75^{+0.42}_{-0.33}$	$0.63^{+0.39}_{-0.30}$	$-0.40^{+0.36}_{-0.62}$
1339002	$-0.17^{+0.76}_{-0.70}$	$1.04^{+0.84}_{-0.50}$	$2.20^{+0.40}_{-0.48}$	$-0.17^{+0.10}_{-0.14}$
1339149	$-0.23^{+0.50}_{-0.35}$	$0.14^{+0.14}_{-0.07}$	$1.33^{+0.38}_{-0.39}$	$0.00^{+0.15}_{-0.22}$
1339392	$0.10^{+0.90}_{-0.85}$	$3.42^{+1.14}_{-1.24}$	$0.74^{+0.36}_{-0.25}$	$-1.03^{+0.45}_{-0.58}$

Table B.2: Continued from above.

SNID	$\mathrm{Log}(Z_\star/Z_\odot)$	t_{age} (Gyr)	τ_V	n
1339450	$-0.26^{+0.51}_{-0.42}$	$0.39^{+0.49}_{-0.20}$	$2.26^{+0.45}_{-0.54}$	$0.03^{+0.08}_{-0.10}$
1340454	$-0.46^{+0.70}_{-0.61}$	$1.16^{+0.65}_{-0.55}$	$0.82^{+0.40}_{-0.35}$	$-0.40^{+0.23}_{-0.33}$
1341370	$-0.61^{+0.76}_{-0.80}$	$0.86^{+0.49}_{-0.48}$	$0.48^{+0.44}_{-0.28}$	$-0.66^{+0.60}_{-0.73}$
1341894	$-0.48^{+0.63}_{-0.63}$	$0.66^{+0.50}_{-0.31}$	$1.09^{+0.39}_{-0.43}$	$-0.26^{+0.25}_{-0.37}$
1342255	$-0.25^{+0.96}_{-0.90}$	$1.92^{+0.67}_{-0.77}$	$0.52^{+0.34}_{-0.22}$	$-0.98^{+0.52}_{-0.70}$
1343208	$-0.56^{+0.52}_{-0.63}$	$1.45^{+0.73}_{-0.57}$	$1.25^{+0.35}_{-0.39}$	$-0.46^{+0.15}_{-0.19}$
1343337	$-0.31^{+0.65}_{-0.52}$	$0.37^{+0.29}_{-0.19}$	$1.49^{+0.42}_{-0.37}$	$-0.05^{+0.16}_{-0.22}$
1343401	$-0.33^{+1.00}_{-1.02}$	$3.24^{+1.49}_{-1.37}$	$0.91^{+0.60}_{-0.41}$	$-0.71^{+0.30}_{-0.51}$
1343533	$-0.22^{+0.92}_{-1.00}$	$2.02^{+0.97}_{-0.96}$	$1.09^{+0.47}_{-0.38}$	$-0.70^{+0.23}_{-0.34}$
1343759	$-0.89^{+0.83}_{-0.76}$	$0.52^{+0.51}_{-0.38}$	$0.84^{+0.60}_{-0.42}$	$-0.49^{+0.29}_{-0.35}$
1344692	$-0.82^{+0.75}_{-0.69}$	$2.20^{+0.91}_{-0.83}$	$1.24^{+0.39}_{-0.38}$	$-0.80^{+0.20}_{-0.26}$
1345553	$-0.58^{+0.76}_{-0.67}$	$1.27^{+0.99}_{-0.64}$	$1.07^{+0.49}_{-0.51}$	$-0.41^{+0.26}_{-0.41}$
1345594	$-0.79^{+0.77}_{-0.69}$	$2.48^{+1.30}_{-1.08}$	$1.69^{+0.51}_{-0.52}$	$-0.34^{+0.12}_{-0.13}$
1346137	$-0.29^{+0.51}_{-0.38}$	$0.27^{+0.19}_{-0.13}$	$1.71^{+0.36}_{-0.32}$	$0.06^{+0.10}_{-0.14}$
1346387	$-0.88^{+0.59}_{-0.59}$	$0.25^{+0.69}_{-0.22}$	$2.72^{+0.92}_{-0.87}$	$0.03^{+0.17}_{-0.22}$
1346956	$-0.19^{+1.33}_{-1.27}$	$0.36^{+0.22}_{-0.23}$	$0.18^{+0.30}_{-0.13}$	$-0.77^{+0.81}_{-0.93}$
1346966	$-0.96^{+0.89}_{-0.67}$	$1.65^{+0.55}_{-0.64}$	$0.49^{+0.32}_{-0.22}$	$-1.07^{+0.45}_{-0.55}$

Table B.3: *Best-fit* results for the DES host galaxies fits with GALEX *NUV*/*FUV*, 2MASS *JHKs* and DECam *griz* photometry.

SNID	$\mathrm{Log}(M_\star/M_\odot)$	$\mathrm{Log}(Z_\star/Z_\odot)$	t_{age} (Gyr)	τ_V	n
1255502	$11.19^{+0.25}_{-0.09}$	$1.57^{+0.08}_{-0.11}$	$0.66^{+0.05}_{-0.07}$	$3.12^{+0.65}_{-0.27}$	$-0.05^{+0.28}_{-0.15}$
1257366	$11.17^{+0.01}_{-0.01}$	$-1.02^{+0.01}_{-0.02}$	$8.49^{+0.18}_{-0.15}$	$0.00^{+0.01}_{-0.00}$	$-0.93^{+0.85}_{-0.77}$
1257695	$10.11^{+0.15}_{-0.30}$	$-0.96^{+1.21}_{-1.03}$	$4.24^{+1.75}_{-2.48}$	$0.05^{+0.13}_{-0.05}$	$-1.09^{+0.88}_{-1.03}$
1259412	$10.36^{+0.15}_{-0.11}$	$-1.89^{+0.13}_{-0.09}$	$0.24^{+0.40}_{-0.12}$	$1.56^{+0.10}_{-0.15}$	$-0.60^{+0.10}_{-0.01}$
1282757	$10.17^{+0.15}_{-0.15}$	$-1.85^{+0.10}_{-0.11}$	$0.14^{+0.36}_{-0.08}$	$1.64^{+0.12}_{-0.24}$	$-0.44^{+0.03}_{-0.03}$
1284587	$11.19^{+0.01}_{-0.03}$	$-1.78^{+0.03}_{-0.06}$	$13.72^{+0.06}_{-0.41}$	$0.51^{+0.01}_{-0.05}$	$0.23^{+0.04}_{-0.08}$
1286398	$10.64^{+0.05}_{-0.04}$	$-0.29^{+0.04}_{-0.05}$	$5.70^{+0.46}_{-0.43}$	$0.27^{+0.02}_{-0.02}$	$-0.67^{+0.33}_{-0.23}$
1291090	$10.19^{+0.07}_{-0.10}$	$-1.84^{+0.25}_{-0.12}$	$1.56^{+0.27}_{-0.26}$	$1.45^{+0.13}_{-0.17}$	$0.23^{+0.08}_{-0.08}$
1292145	$10.62^{+0.19}_{-0.21}$	$1.92^{+0.15}_{-0.19}$	$1.78^{+0.22}_{-0.29}$	$2.05^{+0.63}_{-0.65}$	$0.22^{+0.13}_{-0.28}$
1293758	$10.61^{+0.13}_{-0.39}$	$-1.77^{+0.05}_{-0.16}$	$0.29^{+1.05}_{-0.27}$	$1.67^{+0.43}_{-0.46}$	$-0.74^{+0.14}_{-0.18}$
1296657	$10.00^{+0.01}_{-0.01}$	$0.87^{+0.05}_{-0.04}$	$2.34^{+0.03}_{-0.03}$	$0.06^{+0.01}_{-0.01}$	$-1.37^{+0.15}_{-0.19}$
1297465	$10.54^{+0.06}_{-0.09}$	$0.80^{+0.27}_{-0.29}$	$1.61^{+0.25}_{-0.30}$	$1.77^{+0.16}_{-0.21}$	$0.23^{+0.08}_{-0.08}$
1299785	$10.29^{+0.14}_{-0.16}$	$-1.27^{+0.41}_{-0.42}$	$2.24^{+1.18}_{-1.15}$	$0.88^{+0.25}_{-0.22}$	$-0.26^{+0.30}_{-0.20}$
1302058	$9.91^{+0.06}_{-0.05}$	$-1.74^{+0.41}_{-0.21}$	$0.69^{+1.06}_{-0.36}$	$1.67^{+0.21}_{-0.52}$	$-0.46^{+0.03}_{-0.04}$

Table B.3: Continued from above.

SNID	$\mathrm{Log}(M_\star/M_\odot)$	$\mathrm{Log}(Z_\star/Z_\odot)$	t_{age} (Gyr)	τ_V	n
1302187	$10.97^{+0.06}_{-0.08}$	$-1.35^{+0.36}_{-0.50}$	$0.71^{+0.55}_{-0.27}$	$2.05^{+0.35}_{-0.27}$	$-0.35^{+0.01}_{-0.02}$
1303496	$10.27^{+0.09}_{-0.11}$	$-1.82^{+0.07}_{-0.14}$	$0.19^{+0.52}_{-0.11}$	$2.34^{+0.19}_{-0.42}$	$-0.49^{+0.05}_{-0.09}$
1304442	$9.74^{+0.08}_{-0.06}$	$-1.09^{+0.12}_{-0.23}$	$0.93^{+0.11}_{-0.11}$	$1.72^{+0.07}_{-0.06}$	$0.39^{+0.01}_{-0.07}$
1306141	$9.97^{+0.15}_{-0.16}$	$0.84^{+0.24}_{-0.51}$	$0.37^{+0.57}_{-0.12}$	$1.50^{+0.32}_{-0.36}$	$-0.13^{+0.16}_{-0.15}$
1306785	$11.61^{+0.10}_{-0.11}$	$-0.66^{+0.37}_{-0.30}$	$9.30^{+2.34}_{-1.95}$	$0.87^{+0.18}_{-0.16}$	$-0.22^{+0.24}_{-0.27}$
1308884	$10.56^{+0.00}_{-0.00}$	$-1.50^{+0.00}_{-0.00}$	$2.47^{+0.01}_{-0.01}$	$0.83^{+0.00}_{-0.00}$	$-0.37^{+0.00}_{-0.00}$
1309288	$11.50^{+0.01}_{-0.14}$	$-1.74^{+0.53}_{-0.01}$	$13.74^{+0.05}_{-5.09}$	$0.39^{+0.06}_{-0.02}$	$-0.14^{+0.12}_{-0.07}$
1315259	$11.91^{+0.00}_{-0.00}$	$-1.75^{+0.00}_{-0.00}$	$13.79^{+0.00}_{-0.17}$	$0.45^{+0.04}_{-0.00}$	$-0.37^{+0.07}_{-0.01}$
1316385	$10.19^{+0.07}_{-0.05}$	$1.40^{+0.12}_{-0.09}$	$0.61^{+0.13}_{-0.08}$	$1.74^{+0.04}_{-0.07}$	$-0.63^{+0.17}_{-0.03}$
1317666	$10.02^{+0.03}_{-0.04}$	$-1.54^{+0.40}_{-0.41}$	$1.00^{+1.35}_{-0.48}$	$1.46^{+0.34}_{-0.71}$	$-0.56^{+0.05}_{-0.21}$
1319821	$10.98^{+0.10}_{-0.17}$	$-1.33^{+0.51}_{-0.24}$	$1.40^{+0.12}_{-0.30}$	$2.33^{+0.15}_{-0.08}$	$0.39^{+0.01}_{-0.01}$
1328105	$11.95^{+0.03}_{-0.04}$	$1.66^{+0.05}_{-0.06}$	$1.92^{+0.08}_{-0.07}$	$1.66^{+0.18}_{-0.19}$	$-0.01^{+0.07}_{-0.09}$
1330031	$9.03^{+0.08}_{-0.05}$	$-1.90^{+0.12}_{-0.08}$	$0.34^{+0.35}_{-0.14}$	$1.51^{+0.15}_{-0.19}$	$-0.65^{+0.07}_{-0.06}$
1334620	$10.01^{+0.11}_{-0.11}$	$-1.89^{+0.13}_{-0.08}$	$0.18^{+0.34}_{-0.09}$	$1.79^{+0.16}_{-0.29}$	$-0.64^{+0.06}_{-0.09}$
1336480	$9.98^{+0.15}_{-0.11}$	$-1.87^{+0.19}_{-0.10}$	$0.26^{+0.74}_{-0.15}$	$1.64^{+0.17}_{-0.38}$	$-0.46^{+0.09}_{-0.04}$
1338128	$9.69^{+0.10}_{-0.10}$	$1.35^{+0.21}_{-0.24}$	$0.93^{+0.34}_{-0.27}$	$1.39^{+0.33}_{-0.33}$	$0.09^{+0.15}_{-0.14}$
1339002	$10.26^{+0.09}_{-0.08}$	$-1.80^{+0.15}_{-0.14}$	$0.16^{+0.19}_{-0.06}$	$1.86^{+0.08}_{-0.20}$	$-0.83^{+0.02}_{-0.03}$
1339450	$11.60^{+0.02}_{-0.17}$	$0.17^{+0.06}_{-0.22}$	$6.03^{+0.10}_{-3.68}$	$0.03^{+1.17}_{-0.02}$	$-0.20^{+0.34}_{-0.94}$
1343337	$10.79^{+0.06}_{-0.09}$	$1.71^{+0.11}_{-0.09}$	$1.53^{+0.16}_{-0.15}$	$1.84^{+0.29}_{-0.44}$	$0.27^{+0.09}_{-0.17}$

Appendix C

Kron Aperture Photometry

Kron aperture photometry is a technique developed by Kron (1980)[38] to automatically determine elliptical apertures for galaxy photometry. In the Appendix, we will detail the formalism behind this technique.

C.1 Position and Shape of an Observed Object

An observed object's light distribution S is composed of N pixels, each with a value p_i and arranged in a grid with coordinates (x_i, y_i). From S, some important quantities can be defined, namely the first and second order moments.

The first moments, defined by Eqs. C.1 and C.2, are normally used to define the "center"[51] of the observed object. This works particularly well if the light distribution is not strongly skewed and does not have large wings[51].

$$\bar{x} = \frac{\sum_{i \in S} p_i x_i}{\sum_{i \in S} p_i} \tag{C.1}$$

$$\bar{y} = \frac{\sum_{i \in S} p_i y_i}{\sum_{i \in S} p_i} \tag{C.2}$$

The second moments, defined by Eqs. C.3, C.4 and C.5, are used to measure the spatial spread of the light profile.

$$\overline{x^2} = \frac{\sum_{i \in S} p_i x_i^2}{\sum_{i \in S} p_i} - \bar{x}^2 \tag{C.3}$$

$$\overline{y^2} = \frac{\sum_{i \in S} p_i y_i^2}{\sum_{i \in S} p_i} - \bar{y}^2 \tag{C.4}$$

$$\overline{xy} = \frac{\sum_{i \in S} p_i x_i y_i}{\sum_{i \in S} p_i} - \bar{x}\bar{y} \tag{C.5}$$

It should be noted that, in the previous definitions, the values of p_i are often taken from a detection image[50]. This assures consistency in the moment values when more than one filter bands are considered.

The first and second moments can be essentially used to describe the detected object as an elliptical shape. For this reason, it is useful to establish a relation between these quantities and the usual ellipse parameters, namely the semi-major and semi-minor axes a and b, defined as the ellipse's longest and shortest diameter, respectively, and the rotation angle θ, defined as the angle from the positive horizontal axis to the ellipse's major axis. The geometrical representation of the ellipse parameters is illustrated in Fig. C.1.

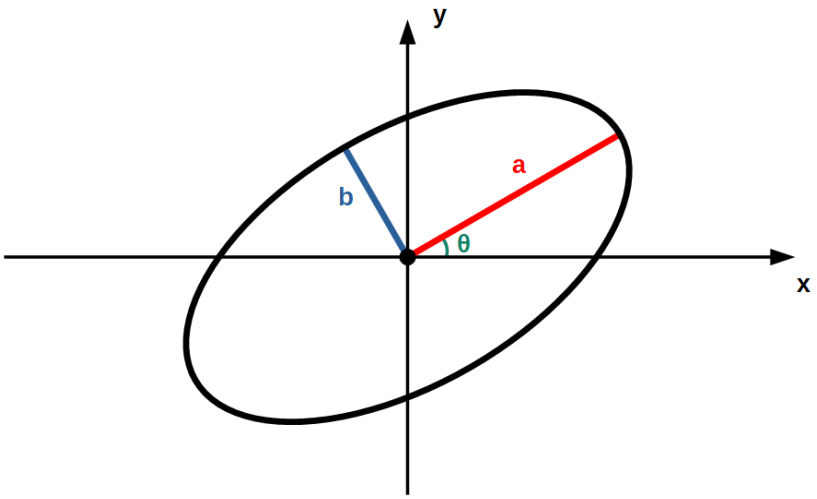

Figure C.1: Schematic representation of the ellipse parameters. The semi-major axis a is shown in red, the semi-minor axis b is shown in blue and the rotation angles θ is shown in green.

The ellipse parameters can be computed from the second order moments using[51]:

$$a^2 = \frac{\overline{x^2} + \overline{y^2}}{2} + \sqrt{\left(\frac{\overline{x^2} - \overline{y^2}}{2}\right)^2 + \overline{xy}^2} \tag{C.6}$$

$$b^2 = \frac{\overline{x^2} + \overline{y^2}}{2} - \sqrt{\left(\frac{\overline{x^2} - \overline{y^2}}{2}\right)^2 + \overline{xy}^2} \tag{C.7}$$

$$\theta = \frac{1}{2}\arctan\left(2\frac{\overline{xy}}{\overline{x^2} - \overline{y^2}}\right) \tag{C.8}$$

In this last equation, we choose the solution in the range $\left[-\frac{\pi}{2}, \frac{\pi}{2}\right[$ with the same sign as $\overline{xy}$[51].

In order to actually compute aperture positions, an alternative parameterization of the ellipse is often used, which can be written in terms of the parameters c_{xx}, c_{yy} and c_{xy}[51]:

$$c_{xx}(x - \bar{x})^2 + c_{yy}(y - \bar{y})^2 + c_{xy}(x - \bar{x})(y - \bar{y}) = R^2, \tag{C.9}$$

where R is a parameter that scales the ellipse, either in units of a or b, usually known as the "reduced

pseudo-radius". These new ellipse parameters can also be expressed in terms of the second order moments of the object light distribution[51]:

$$c_{xx} = \frac{\overline{y^2}}{\overline{x^2}\,\overline{y^2} - \overline{xy}^2} \tag{C.10}$$

$$c_{yy} = \frac{\overline{x^2}}{\overline{x^2}\,\overline{y^2} - \overline{xy}^2} \tag{C.11}$$

$$c_{xy} = -2\frac{\overline{xy}}{\overline{x^2}\,\overline{y^2} - \overline{xy}^2} \tag{C.12}$$

C.2 Kron's First Moment Algorithm

Kron apertures are derived from a "first moment" algorithm[50], the reduced radius of which can be obtained by following the steps detail below:

1. An elliptical aperture E is defined by the second order moments of the observed object's light distribution, using Eqs. C.6, C.7 and C.8;
2. The semi-major and semi-minor axes are multiplied by 6;
3. Inside E, an analog of Kron's "first moment" is computed:

$$r_{Kron} = \frac{\sum_{i \in E} p_i r_i}{\sum_{i \in S} p_i} \tag{C.13}$$

4. The Kron radius is defined as a multiple of this first moment: kr_{Kron}. Usually, $k = 2$ is chosen.

The quantity r_i in Eq. C.13 refers to the "reduced pseudo-radius" at a given pixel i, which is given by:

$$r_i = \sqrt{c_{xx}(x_i - \bar{x})^2 + c_{yy}(y_i - \bar{y})^2 + c_{xy}(x_i - \bar{x})(y_i - \bar{y})} \tag{C.14}$$

Evidence shows that, using an elliptical aperture with a "reduced pseudo-radius" kr_{Kron} with $k = 2$, one is able to capture $> 90\%$ of the total object's light flux, almost independently of the magnitude[37][38]. This is the most important property of Kron's method, as it allows for a systematic and automatic definition of apertures across a wide range of luminosity in the observed objects.

Appendix D

Gaussian Processes Regression

D.1 Gaussian Processes

Gaussian processes are a set of stochastic processes that assume that, for a given data set, the output $\mathbf{y}$ associated with a given input $\mathbf{X}$ follows a multivariate normal distribution, given by Eq. D.1[43]. Here, $\mathbf{y}$ is a n-dimensional output vector, comprised of n output values y_i, while $\mathbf{X}$ is a $n \times d$ input matrix, comprised of n d-dimensional input vectors $\mathbf{x}$. The goal of Gaussian processes regression is to determine the previously mentioned distribution, so predictions about the data can be made from a new set of input points.

$$\mathbf{y} \sim \mathcal{N}(\mu(\mathbf{X}), \Sigma(\mathbf{X})) \tag{D.1}$$

In the previous equation, $\mu(\mathbf{X})$ and $\Sigma(\mathbf{X})$ are known as the mean and covariance functions, respectively.

The mean function defines a mean for the distribution, which can be different for each point. More commonly, however, when performing a Gaussian processes regression, $\mu(\mathbf{X})$ is assumed to be constant, with $\mu(\mathbf{X}) = \boldsymbol{\mu}$, where $\boldsymbol{\mu} = \mu \mathbb{1}_n$.

The covariance function essentially controls the covariance between any two input vectors and is often written in the form:

$$\Sigma = \sigma^2 R, \tag{D.2}$$

where R is a correlation function, which maps any pair of input vectors to a real number in the range $[0, 1]$. To obtain the correct covariance function, R must be then scaled by a variance parameter σ^2. The correlation function R most commonly takes a Gaussian form. In such cases, for any two d-dimensional input vectors $\mathbf{u}$ and $\mathbf{v}$, $R(\mathbf{u}, \mathbf{v})$ is thus given by[43]:

$$R(\mathbf{u}, \mathbf{v}) = e^{-\sum_{i=1}^{d} \theta_i (u_i - v_i)^2}, \tag{D.3}$$

where $\boldsymbol{\theta}$ is a d-dimensional vector containing the correlation parameters for each dimension. From this expression we can then define the correlation and covariance matrices, which are represented as $R(\mathbf{X})$ and $\Sigma(\mathbf{X})$, respectively.

D.2 Data Predictions

The main purpose of Gaussian processes regression is to determine the values of μ and σ^2. This is done though the maximization of the likelihood function for the given data set, which is defined as[43]:

$$\ln(\mathcal{L}) = -\frac{1}{2}\left[\ln\left(\Sigma(\mathbf{X})\right) + (\mathbf{y}-\boldsymbol{\mu})^T\Sigma^{-1}(\mathbf{X})(\mathbf{y}-\boldsymbol{\mu})\right] \tag{D.4}$$

To obtain an estimate for μ, we differentiate Eq. D.4 with respect to μ and set the result equal to zero. We thus obtain the maximum likelihood estimate $\hat{\mu}$, given by[43]:

$$\hat{\mu} = \frac{\mathbb{1}_n^T\Sigma^{-1}(\mathbf{X})\mathbf{y}}{\mathbb{1}_n^T\Sigma^{-1}(\mathbf{X})\mathbb{1}_n} \tag{D.5}$$

Doing the same for σ^2, we obtain the maximum likelihood estimate $\hat{\sigma}^2$, which is given by[43]:

$$\hat{\sigma}^2 = \frac{1}{n}(\mathbf{y}-\boldsymbol{\mu})^T R^{-1}(\mathbf{X})(\mathbf{y}-\boldsymbol{\mu}) \tag{D.6}$$

With these estimates we can then begin to make predictions about the outputs for a series of new input values. Assuming we have a set of inputs $\mathbf{X}_1$ and a set of outputs $\mathbf{y}_1$ that have been used to calculate $\hat{\mu}$ and $\hat{\sigma}^2$, an estimation of the output y_2 for a new input vector $\mathbf{x}_2$ can be estimated using[43]:

$$\hat{y}_2 = \hat{\mu} + R(\mathbf{x}_2, \mathbf{X}_1)R(\mathbf{X}_1)^{-1}(\mathbf{y}_1 - \boldsymbol{\mu}), \tag{D.7}$$

where $R(\mathbf{x}_2, \mathbf{X}_1)$ is a line vector whose elements are the covariance of the lines of $\mathbf{X}_1$ with $\mathbf{x}_2$.

Additionally, the accuracy of the model can be evaluated using an estimate of the standard error associated with $\hat{y}_2$, which can be obtained using[43]:

$$\hat{\sigma}^2(y_2) = R(\mathbf{x}_2) - R(\mathbf{x}_2, \mathbf{X}_1)R(\mathbf{X}_1)^{-1}R(\mathbf{X}_1, \mathbf{x}_2), \tag{D.8}$$

where $R(\mathbf{X}_1, \mathbf{x}_2)$ is a column vector whose elements are the covariance of the rows of $\mathbf{X}_1$ with $\mathbf{x}_2$.